UNIVERSIDADE FEDERAL DE SÃO CARLOS
CENTRO DE CIÊNCIAS EXATAS E DE TECNOLOGIA
DEPARTAMENTO DE QUÍMICA
PROGRAMA DE PÓS-GRADUAÇÃO EM QUÍMICA

EVALUATION OF THE COMPOSITION OF ELECTRONIC WASTE HARD DISK USING SPECTROANALYTICAL TECHNIQUES: PROPOSITION OF FAST AND SIMPLE METHODS

Jeyne Pricylla de Castro*

Tese apresentada como parte dos requisitos para obtenção do título de DOUTORA EM CIÊNCIAS, área de concentração: QUÍMICA ANALÍTICA.

Orientador: Prof. Dr. Edenir Rodrigues Pereira Filho

*** Bolsista FAPESP: 2016/17221-8 e 2018/17753-5**

São Carlos - SP

2020

UNIVERSIDADE FEDERAL DE SÃO CARLOS

Centro de Ciências Exatas e de Tecnologia
Programa de Pós-Graduação em Química

Folha de Aprovação

Defesa de Tese de Doutorado da candidata Jeyne Pricylla de Castro, realizada em 17/12/2020.

Comissão Julgadora:

Prof. Dr. Edenir Rodrigues Pereira Filho (UFSCar)

Profa. Dra. Maria Fernanda Pimentel Avelar (UFPE)

Prof. Dr. Frederico Luis Felipe Soares (UFPR)

Profa. Dra. Gisele Simone Lopes (UFC)

Profa. Dra. Carolina Santos Silva (UFPE)

O presente trabalho foi realizado com apoio da Coordenação de Aperfeiçoamento de Pessoal de Nível Superior - Brasil (CAPES) - Código de Financiamento 001.
O Relatório de Defesa assinado pelos membros da Comissão Julgadora encontra-se arquivado junto ao Programa de Pós-Graduação em Química.

DEDICATÓRIA

“Não te ordenei que sejas forte e corajoso? Não tenhas medo, não te acovardes, pois o Senhor, teu Deus, estará contigo por onde quer que vás.”

Js 1, 9.

Dedico este trabalho a Deus e a minha família.

AGRADECIMENTOS

A Deus, por ser sustento e força a cada amanhecer. Por cuidar e me guardar debaixo de sua proteção. “Na verdade, tudo é dEle, por Ele, e para Ele. A Ele, a glória para sempre. Amém.” Rm 11, 36.

A toda a minha família, por todo suporte e amor. Meus queridos pais, Vânia e Vandeil, obrigada por tudo e por sempre serem meu porto seguro. Eu amo vocês.

Ao meu noivo Leonardo pelo companheirismo, apoio e incentivo a buscar os meus sonhos. Por sempre confiar e acreditar que eu sou capaz. Obrigada por todo cuidado e amor.

Ao professor Edenir por ter aceitado me orientar lá em 2014 ainda no mestrado. Foram seis anos de muito aprendizado e crescimento profissional/pessoal. Obrigada por toda amizade e orientação durante esse período. Você é uma pessoa extraordinária que pensa em seus alunos como se fossem seus filhos, sou muito grata a você.

Ao professor Rasmus Bro, pela oportunidade e orientação durante a realização do estágio de doutorado no exterior. Aos amigos que fiz durante esse período, Isabelle, Rafaela, Stefano, Sahar, Isabel e ao pessoal da Igreja St. Augustine, obrigada por tornarem essa caminhada mais leve e alegre.

Aos amigos e professores do Grupo de Análise Instrumental Aplicada. É sempre uma alegria conviver com todos vocês. Obrigada por cada café, almoço, conversas, trabalhos em conjunto e tantos aprendizados. Levarei vocês sempre comigo.

A Taíse e a Jéssica, companheiras de “república”, obrigada pela convivência e amizade durante todo esse tempo. Vocês são muito especiais.

Aos membros da banca por aceitarem o convite e por contribuírem com essa tese. Obrigada a cada um de vocês.

Ao programa de pós-graduação em Química, secretárias e coordenação por todo suporte.

A Universidade Federal de São Carlos e ao Departamento de Química pela estrutura fornecida para a realização do trabalho.

A Fundação de Amparo a Pesquisa do Estado de São Paulo (FAPESP) pelas bolsas concedidas (doutorado e BEPE).

As editoras Elsevier e Royal Society of Chemistry e ao jornal Detritus pela autorização do uso dos artigos publicados e apresentados no corpo dessa tese.

O presente trabalho foi realizado com apoio da Coordenação de Aperfeiçoamento de Pessoal de Nível Superior – CAPES, código de financiamento 001.

O meu muito obrigado a todos!

This PhD thesis is based on the following publications which are presented in the original format:

“Spectroanalytical method for evaluating the technological elements composition of magnets from computer hard disks”
Jeyne Pricylla Castro, Edenir Rodrigues Pereira-Filho, *Talanta* 189 (2018) 205-210.

“Chemical exploratory analysis of printed circuit board (PCB) using inductively coupled plasma optical emission spectrometry (ICP OES): data treatment and elements correlation”
Jeyne Pricylla Castro, Edenir Rodrigues Pereira-Filho, *Detritus* 13 (2020) 131-139.

“Calibration strategies for the direct determination of rare earth elements in hard disk magnets using laser-induced breakdown spectroscopy”
Jeyne Pricylla Castro, Diego Victor Babos, Edenir Rodrigues Pereira-Filho, *Talanta* 208 (2020) 120443.

“Neodymium determination in hard drive disks magnets using different calibration approaches for wavelength dispersive X-ray fluorescence”
Jeyne Pricylla Castro, Marco Aurelio Sperança, Diego Victor Babos, Daniel Fernandes Andrade, Edenir Rodrigues Pereira-Filho, *Spectrochimica Acta Part B* 164 (2020) 105763.

“Laser-induced breakdown spectroscopy (LIBS) spectra interpretation and characterization using parallel factor analysis (PARAFAC): a new procedure for data and spectral interference processing fostering the waste electrical and electronic equipment (WEEE) recycling process”
Jeyne Pricylla Castro, Edenir Rodrigues Pereira-Filho, Rasmus Bro, *Journal of Analytical Atomic Spectrometry* 35 (2020) 1115-1124.

LIST OF ACRONYNS

ABINEE	Associação Brasileira de industrias de EEE
ALS	Alternating least square
ANN	Artificial neural networks
BBC	British broadcasting corporation
BFR	Brominated flame retardants
CETESB	Companhia Ambiental do Estado de São Paulo
CFCs	Chlorofluorocarbons
CORCONDIA	Core consistency diagnostic
CRM	Certified reference material
CV	Cross-validation
EC	External calibration
EEE	Electrical and electronic equipment
E-WASTE	Electronic waste
FECOMERCIO-SP	Federação do comércio do Estado de São Paulo
FPC	Flow proportional counter
HCFCs	Hydrochlorofluorocarbons
HD	Hard disk
HR-CS-FAAS	High-resolution continuum source flame atomic absorption spectrometry
ICP	Inductively coupled plasma
ICP OES	Inductively coupled plasma optical emission spectroscopy
IS	Internal standardization
LCD	Liquid crystal displays
LIBS	Laser-induced breakdown spectroscopy
MEC	Multi-energy calibration
MIP OES	Microwave-induced plasma optical Emission spectrometry
MLR	Multiple linear regression
MMC	Matrix-matching calibration
Mt	Million metric tons
NIPALS	Nonlinear iterative partial least squares

OP GSA	One-point gravimetric standard addition
PARAFAC	Parallel factor analysis
PCA	Principal component analysis
PCB	Printed circuit board
PCR	Principal component regression
PGMs	Platinum group metals
PLS	Partial least square
PLS DA	Partial least square discriminant analysis
PNRS	National solid waste policy
REEs	Rare earth elements
RSD	Relative standard deviation
SAG	Sectorial agreement
SA	Standard addition
SC	Scintillation counter
SMA-SP	Secretaria de Estado do Meio Ambiente
SRC	Slope ratio calibration
TP CT	Two-point calibration transfer
WD XRF	Wavelength dispersive x-ray fluorescence
WEEE	Waste electrical and electronic equipment
XRF	X-ray fluorescence

LIST OF FIGURES

RESUMO

AVALIAÇÃO DA COMPOSIÇÃO DE DISCOS RÍGIDOS DE RESÍDUOS ELETRÔNICOS UTILIZANDO TÉCNICAS ESPECTROANALÍTICAS: PROPOSIÇÃO DE MÉTODOS RÁPIDOS E SIMPLES. Os resíduos eletrônicos são um problema mundial de grande magnitude com 53,6 Mt de resíduos gerados em 2019. Infelizmente a taxa de reciclagem ainda é muito baixa. Estima-se que apenas 2% do resíduo eletrônico é reciclado no Brasil, sendo uma situação longe da ideal. Há muitos fatores que podem influenciar a reciclagem sendo a complexidade desses materiais um aspecto crítico. Assim, a química analítica pode auxiliar em todo esse processo, otimizando e desenvolvendo novos métodos. Essa tese teve como objetivo o desenvolvimento de procedimentos de caracterização de amostras de imãs de alto desempenho e placas de circuito impresso provenientes do disco rígido de computadores. Três técnicas analíticas foram utilizadas: *Inductively coupled plasma optical emission spectroscopy* (ICP OES), *Laser-induced breakdown spectroscopy* (LIBS) e *Wavelength dispersive x-ray fluorescence* (WD XRF). Métodos de referência mais brandos foram desenvolvidos utilizando ICP OES, onde os resultados foram utilizados para a proposição de métodos mais rápidos, simples e “verdes” utilizando as técnicas de análise direta de sólidos (LIBS e WD XRF). Nesse contexto, diferentes abordagens de calibração foram estudadas, e nessa tese foi proposta uma nova abordagem intitulada como *two point calibration transfer* (TP CT). Além disso, *paralell factor analysis* (PARAFAC) foi utilizado pela primeira vez na caracterização dos espectros LIBS provenientes da análise das placas de circuito impresso, apresentando ser uma abordagem promissora para a técnica LIBS.

ABSTRACT

EVALUATION OF THE COMPOSITION OF ELECTRONIC WASTE HARD DISK USING SPECTROANALYTICAL TECHNIQUES: PROPOSITION OF FAST AND SIMPLE METHODS. The electronic waste is a worldwide problem of great magnitude with 53.6 Mt of waste generated in 2019. Unfortunately, the recycling rate is still very low. It is estimated that only 2% of the electronic waste is recycled in Brazil, being a situation far from ideal. There are many factors that can influence recycling, being the complexity of these materials a critical aspect. Therefore, the analytical chemistry can assist in all this process, optimizing and developing new methods. The purpose of this thesis was the development of characterization procedures of high-performance magnets and printed circuit board samples from hard disk of computer. Three analytical techniques were used: Inductively coupled plasma optical emission spectroscopy (ICP OES), Laser-induced breakdown spectroscopy (LIBS) and Wavelength dispersive x-ray fluorescence (WD XRF). So, softer reference methods were developed using ICP OES, where the results were used to the proposition of methods more quick, simple and “green” using the techniques of direct analysis of solids (LIBS and WD XRF). In this context, different calibration approaches were studied and, in this thesis was proposed a new strategy named by two-point calibration transfer (TP CT). In addition, parallel factor analysis (PARAFAC) was used for the first time in the characterization of spectra LIBS from the analysis of printed circuit board, being a promising approach for the LIBS technique.

SUMMARY

Chapter 1: Introduction

1. Introduction

1.1. Electronic waste context

Nowadays, electrical and electronic equipment (EEE) is part of everyone's daily life and, its use is directly linked to global economic development with growing urbanization, mobility, industrialization and high levels of disposable incomes [1–3]. Consequently, growing amounts of EEE have been used, where old technologies are replaced by new one, reducing the lifespan of the equipment. Therefore, the disposal of these EEE's is a concern [1–3]. When the EEE is discarded by its owner without the intent of reuse, becomes electronic waste (e-waste). In 2019, 53.6 million metric tons (Mt) of e-waste was generated, which corresponds to 7.3 kg per capita, distributed among Asia (24.9 Mt), Americas (13.1 Mt), Europe (12 Mt), Africa (2.9 Mt) and Oceania (0.7 Mt) [1]. According to Lundgren, this residue class is the fastest growing worldwide [4].

The great problem is the rate of formal documented collection and recycling with a value of 9.3 Mt in 2019, which is 17.4% in relation to e-waste generated [1]. Since 2014, this rate has grown by almost 0.4 Mt, on the other hand, the generation of e-waste has grown by 9.2 Mt, being totally unbalanced [1]. The recycling rate depends on several factors and, one of them is the legislation of each country, where in 2019, 71% of population was covered by legislation, policy or regulation [1]. In addition, the complexity, variety and different sizes of EEE, health and environmental factors and, lack of knowledge on the subject can make this difficult [5].

Brazil is considered the largest e-waste producer in South America and, in 2010 was instituted the National Solid Waste Policy (PNRS) [6], which is mandatory the implementation of e-waste take-back systems in countrywide made by Sectorial Agreement (SAG) [6,7]. The SAG are contracts signed among representatives of EEE producers and the Government focusing in a shared responsibility of EEE life cycles [7]. In São Paulo State, for example, there is a SAG among SMA-SP (Secretaria de Estado do Meio Ambiente), CETESB (Companhia Ambiental do Estado de São Paulo) and Green Eletron that is an entity of take-back systems represented by ABINEE (Associação Brasileira de industrias de EEE) and FECOMERCIO-SP (Federação do comércio do Estado de São Paulo) [7].

Even with several initiatives, this situation in Brazil is critical and, it is far from ideal. The e-waste recycling rate is estimated at 2% and, the majority of the take-back routes are located in the Southeast and South regions on the country [7]. There are also the individual waste pickers and irregular cooperatives that collect the e-waste from households or business, dismantle and separate the most valuable components and, the remaining is discarded in inappropriate places (parks, vacant lots, green areas) being very dangerous for environment [7].

Why is it so important recycle this e-waste? The EEE is an important source of secondary raw material. There are up to 69 elements from the periodic table in the EEE composition including precious metals, critical raw materials and non-critical metals [1]. In addition, the primary mining has been suffering problems with availability, access to resources, material scarcity and market price fluctuations [1]. Even though it is a challenge, it is important to improve recycling and reduce the pressure on primary sources. With the material collected in 2019 (17.4%), 4 Mt of secondary material would be available again totalizing $10 billion USD [1].

In addition to being considered a rich source of material, the e-waste contains hazardous substances as potential toxic elements (mercury, cadmium, lead) and, chemicals such as chlorofluorocarbons (CFCs), hydrochlorofluorocarbons (HCFCs) and flame retardants. Therefore, high levels of environmental pollution have been achieved with the improper disposal of e-waste and the extraction of precious metals. The hazardous substances contaminate soil, air and water, and consequently, the human health [5,8]. Landfill is the most common destination for disposal, and toxic metals can leach through the soil into underground water streams, contaminating the soil, lakes and rivers nearby these regions, resulting in contamination of the food chain and sources of water [5,8]. The inadequate combustion of these materials, mainly for extraction of precious metals, contaminate the air in burning sites with fly ash of burnt e-waste, being highly toxic [8]. For human health, this can lead chronic disease and, in some cases, could be lethal [8]. An alert is for e-waste workers, who could carry toxic contamination from work to home, increasing the exposure of their families [9].

1.2. Hard disk (HD) sample

The hard disk (HD), the part of the computer where the data is stored, was studied in this thesis. Figure 1 shows the HD components. The data is read and recorded by the head on the platters, and the rotation motor is responsible for maintaining a platter constant rotation. The head is attached to an arm, which is moved by actuator, being a mechanism that acts by electromagnetic attraction and repulsion. In the back part, there is the logic board that is the interface with the motherboard, controls the rotation of the motor and the movement of the read head [10]. Thus, two components were investigated: the high-performance magnets and the printed circuit board (PCB).

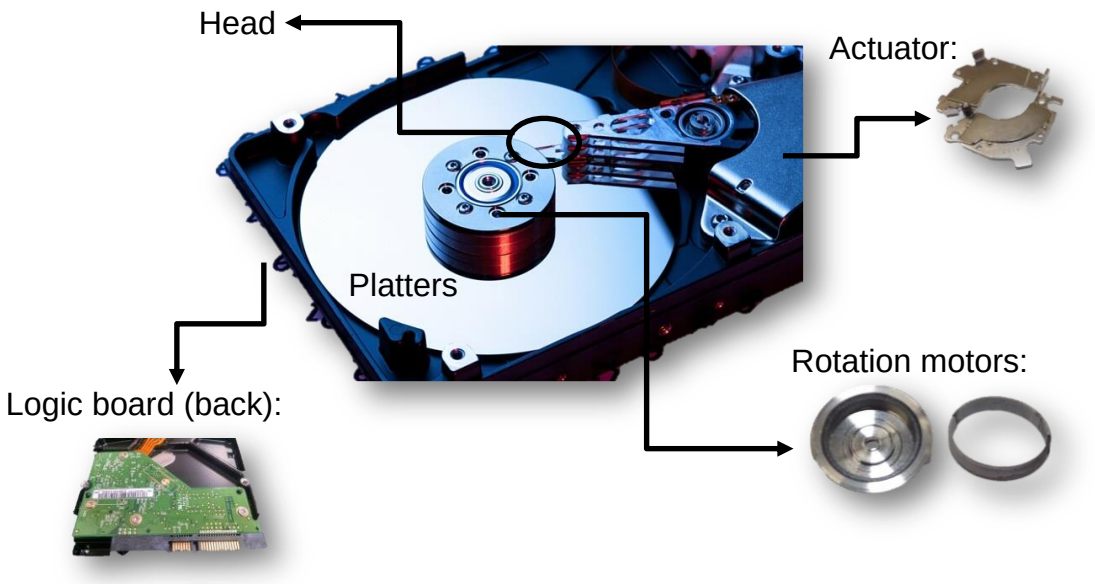

Figure 1. Hard disk components.

The magnets are present in the actuator and the rotation motor and, they are composed of Nd-Fe-B alloy, which have a huge amount of rare earth elements (REEs) including Dy, Gd, Nd, Pr, Sm and Tb [11]. The REEs present magnetic, catalytic, electronic and optical characteristics and they are composed of 15 lanthanides, yttrium and scandium [11,12]. With a demand higher than supply, the REEs are found in the list of the critical raw materials for the European Union [13]. In addition, the most REEs are mined and concentrated in China (extracted and produced locally) with 90% of the world's REEs. This was a problem in the pandemic because the global production had suddenly stopped,

which made the producers realize the dependence of only one country for obtaining REEs [14]. Other point is the production of electrical vehicles, which use Nd to produce magnets to the motors. According to British Broadcasting Corporation (BBC) news, Netherlands aims not to sell new fossil-fuel cars after 2025, United Kingdom and France have planned to achieve this target by 2040 [14]. With this, the demand by REE will increase considerably and, the search by new technologies, such as recycling, can also increase [14].

The PCB is a device made by multilayer or single layer of polymers and fibrous materials (glass fiber) covered by a layer of Cu, where the conductive lines are printed and, electronic components are mounted on the board [15,16]. This sample present many chemical elements, such as hazardous substances including brominated flame retardants (BFR) and lead used on the solder material. Nowadays, there is the search for free-Pb solder material and, in European Union the materials with Pb are banned [17]. On the other hand, there are other chemicals elements with high added value, such as precious metals including gold, silver and the platinum group metals (PGMs), with good electrical conductivity, high melting point and corrosion resistance [12]. For electronic industry, these metals increase the storage capacity in computer's HD [12]. In addition, Al and Cu are other interest elements for recycling being present in high concentration on PCB.

1.3. The role of analytical chemistry

The recycling process is a challenge, mainly due to the complexity of the EEE with its versatile shape, size and composition and, the role of analytical chemistry is to try overcome these challenges and improve the process [18]. But, how is this possible?

(1) Waste characterization to optimize the process: it is growing the search by rapid measurement technologies for elements identification on the sample. For example: Waste electrical and electronic equipment (WEEE) polymers characterization and identification. Costa et al. [19] used LIBS to identify and propose classification models for six polymers and predictive analytical capabilities from 92 to 98% of correct predictions were acquired [18].

(2) Characterization of the efficiency and toxicity of the process; characterization of the purity and properties related to recycled products [18].
(3) Development of analytical procedure for classic recycling [18].
(4) New recycling methods using greener sample treatment and analytical procedures, focusing on sustainable processes. This is still a challenge, since any waste treatment will have an environmental risk, the question is to try minimize that risk [18].

Due to data protection, the most collected HDs are ground, losing information of elements with low concentration. On the other hand, the manual disassembly is a fundamental process to avoid losses of material. Sprecher et al. [20] investigated the production of 1 kg of Nd magnet with three different processes: (1) from primary production and recycling process using two routes (2) manual disassembly and (3) shredding. As conclusion of this study, the recycling process obtained adequate results from the environmental point of view in relation to primary production and, using the manual disassembly avoided loss of material.

It is possible to find in the literature different recycling routes for the magnets from HD: hydrometallurgical process using leaching with inorganic acid (diluted and concentrated acids) [21–28], leaching with organic acid (citric, malic, acetic, maleic, glycolic and L-ascorbic) [29–31], characterization by direct analysis using x-ray fluorescence (XRF) [32]; use of hydrogen as a processing agent to decrepitate sintered magnets [33] and, green method using water and sodium chloride for REE recovery with hydrothermal treatment [34]. On the other hand, there is no environmentally safe route, the best way to follow all the principles of green chemistry is re-use if the magnet is intact.

For the PCB, there are also many options to recycling. First is the pre-treatment as a crucial step with manual disassembly, comminution or/and classification [35], followed by pyro [16,36] or hydrometallurgical [25,37] processing. And the last step is the recovery and purification with solvent extraction, precipitation or cementation [38].

1.4. The purpose

The purpose of this thesis was the characterization of high-performance magnet and the PCB from hard disk. As mentioned before, the characterization is an important part of the recycling process, in which it is possible optimize the process besides to determine the material composition. Three analytical techniques were used: inductively coupled plasma optical emission spectroscopy (ICP OES), laser-induced breakdown spectroscopy (LIBS) and wavelength dispersive x-ray fluorescence (WD XRF). Therefore, the goal was to propose reference methods using ICP OES with simple procedures and, with direct analysis techniques (LIBS and WD XRF) was presented fast methods for characterization. Therefore, alternative calibration models (univariate and multivariate) were proposed to both techniques. In addition, the use of chemometrics was extremely valuable to know the characteristic of the samples.

Chapter 2: Characterization of the samples using ICP OES

2. Characterization of the samples using ICP OES

One of the most used analytical techniques to determine the composition of material from WEEE is ICP OES. For the PCB, the ICP techniques cover approximately 60% of available data sets [39].

This technique is already well established in the literature. First, there is the liquid sample introduction through the peristaltic pump until the nebulizer chamber, where there are sample and argon input. When both come into contact, an aerosol is formed and, small particles go to the plasma and the bigger ones are discarded. The plasma is formed in the torch by Ar gas after a spark in the Tesla coil, where the Ar gas is ionized and the free electrons are accelerated by radio frequency field and, collide with atoms, keeping the temperature on the plasma. The sample is dragged to the plasma by Ar gas and, in this path to the plasma, occurs the desolvation of the sample. With the energy received, the molecules are dissociated and, the process of atomization, excitation and ionization occurs. The plasma light is taken to spectrometer and detector, where there is the simultaneous determination of analytes of the sample [40].

Low background radiation, low limits of detection, possibility of multi elementary analysis, wide linear range and few interferences are some characteristics of ICP OES. On the other hand, it is necessary special care with sample preparation avoiding contamination, high dissolved solids content and the acidity content [40]

In this chapter, it is shown two studies using the ICP OES:

2.1. Characterization of the high-performance magnets with the proposition of a simple method using diluted acid and digestor block.

2.2. Characterization of the printed circuit board from hard disk using a sample preparation without milling, approaching an exploratory analysis.

2.1. Spectroanalytical method for evaluating the technological elements composition of magnets from computer hard disks

Talanta 189 (2018) 205–210

Contents lists available at ScienceDirect

Talanta

journal homepage: www.elsevier.com/locate/talanta

Spectroanalytical method for evaluating the technological elements composition of magnets from computer hard disks

Jeyne Pricylla Castro, Edenir Rodrigues Pereira-Filho*

Group of Applied Instrumental Analysis, Chemistry Department, Federal University of São Carlos, P. O. Box 676, 13565-905 São Carlos, São Paulo State, Brazil

ARTICLE INFO

Keywords:
E-waste
Sample preparation
ICP OES
Rare earth elements
Hard disk
Recycling

ABSTRACT

In this study, inductively coupled plasma optical emission spectrometry (ICP OES) was used for the development of an analytical procedure for elemental analysis of hard disks (HDs). More than 50 samples were acquired and separated according to the manufacturers. Both magnets were used, namely, the actuator (a) and the spindle (s) motor. The samples were heated to remove magnetism, ground in a knife mill and sieved. Different digestion procedures were performed with a block digester and microwave, and three acid concentrations were employed. Due to the lack of certified materials or references from HDs, tests of standard addition and recovery were performed to verify the accuracy of the proposed method. Hyperspectral image and principal component analysis were also used to assist in the data treatment related to the Ni layer. For both magnets, the best analytical procedure was 100 mg of sample, 7 mol L^{-1} nitric acid and a digester block. The elements observed in the highest concentrations were Fe followed by Nd and Pr. This procedure was simpler than others were and prioritized the principles of green chemistry.

1. Introduction

Environmental contamination by incorrect disposal of electronic equipment and its components is one of the largest problems derived from modern human activities [1]. These materials are named e-waste or WEEE and are the residue type with the highest growth on a global scale. The term “e-waste” is used for all electrical and electronic equipment (EEE) discarded without the intention of reuse [2].

EEE include toxic elements in their composition, which can contaminate the environment and affect human health when improperly discarded [3–5]. Conversely, EEE contain several noble and rare earth elements (REEs) with industrial, technological and strategic importance [6]. Therefore, e-waste has the potential to become an important source of resources using methods or strategies for the recovery of specific elements, minimizing the environmental impact and improving the economy in several countries [7].

Computer hard disks (HDs) are a component where data are stored. The HD is a highly complex computer component with several parts composed of plastic, metals, printed circuit boards (PCBs) and two types of magnets: (1) actuator and (2) spindle motor. In this study, both magnets were analytically interrogated due to the rich and strategic REE composition [8]. Actuator magnets move the reading arm, and spindle motor magnets are responsible for maintaining a constant rotation of the disk. These magnets are composed of a Nd-Fe-B alloy, which includes a large amount of REEs [8]. REE, due their electronic configurations, have several technological characteristics, such as magnetism, luminescence, optical, electrical and thermal properties [9,10].

The scientific literature regarding this type of sample is notably scarce, and only a small number of examples were found and are presented in the following. Ueberschaar and Rotter [11], for instance, presented a sample preparation procedure for further determination of 14 analytes using inductively coupled plasma optical emission spectrometry (ICP OES). In the mineralization protocol, nitric acid and aqua regia were used for the actuator and spindle motor magnets, respectively, and the process was accomplished using microwave-assisted dissolution. The authors used a concentrated acid mixture (aqua regia) with a large amount of sample for more than 10 h, and only microwave-assisted dissolution was tested. The whole procedure makes the sample preparation process longer and limited to a small number of laboratories. In addition, the authors did not report important details regarding magnet characterization, such as the method's limits of detection and evaluation of its efficiency with certified reference material or standard addition and recovery tests.

Habib et al. [8] described a method for the direct analysis of actuator magnet composition using wavelength dispersive X-ray fluorescence (WD XRF). The authors found approximately 30% Nd, 5% Pr, and 2% Dy, and the balance was mainly Fe. Low-concentration elements in

* Corresponding author.
E-mail address: erpf@ufscar.br (E.R. Pereira-Filho).

https://doi.org/10.1016/j.talanta.2018.06.062
Received 2 May 2018; Received in revised form 18 June 2018; Accepted 19 June 2018
Available online 20 June 2018
0039-9140/

the range of mg/kg were not determined.

Munchen et al. [12] published a study where a thermal demagnetization process was described for the magnets magnetic field elimination. The samples were ground in a knife mill, and the digestion used the 3051 A method as described by the United States Environmental Protection Agency (US-EPA). Nd, Fe and B were determined by ICP OES, and the Ni coating layer composition was investigated by WD XRF. As can be noted, the scientific literature regarding this type of important sample is limited, and a systematic investigation could shed light on this problem, such as the effects of acid composition, the use of different and inexpensive sample preparation instruments and the chemical concentration of minor elements.

Currently, analytical chemistry represents an important role by providing qualitative, quantitative, temporal and spatial results on the chemical composition of matter [13]. Several applications have already been published targeting polymers, printed circuit board (PCB), mobile phone classifications, and chemometric application in this field [14–20]. The goal of the present study is the development of a reliable analytical procedure for the characterization of both HD magnets, considering the principles of green chemistry and minimum sample preparation. The results presented can help recycling companies improve their HD and e-waste recovery processes. In addition, more than 50 HD samples from different countries were collected, permitting a global chemical view of this material. The experimental part was mainly devoted to REE determination, and Nd alone represents a market of approximately 100 dollars/metric ton for its oxide [21].

2. Experimental

2.1. Sample collection, organization and preliminary preparation steps

In this study, 56 hard disk samples and a group of 6 actuators were collected from old laptop and desktop computers. These samples were manufactured in Brazil, China, Malaysia, Korea, Singapore and Thailand from 2001 to 2014. Nine different manufacturers (M1 – M9) were identified. The sample preparation procedure was divided into three steps. The first step was the HD disassembly. The main HD parts identified are presented in Fig. 1: original (a) and open (b) HD, platters (c), magnets (d), heads (e) and logic PCB (f).

Both magnet types (Fig. 1, part d) were used in this study. The second step was the elimination of the sample magnetic field. In this step, the samples were heated in a furnace at 500 °C for approximately two hours. These magnets have high resistance to demagnetization, losing the magnetic field if they are heated above the Curie temperature (~ 312 °C) [12].

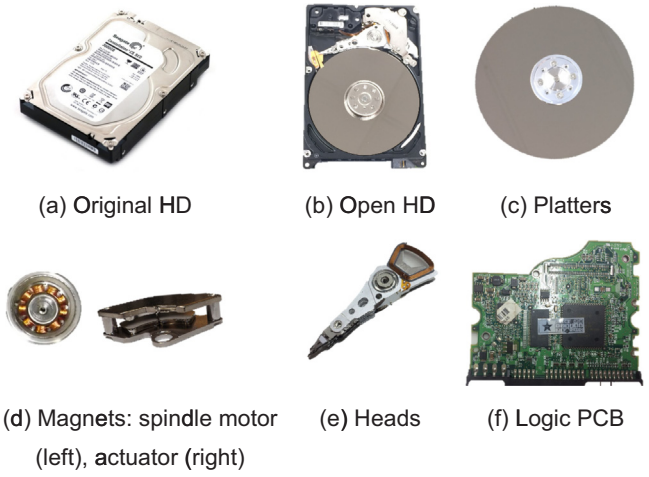

Fig. 1. Computer HD sample disassembly (a and b) with the presentation of main components: platters (c), magnets (d), heads (e) and logic PCB (f).

Table 1
Sample characteristics (country origin and manufacturer codification, M1-M9 and unidentified) for each magnet studied: actuator (a) and spindle motor (s).

Sample identification	Quantity of sub-samples	Country origin	Manufacturer codification
1a[a] and 1s[b]	12	Brazil	M1
2a and 2s	6	Korea and two unknown	M1
3a and 3s	13	China	M2
4a and 4s	7	Brazil, Singapore and Thailand	M2
5a and 5s	7	China, Singapore and Thailand	M3
6a and 6s	5	Malaysia and Thailand	M4
7a and 7s	6	China, Singapore and Thailand,	M5 – M9
8a	6	Unidentified	Unidentified

[a] Magnets from the actuator.
[b] Magnets from the spindle motor.

The third step was sample milling. In this case, the magnets were combined in groups from 5 to 13 individual sub-samples in order to have sufficient volume for the milling process. The criteria used for sample categorization was the magnet's manufacturer. Table 1 shows the samples for each group of magnets.

The sub-samples were ground in a knife mill (IKA, A11), and the particle size was estimated through the use of a 500-μm sieve.

2.2. Reagents and sample digestion procedure

The literature is scarce in analytical procedures for HD analysis. Therefore, some digestion tests with concentrated or diluted HNO_3 (Synth, Diadema, São Paulo State, Brazil) were evaluated. The acid used was purified in a sub-boiling distillation system, Distillacid™ BSB-939-IR (Berghof, Eningen, Germany). In all experiments, 100 mg of sample was weighed, and 10 mL of acid mixture was used. Three different concentrations of acid were tested: 7 mol L^{-1} (one part of acid + one part of deionized water), 9 mol L^{-1} (two parts of acid + one part of deionized water) and 14 mol L^{-1} (only the concentrated nitric acid). The digestions were performed in a microwave system (Speedwave four, Berghof, Eningen, BW, Germany) and a digester block (Marconi, Piracicaba, São Paulo State, Brazil) to compare both digestion methods. The heating program used in the microwave is described in Table 1S in the Supplementary material and was accomplished with three steps. For the digester block, perfluoroalkoxy (PFA) closed tubes with an inner volume of 50 mL (Savillex, MN, USA) were used, and the heating program constituted two hours at 100 °C.

The final volume was made 50 mL with deionized water (Milli-Q®, Millipore, Bedford, MA, USA), and a number of consecutive dilutions were performed. ICP OES (Thermo Scientific, iCAP 6000) with the axial view was used to determine Al, B, Co, Cu, Dy, Fe, Gd, Nd, Ni, Pr, Sm, Sn, Tb and Zn. The maximum sample and standard acidity was 10% to avoid compromising the physical integrity of the ICP OES components. These experiments were made only for sample 3 of the actuator (3a) magnet (see Fig. 1 and Table 1 for details).

The limits of detection (LOD) and quantification (LOQ) for both sample preparation procedures were calculated using equations from (1) to (4) [22].

$$SBr = \frac{(I_{standard} - I_{blank})}{I_{blank}} \quad (1)$$

$$BEC = \frac{C_{standard}}{SBr} \quad (2)$$

$$LOD = \frac{3 \times BEC \times RSD}{100} \quad (3)$$

$$LOQ = \frac{10 \times BEC \times RSD}{100} \quad (4)$$

where

SBr is the signal-to-background ratio.

BEC is the concentration equivalent of the background.

RSD is the relative standard deviation.

The best digestion method was applied to the other samples (Table 1). To verify the accuracy of the proposed method, standard addition and recovery tests were performed because there are not available certified materials or references for this type of sample. In these experiments, known concentrations of analytes in two samples of each magnet (1a, 3a, 1s and 3s) were added before the mineralization process. However, as the concentrations of Fe, Nd and Pr were very high, the addition of these elements was performed in the liquid extract obtained after the mineralization process. The final concentrations after standard addition were two-fold higher the net concentration of each analyte. ICP OES instrumental parameters are shown in Table 2S in the Supplementary material, as well as the standard concentrations for each analyte.

For data treatment and evaluation of the results, some chemometric strategies, such as principal component analysis (PCA) and paired *t*-test for multiple samples, were used. All experiments were performed in triplicate (n = 3).

2.3. Hyperspectral images

Direct analysis of the actuator magnets was performed using a laser-induced breakdown spectroscopy (LIBS) instrument (Applied Spectra, model J200, California, USA) in an area with four lines and five columns (approximately 1.5 by 2.0 mm) in order to obtain a hyperspectral image and verify the chemical composition and certain special features. A total of 20 points were analyzed, and five pulses were performed *per* point (100 spectra were obtained).

The actuator magnets have a Ni coating layer to prevent Fe oxidation that might jeopardize the HD performance. Before the analysis, part of the Ni layer was mechanically removed. In the LIBS system, 85 mJ of laser pulse energy, 75 μm spot size and 0.5 μs of delay time were used. The fluence, power and irradiance were approximately 2000 mJ/cm^2, 1.7 × 10^7 W and 400 GW/cm^2, respectively. After LIBS data recording, the most intense Nd and Ni emission lines (11 lines) were selected, the signal height was calculated, and the data were normalized by the Euclidean norm and auto-scaled. All data organization, treatment and calculations were performed in Microsoft Excel®, MATLAB 2017b (Matworks, Natick, MA, USA) and Pirouette version 4.5 (Informetrix, Bothell, WA, USA).

3. Results and discussion

3.1. Actuator magnets

All samples collected and described in Table 1 were heated above the Curie temperature to eliminate the magnetic field. After heating, the samples were milled, and the particle size was lower than 500 μm for 85% of the sample particles.

Initial tests were performed with sample 3a (actuator). Table 2 shows the results obtained by ICP OES determination for the analytes and its standard deviations for three different concentrations of HNO_3 using the microwave and digester block. There was no visual difference among the digested solutions with three different acid concentrations; therefore, all of the mixtures presented similar results. Fe was present at the highest concentration (approximately 60%) in the magnet followed by certain REEs, such as Nd, Pr and Dy. All the calculated RSD values were below 20%, except for that of Ni, which was 35% (HNO_3 14 mol L^{-1}, microwave). According to these results, it is possible to observe a similarity between the analytical procedures.

Therefore, a paired *t*-test was performed to compare the solutions of the different concentrations of HNO_3 and the different digestion methods (microwave and digester block). There were no significant differences using the 95% confidence level.

According to the previously presented results, the mineralization procedure chosen for further sample preparation was 100 mg of sample, 10 mL of 7 mol L^{-1} HNO_3 (the lowest acid concentration), experiments in triplicate and two hours of heating at 100 °C in the digester block (the less expensive sample preparation instrument). This analytical procedure was applied to the other samples (see Table 1).

The limits of detection and LOQ were also compared using both sample preparation strategies (microwave and digester block); Table 3 shows these results, but only for HNO_3 7 mol L^{-1}. A paired *t*-test was also performed to compare the limits obtained for all analytes simultaneously and between both methods. Despite the differences observed for Cu, after *t*-test evaluation for all analytes there was no significant difference at the 95% confidence level.

Table 4 shows the concentration range for all the elements determined in the actuator (a, see details in Table 1) samples (lower and higher value between the samples). In addition, the table shows the element recovery for two samples (1a and 3a).

The concentrations among the different samples were in average very similar, varying from 0.021% for Zn to 62% for Fe. All values of RSD for all the samples and elements were below 20%. The sample 1a recoveries varied from 87% for B to 106% for Cu, while those for sample 3a varied from 82% for B to 105% for Cu. These recovery values

Table 2
Comparison of the results (% w/w) from ICP OES after using different digestion methods (microwave oven and digester block) and acid concentrations for the actuator magnet (sample 3a).

Elements	Microwave			Digester block		
	HNO_3 7 mol L^{-1} (% m/m)	HNO_3 9 mol L^{-1} (% m/m)	HNO_3 14 mol L^{-1} (% m/m)	HNO_3 7 mol L^{-1} (% m/m)	HNO_3 9 mol L^{-1} (% m/m)	HNO_3 14 mol L^{-1} (% m/m)
Al	0.69 ± 0.02	0.71 ± 0.02	0.71 ± 0.02	0.69 ± 0.01	0.67 ± 0.03	0.73 ± 0.02
B	0.76 ± 0.01	0.77 ± 0.04	0.77 ± 0.02	0.75 ± 0.01	0.75 ± 0.02	0.77 ± 0.02
Co	0.73 ± 0.01	0.72 ± 0.01	0.75 ± 0.03	0.70 ± 0.02	0.72 ± 0.02	0.74 ± 0.04
Cu	0.19 ± 0.01	0.17 ± 0.01	0.19 ± 0.03	0.21 ± 0.01	0.19 ± 0.01	0.20 ± 0.02
Dy	1.71 ± 0.08	1.74 ± 0.03	1.8 ± 0.1	1.74 ± 0.05	1.73 ± 0.06	1.97 ± 0.05
Fe	65 ± 2	65 ± 2	64 ± 1	60 ± 1	65 ± 1	66 ± 4
Gd	0.151 ± 0.003	0.150 ± 0.008	0.152 ± 0.004	0.150 ± 0.002	0.158 ± 0.004	0.167 ± 0.005
Nd	25 ± 1	25 ± 1	25 ± 1	23.0 ± 0.4	25.0 ± 0.4	26 ± 2
Ni	2.6 ± 0.4	1.8 ± 0.3	1.8 ± 0.6	3.3 ± 0.5	3.1 ± 0.2	2.8 ± 0.4
Pr	3.2 ± 0.1	3.38 ± 0.01	3.3 ± 0.1	3.13 ± 0.08	3.3 ± 0.1	3.5 ± 0.2
Sm	0.32 ± 0.01	0.31 ± 0.02	0.48 ± 0.03	0.30 ± 0.01	0.31 ± 0.01	0.31 ± 0.01
Sn	0.613 ± 0.005	0.61 ± 0.03	0.629 ± 0.008	0.58 ± 0.01	0.58 ± 0.02	0.60 ± 0.01
Tb	0.23 ± 0.03	0.20 ± 0.02	0.21 ± 0.01	0.19 ± 0.02	0.204 ± 0.003	0.18 ± 0.02
Zn	0.020 ± 0.002	0.017 ± 0.002	0.018 ± 0.003	0.024 ± 0.002	0.022 ± 0.001	0.024 ± 0.002

Table 3
Limits of detection and quantification (mg kg^{-1}) for both digestion methods (microwave and digester block) for mineralization with 7 mol L^{-1} HNO_3.

Elements	Microwave		Digester Block	
	LOD (mg kg^{-1})	LOQ (mg kg^{-1})	LOD (mg kg^{-1})	LOQ (mg kg^{-1})
Al	0.07	0.2	0.09	0.3
B	0.07	0.2	0.03	0.09
Co	0.006	0.02	0.004	0.01
Cu	0.03	0.09	0.3	1
Dy	0.002	0.007	0.002	0.008
Fe	0.02	0.06	0.05	0.2
Gd	0.02	0.05	0.02	0.05
Nd	0.02	0.07	0.02	0.06
Ni	0.002	0.007	0.007	0.02
Pr	0.01	0.03	0.008	0.03
Sm	0.03	0.1	0.03	0.1
Sn	0.2	0.6	0.06	0.2
Tb	0.002	0.005	0.003	0.008
Zn	0.02	0.06	0.09	0.3

were between the acceptable range of 80–120%, showing the efficiency of the proposed method.

The same standard addition test was repeated for the other samples and for some selected analytes. The recovery values varied from 89 (B) to 134% (Cu) and more details can be observed in Table 3S.

In the case of Ni, it was not possible to calculate the recovery because this element is the main constituent of the coating layer that was not removed before milling; therefore, the concentration values of Ni were uneven due to the particle size and homogenization difficulties encountered with the samples.

In this manner, the Ni behavior was studied in detail using hyperspectral images. An area of 1.5 by 2.0 mm was analyzed using LIBS; 20 points and 5 laser pulses *per* point were performed.

Fig. 2a shows the actuator magnet image and a magnification of the ablated area (4 by 5 points). A PCA was calculated for each pulse layer; Fig. 2b shows a score map obtained for the first principal component (PC1) and for the second pulse. As can be noted, there is a clear difference in the surface. Fig. 2c shows the emission lines that characterize each region (blue and yellow). The yellow part (positive score values) is the magnet with the coating layer and is related to Ni emission lines. The blue part (negative score values) represents the magnet without the coating layer (related to Nd emission lines).

3.2. Spindle motor magnet

For this magnet, the same actuator magnet sample preparation procedure was made. After heating and milling, the samples were sieved, and 93% of the particles were smaller than 500 μm.

The best mineralization procedure chosen (7 mol L^{-1} HNO_3) for the actuator magnet was applied to the spindle motor samples (s, see details in Table 1). The results (concentration range and recovery of the elements) by ICP OES are shown in Table 4. These samples do not have Ni as the coating layer; therefore, its concentration is notably low (approximately 100 mg/kg on average). The concentration varied from 0.011% for Ni to 63% for Fe. The highest element concentrations were for Fe, followed by Nd, Pr and Co, where the remaining elements are lower than 1% m/m. In the case of Tb, it was not possible to determine this element in these samples, as the results were lower than the LOD (see Table 4). The recoveries were in the acceptable range from 80% to 120%, except for Sn in the 3 s sample, which was 68%. The RSD values for this magnet were below 20%, except for the Ni. Table 3S shows the recovery values for the remaining samples.

Visually, the spindle motor samples were not digested completely, remaining as a solid residue. Therefore, a more drastic acid mixture consisting of 5 mL of aqua regia (HNO_3 and HCl in a 1:3 ratio) was tested. This mineralization was made with 100 mg of sample 1 s, in triplicate, with two hours in the digester block at 100 °C. The solutions were analyzed by ICP OES, and the results are shown in the Table 5.

According to Table 5, it can be observed that the results are very similar between the digestions with 7 mol L^{-1} HNO_3 and concentrated aqua regia. A paired *t*-test was calculated, and there was no significant difference at the 95% of confidence level. In this mineralization, the sample was digested completely. Therefore, the solid residue observed in the samples prepared with HNO_3 did not influence the determined elements.

3.3. Comparison between the two magnets

PCA was used for data set exploration. The data were auto-scaled, and three factors were selected with a cumulative variance of 84%. Fig. 3 shows simultaneous scores (red squares and blue circles) and loadings (black squares). The scores plot shows a clear separation between both magnets, the spindle motor (blue circles) and the actuator (red squares). Confidence ellipses with 95% of confidence level [23] were calculated for both types of magnets, and different chemical profiles are confirmed.

According to PC1, Sn and Ni were the elements that most characterized the spindle motor and actuator magnets, respectively. The Ni

Table 4
Concentration range of samples and the recovery of elements determined by ICP OES for actuator (1a – 8a) and spindle motor (1s–7s) magnets.

Elements	Results for actuator (samples 1a – 8a)					Results for spindle (samples 1s–7s)				
	Range (% m/m)			Recovery (%)		Range (% m/m)			Recovery (%)	
	Lower	Higher	Overall average	Sample: 1a	Sample: 3a	Lower	Higher	Overall average	Sample: 1s	Sample: 3s
Al	0.392 ± 0.002	0.50 ± 0.01	0.44	90	84	0.099 ± 0.002	0.56 ± 0.02	0.28	108	102
B	0.63 ± 0.05	0.710 ± 0.001	0.66	87	82	0.64 ± 0.02	0.75 ± 0.01	0.67	96	90
Co	0.48 ± 0.02	1.65 ± 0.06	0.89	88	89	0.34 ± 0.01	3.00 ± 0.03	1.41	90	81
Cu	0.135 ± 0.003	0.40 ± 0.03	0.22	106	105	0.040 ± 0.002	0.06 ± 0.01	0.05	93	89
Dy	0.72 ± 0.05	1.8 ± 0.1	1.21	99	83	0.035 ± 0.001	0.045 ± 0.003	0.04	97	87
Fe	59 ± 1	64 ± 1	62	100	102	58 ± 4	68 ± 1	63	109	104
Gd	0.090 ± 0.008	0.106 ± 0.004	0.10	92	81	0.076 ± 0.001	0.112 ± 0.004	0.10	93	88
Nd	24 ± 1	26.00 ± 0.05	25	99	99	16 ± 1	24 ± 1	21	108	102
Ni	1.37 ± 0.05	3.3 ± 0.3	2.12	–	–	0.0054 ± 0.0003	0.016 ± 0.003	0.011	103	99
Pr	2.2 ± 0.1	3.9 ± 0.1	3.1	93	95	0.464 ± 0.004	4.0 ± 0.2	2.3	117	117
Sm	0.31 ± 0.01	0.376 ± 0.001	0.34	96	85	0.29 ± 0.01	0.339 ± 0.005	0.31	95	91
Sn	0.059 ± 0.001	0.102 ± 0.003	0.09	93	91	0.28 ± 0.01	0.44 ± 0.01	0.38	82	68
Tb	0.0182 ± 0.0004	0.53 ± 0.03	0.24	104	85	< LOD	< LOD	–	–	–
Zn	0.018 ± 0.001	0.026 ± 0.003	0.021	89	95	0.0073 ± 0.0001	0.0187 ± 0.0002	0.012	99	96

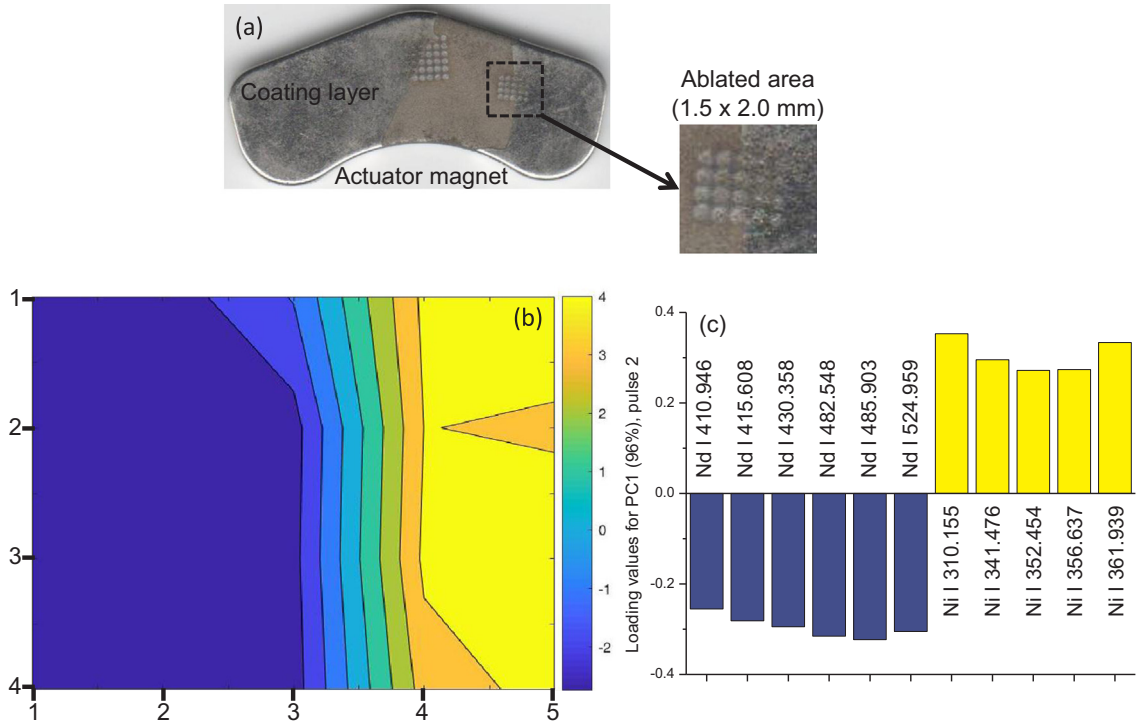

Fig. 2. Image of actuator magnet analyzed by LIBS (a), score map (b) and loadings plot (c). For interpretation of the references to color in this figure legend, the reader is referred to the web version of this article.

Table 5
Comparison between the digestion procedures with 7 mol L^{-1} HNO_3 and concentrated aqua regia for sample 1 of the spindle motor magnets (1 s).

Elements	Nitric acid (% m/m)	Aqua regia (% m/m)
Al	0.24 ± 0.01	0.333 ± 0.005
B	0.65 ± 0.01	0.65 ± 0.01
Co	0.94 ± 0.02	0.98 ± 0.02
Cu	0.041 ± 0.001	0.041 ± 0.001
Dy	0.035 ± 0.001	0.0361 ± 0.0003
Fe	64 ± 2	66.0 ± 0.4
Gd	0.099 ± 0.003	0.102 ± 0.001
Nd	22 ± 1	22.0 ± 0.2
Ni	0.0059 ± 0.0004	0.0081 ± 0.0002
Pr	2.13 ± 0.05	2.23 ± 0.02
Sm	0.30 ± 0.01	0.334 ± 0.002
Sn	0.39 ± 0.01	0.506 ± 0.001
Zn	0.0102 ± 0.0001	0.015 ± 0.002

behavior is explained by the coating layer of the actuator magnet (see details in Fig. 2). Ni is not present in the spindle motor magnet due to other manufacturing methods. Sn is added to both magnets in small concentrations.

There is no difference in the principle of converting electrical energy into motion through the magnetic field between both the magnets, but in the spindle motor, the motion is rotary, and the actuator motion is from side to side. However, there is a difference in the manufacturing method [24].

The spindle motor magnets are bonded by polymers, mixing the Nd-Fe-B powder with a special binder and allowing the magnets to be pressed easily and precisely to a final shape, which are considered isotropic compounds. This property justifies why this sample did not digest completely with 7 mol L^{-1} HNO_3. Actuator magnets, which employ anisotropic sintered Nd-Fe-B permanent magnets, are produced without a binder and are easier to mineralize when compared with that of spindle magnets [24].

Certain REEs and other alloying elements are added to the magnets

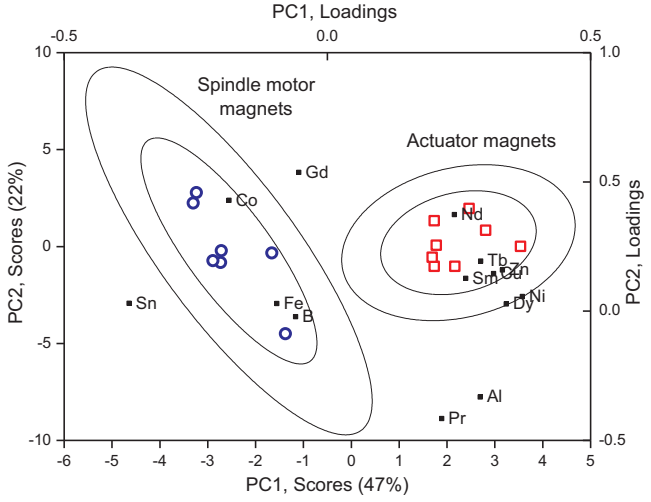

Fig. 3. Scores and loadings (black squares) of the two magnet element concentrations: actuator (red squares) and motor magnets (blue squares), and its respective confidence ellipses. (For interpretation of the references to color in this figure legend, the reader is referred to the web version of this article.).

to improve physical properties. The addition of Co can increase the Curie temperature, substituting some of the Fe present. Dy can improve the stability at high temperatures and prevent demagnetization, but it does not raise the Curie temperature of the magnets. Other applications are the substitution of a small amount of Nd by Pr to reduce the manufacturing cost. However, a substitution with more than 20–25% can compromise the performance of the magnet [24].

4. Conclusions

In this study, it was possible to develop an analytical procedure to characterize both the actuator and spindle motor magnets from hard

disks by prioritizing the principle of green chemistry using simpler methods and employing diluted acid. Several acid mixtures were examined, and the best results were obtained with 7 mol L^{-1} HNO_3.

After characterization, the strategic elements can be extracted in the recycling process, thereby minimizing the environmental impact, and can be reused to make new computers and telecommunication tools, batteries for electric cars, flat-screen TVs and other products. In addition, the recycling represents a necessary and economically viable alternative in view of the reduction in available conventional mining areas worldwide.

Acknowledgments

This study was supported by the São Paulo Research Foundation (FAPESP, grants 2012/01769-3, 2012/50827-6, 2014/22408-4, 2016/01513-0 and 2016/17221-8) and Conselho Nacional de Desenvolvimento Científico e Tecnológico (CNPq, 401074/2014-5 and 305637/2015-0).

Appendix A. Supplementary material

Supplementary data associated with this article can be found in the online version at http://dx.doi.org/10.1016/j.talanta.2018.06.062.

References

[1] K. Lundgren, The Global Impact of E-Waste: Addressing the Challenge, International Labour Office, SafeWork and SECTOR, Geneva, 2012.
[2] C.P. Baldé, F. Wang, R. Kuehr, J. Huisman, The Global E-Waste Monitor – 2014, United Nations University, IAS – SCYCLE, Bonn, Germany, 2015.
[3] C. Luo, C. Liu, Y. Wang, X. Liu, F. Li, G. Zhang, X. Li, Heavy metal contamination in soils and vegetables near an e-waste processing site, South China, J. Hazard Mater. 186 (2011) 481–490.
[4] J. Zheng, K.-h. Chen, X. Yan, S.-J. Chen, G.-C. Hu, X.-W. Peng, J.-g. Yuan, B.-X. Mai, Z.-Y. Yang, Heavy metals in food, house dust, and water from an e-waste recycling area in South China and the potential risk to human health, Ecotoxicol. Environ. Saf. 96 (2013) 205–212.
[5] Y. Yang, M. Xue, Z. Xu, C. Huang, Health risk assessment of heavy metals (Cr, Ni, Cu, Zn, Cd, Pb) in circumjacent soil of a factory for recycling waste electrical and electronic equipment, Mater. Cycles Waste Manag. 15 (2013) 556–563.
[6] I. Rucevska, C. Nellemann, N. Isarin, W. Yang, N. Liu, K. Yu, S. Sandnaes, K. Olley, H. McCann, L. Devia, L. Bisschop, D. Soesilo, T. Schoolmeester, R. Henriksen, R. Nilsen, Waste Crime – Waste Risks Gaps in meeting the global waste challenge, UNEP, Norway, 2015.
[7] R.M. Izatt, S.R. Izatt, R.L. Bruening, N.E. Izatt, B.A. Moyer, Challenges to achievement of metal sustainability in our high-tech society, Chem. Soc. Rev. 43 (2014) 2451–2475.
[8] K. Habib, K. Parajuly, H. Wenzel, Tracking the flow of resources in electronic waste – the case of end-of-life computer hard disk drives, Environ. Sci. Technol. 49 (2015) 12441–12449.
[9] P.C.S. Filho, O.A. Serra, Terras raras no Brasil: histórico, produção e perspectivas, Quim. Nova 37 (2014) 753–760.
[10] S. Zhang, Y. Ding, B. Liu, C.C. Chang, Supply and demand of some critical metals and present status of their recycling in WEEE, Waste Manag. 65 (2017) 113–127.
[11] M. Ueberschaar, V.S. Rotter, Enabling the recycling of rare Earth elements through product design and trend analyses of hard disk drives, J. Mater. Cycles Waste Manag. 17 (2015) 266–281.
[12] D.D. Munchen, H.M. Veit, Neodymium as the main feature of permanent magnets from hard disk drives (HDDs), Waste Manag. 61 (2017) 372–376.
[13] M. Valcárcel, Quo vadis, analytical chemistry? Anal. Bioanal. Chem. 408 (2016) 13–21.
[14] M.A. Aguirre, M. Hidalgo, A. Canals, J.A. Nóbrega, E.R. Pereira-Filho, Analysis of waste electrical and electronic equipment (WEEE) using laser induced breakdown spectroscopy (LIBS) and multivariate analysis, Talanta 117 (2013) 419–424.
[15] R.R.V. Carvalho, J.A.O. Coelho, J.M. Santos, F.W.B. Aquino, R.L. Carneiro, E.R. Pereira-Filho, Laser-induced breakdown spectroscopy (LIBS) combined with hyperspectral imaging for the evaluation of printed circuit board composition, Talanta 134 (2015) 278–283.
[16] F.W.B. Aquino, E.R. Pereira-Filho, Analysis of the polymeric fractions of scrap from mobile phones using laser-induced breakdown spectroscopy: chemometric applications for better data interpretation, Talanta 134 (2015) 65–73.
[17] V.C. Costa, F.W.B. Aquino, C.M. Paranhos, E.R. Pereira-Filho, Identification and classification of polymer e-waste using laser-induced breakdown spectroscopy (LIBS) and chemometric tools, Polym. Test. 59 (2017) 390–395.
[18] J.P. Castro, E.R. Pereira-Filho, Twelve diferente types of data normalization for the proposition of classification, univariate and multivariate regression models for the direct analyses of alloys by Laser-induced breakdown spectroscopy (LIBS), J. Anal. At. Spectrom. 31 (2016) 2005–2014.
[19] V.C. Costa, F.W.B. Aquino, C.M. Paranhos, E.R. Pereira-Filho, Use of laser-induced breakdown spectroscopy for the determination of polycarbonate (PC) and acrylonitrile-butadiene-styrene (ABS) concentrations in PC/ABS plastics from e-waste, Waste Manag. 70 (2017) 212–221.
[20] F.W.B. Aquino, C.M. Paranhos, E.R. Pereira-Filho, Method for the production of acrylonitrile– butadiene–styrene (ABS) and polycarbonate (PC)/ABS standards for direct Sb determination in plastics from e-waste using laser-induced breakdown spectroscopy, J. Anal. At. Spectrom. 31 (2016) 1228–1233.
[21] Forecast of rare earth oxide prices worldwide from 2014 to 2025. ⟨https://www.statista.com/statistics/449838/forecast-average-rare-earth-oxide-prices-globally/⟩, (Accessed 18 April 2018), 2014.
[22] F.V. Silva, L.C. Trevizan, C.S. Silva, A.R.A. Nogueira, J.A. Nóbrega, Evaluation of inductively coupled plasma optical emission spectrometers with axially and radially viewed configurations, Spectrochim. Acta Part B 57 (2002) 1905–1913.
[23] F. Husson, S. Le, J. Pages, Confidence ellipse for the sensory profiles obtained by principal component analysis, Food Qual. Prefer. 16 (2005) 245–250.
[24] G. Hatch, Seagate, rare earths and the wrong end of the stick, Technol. Met Res. (2011), ⟨http://www.techmetalsresearch.com/seagate-rare-earths-and-the-wrong-end-of-the-stick/⟩ (Accessed on 12 April 2018).

Spectroanalytical method for evaluating the technological elements composition of magnets from computer hard disks

Jeyne Pricylla Castro and Edenir Rodrigues Pereira-Filho*

Group of Applied Instrumental Analysis, Chemistry Department, Federal University of São Carlos, São Carlos – São Paulo State, Brazil, P. O. Box 676, Zip Code 13565-905

*corresponding author: erpf@ufscar.br
Phone: + 55 16 3351 8092
Fax: + 55 16 3351 8350

Supplementary Material

Table 1S. Microwave heating program used for sample preparation.

Steps	Temperature (°C)	Pressure (bar)	Ramp (min)	Hold time (min)	Maximum power (%)*
1	120	30	5	5	60
2	150	30	5	2	70
3	200	30	5	15	80

* The instrument maximum nominal power is 2000 W.

Table 2S. Instrumental parameters of ICP OES, and emission lines used for analytes determination.

Instrumental Parameters			Operation conditions
Power applied by RF (W)			1150
Nebulizer gas flow rate (L/min)			0.70
Auxiliary gas flow rate (L/min)			0.5
Argon gas flow rate (L/min)			12
Integration time / s			15 for low and 5 for high emission lines
Replicates number			3
Analytes	Standards concentration ranges (mg/L)		Emission Lines (nm)
	Actuator	Spindle motor	
Al	1 to 70	1 to 50	396.152
B	1 to 70	1 to 50	249.678
Co	1 to 70	1 to 50	230.786
Cu	1 to 70	0.1 to 2.5	327.396
Dy	1 to 70	0.1 to 2.5	353.170
Fe	1 to 70	1 to 65	259.940
Gd	1 to 70	1 to 50	335.047
Nd	1 to 70	1 to 50	378.425
Ni	1 to 70	0.1 to 2.5	231.604
Pr	1 to 70	1 to 65	414.311
Sm	1 to 70	1 to 50	330.639
Sn	1 to 70	1 to 50	226.891
Tb	1 to 70	0.1 to 2.5	350.917
Zn	0.1 to 5	0.1 to 2.5	213.856

Table 3S. Addition and recovery test range results obtained for selected analytes in the HD magnet samples

Selected analytes	Recovery range values (%) obtained for all samples tested	Average (%)
B	89 – 102	96
Co	91 – 110	98
Cu	88 – 134	109
Dy	97 – 118	105
Fe	95 – 101	98
Gd	98 – 116	108
Nd	94 – 100	97
Pr	91 – 106	98
Zn	97 – 126	112

2.2. Chemical exploratory analysis of printed circuit board (PCB) using inductively coupled plasma optical emission spectrometry (ICP OES): data treatment and elements correlation

detritus | Multidisciplinary Journal for Waste Resources & Residues

CISA

CHEMICAL EXPLORATORY ANALYSIS OF PRINTED CIRCUIT BOARD (PCB) USING INDUCTIVELY COUPLED PLASMA OPTICAL EMISSION SPECTROMETRY (ICP OES): DATA TREATMENT AND ELEMENTS CORRELATION

Jeyne Pricylla Castro and Edenir Rodrigues Pereira-Filho *

Group of Applied Instrumental Analysis, Chemistry Department, Federal University of São Carlos, São Carlos, São Paulo State, Brazil

Article Info:
Received:
27 April 2020
Revised:
27 July 2020
Accepted:
24 August 2020
Available online:
28 December 2020

Keywords:
Urban mining
PCB element distribution maps
Scores map
Electronic waste
Correlation plot

ABSTRACT

Electronic waste is the fastest growing class of residue in the world. This material presents several electric and electronic equipment (EEE) with a huge amount of base, valuable and toxic elements, thus increasing its recycling interest. This study is aimed to perform an exploratory analysis of printed circuit board (PCB) using Inductively coupled plasma optical emission spectrometry (ICP OES). A PCB from hard disk (HD) was split in 77 sub-samples using a lathe following by mineralization process. This step was conducted without milling process. So, the sub-samples were weighted and mixed with concentrated aqua regia solution, followed by mineralization using microwave oven radiation. Twenty elements were determined by ICP OES (Al, Au, Ba, Ca, Co, Cr, Cu, Fe, Mg, Mn, Nd, Ni, Pb, Pd, Pt, Sb, Sn, Ti and Zn), and Flame atomic absorption spectrometry - FAAS (Ag). With the concentration results, several graphical analyzes were performed: (1) scores map and loading plot; (2) correlation plot and; (3) PCB element distribution maps. With this exploratory analysis, it was possible visualize and understand the data, observing correlations among the elements, how close these correlations are and how is this correlation around the PCB components. This strategy was a good way to observe the PCB complexity and the importance of recycling these materials.

1. INTRODUCTION

Nowadays, around 60 different chemicals elements are found in electrical and electronic equipment (EEE), making this type of material a powerful economic and technological source. While the lifespan of these equipment is decreasing over the years due to the fast-technological development, the amount of electronic waste (e-waste) increases (Baldé et al., 2017; Andrade et al., 2019a; Costa et al., 2018).

The composition of e-waste contains precious metals, valuable bulky materials, rare earth elements (REE), hazardous and scarce metals, being extremely important to recycle these obsolete materials. Initiatives related to recycling avoid health and environmental risks, minimizing impacts caused by primary metal extraction, being also a strategic commercial sector (Zhang et al., 2017; Bookhagen et al., 2018). Therefore, the e-waste should be considered a source of valuable resources, and not a common waste (Cucchiella et al., 2015).

Printed circuit board (PCB) is one type of e-waste, which is found in almost all EEE. It consists of a board composed of layers of polymers and fibrous materials, such as, glass fiber. Conductive lines are printed and, electronic components (transistors, capacitors, integrated circuits) are mounted on the board (Yamane et al., 2011; Cayumil et al., 2018). There are many elements on the PCB, increasing its complexity and heterogeneity, even so, the interest to recycle this type of material increase over the years (Yamane et al., 2011; Cayumil et al., 2018).

It is necessary several steps to recycle this material: pre-treatment (manual disassembling); processing (comminution, granulometric classification, magnetic and electrostatic separation); concentration (pyro and hydrometallurgical processing); recovery and purification (solvent extraction, precipitation/cementation) (Silvas et al., 2015). In the literature, there are some studies that show several recycling routes (Cui & Zhang, 2008; Huang et al., 2009; Park & Fray, 2009; Rao et al., 2020).

In the study proposed by Dervisevic et at., 2013, the quantitative analysis of the PCBs (individual components and complete PCB) from computer and mobile phones

* Corresponding author:
Edenir Rodrigues Pereira-Filho
email: erpf@ufscar.br

Detritus / Volume 13 - 2020 / pages 131-139
https://doi.org/10.31025/2611-4135/2020.14039

were performed using inductively coupled plasma optical emission spectrometry (ICP OES) and x-ray fluorescence (XRF). Besides that, structure and chemical composition, phase transformations and microstructural analysis were performed. In addition, a recycling procedure was proposed observing the effect of the extraction in different parts of PCB before the melting process. The authors suggested also new materials that can replace the harmful ones, as an example, Ga-Sb-Zn as a good lead-free solder material.

Tanvar et al., 2020, evaluate hard disk drive (HDD) as a source of Cu and REE and, performed physical separation in a customized water fluidization classifier for Cu recovery from PCB. The extraction of REE elements from the magnet were performed using microwave exposure-leaching and precipitation route. Another study was performed by Moosakazemi et al., 2020, where the authors proposed a cementation process using waste Al-based heat sinks as cementing agent to precipitate Sn and Pb from the dissolution of PCBs in HCl. El-Nasr et al., 2020, used a leach solution (ammonia salt leaching process) for PCB from old computers to prepare Cu nanoparticle using an ecofriendly and low-cost method with L-ascorbic acid as reductant and stabilizer. Mesquita et al., 2018, described a chemical characterization of connector pins from PCB of computers using Scanning Electron Microscopy – Energy Dispersive Spectroscopy (SEM-EDS) and ICP OES. The authors concluded that, due to leaching procedure of the mixed sample without grinding, the operating costs were reduced and metals recovery were maximized.

Andrade et al., 2019b, prepared a reference material for inorganic constituents on PCB samples. They evaluated different acid mixtures for leaching procedure. Diluted aqua regia presented the best performance using microwave radiation and ICP OES for determination of several elements. Instrumental neutron activation analysis (INAA) was used to compare the results obtained. After that, several characterizations were performed according to ISO Guides 30-35, such as homogeneity, stability (short and long) and chemical characterization of the reference material (Andrade et al., 2019c).

An important aspect in all studies is the characterization of the material and, one of the most used instrumental analytical techniques is ICP OES (Castro & Pereira-Filho, 2018). This technique is already well established, with many advantages such as multielement determination, accurate and precise determinations and, low limits of detection (LODs), being necessary dissolution of the solid samples. In this study, ICP OES was used to analyze a PCB from HDD. The goal was dedicated to exploratory analysis using correlation plot, PCB element distribution maps and, scores maps and loading plot using the concentrations acquired from ICP OES. The images help to interpret and correlate the different elements on the PCB, characterizing this material and collaborating with urban mining.

2. MATERIAL AND METHODS

2.1 Sample preparation, digestion procedure and ICP OES analysis

A PCB from HDD was chosen to perform this study. This PCB was mechanically fragmented in 77 square-shaped sub-samples (11 rows and 7 columns) with the help of a lathe. The size of each fragment was around 1 by 1 cm. To avoid intense sample preparation procedures, the fragments were not crushed and milled, but entirely used. Therefore, it was not possible to obtain replicates due to heterogeneity of the sample. Even for a single manufacturer, PCB's are not exactly the same in composition.

The fragments' weight ranged from 0.41 to 1.63 g, and were separated according to their weights to further mineralization, which was performed using a microwave system (Speedwave four, Berghof, Eningen, BW, Germany). Seven mL of concentrated aqua regia (HNO_3 and HCl in a 1:3 ratio) was used as acid mixture. The acids used were previously purified in a sub-boiling distillation system. Table 1 shows the heating program used in the microwave for DAK 100 tube, that allows up to 100 mL of volume.

After the mineralization, the final solutions volume was completed until 20 mL with deionized water (Milli-Q®, Millipore, Bedford, MA, USA). Consecutive dilutions were performed to ensure that the solutions would be fit for maximum allowed for dissolved solids and acidity. ICP OES (Thermo Scientific, iCAP 7000) was used to determine Al, Au, Ba, Ca, Co, Cr, Cu, Fe, Mg, Mn, Nd, Ni, Pb, Pd, Pt, Sb, Sn, Ti and Zn. The determinations were performed in axial mode, except for Ba and Ca, that were determined in radial mode, due to high concentration of these elements on the sub-samples. Table 2 shows the ICP OES instrumental parameters.

For Ag, Flame Atomic Absorption Spectrometry (FAAS) was used. The FAAS instrument (Varian AA240FS, Mulgrave, Australia) performed the determinations with a hollow cathode lamp of Ag. The spectrometer parameters used were wavelength of 328.1 nm, lamp current of 3 mA (75% of the manufacturer's recommendation), spectral resolution of 0.5 nm in absorbance measurement mode. The flame type was Air-C_2H_2 with a flow of 1.3 L min^{-1}.

Limits of detection and quantification were calculated

TABLE 1: Microwave heating program used for fragments' mineralization.

Steps	Temperature (°C)	Ramp time (min)	Hold time (min)	Percentage of maximum pressure* used (%)
1	120	5	5	60
2	150	5	2	70
3	200	5	15	80

** The maximum pressure is 30 bar*

TABLE 2: Instrumental parameters for ICP OES determinations.

Instrumental Parameters	Operation conditions
Power applied by RF (W)	1150
Nebulizer gas flow rate (L/min)	0.70
Auxiliary gas flow rate (L/min)	0.5
Argon gas flow rate (L/min)	12
Integration time / s	15 for low and 5 for high emission lines
Analytes	Emission Lines (nm)
Al	I 308.215
Au	I 267.595
Ba	II 493.41
Ca	I 422.673
Co	II 228.616
Cr	II 284.325
Cu	I 327.396
Fe	II 239.562
Mg	II 280.27
Mn	II 260.569
Nd	II 401.225
Ni	II 231.604
Pb	II 220.353
Pd	I 340.458
Pt	II 203.646
Sb	I 217.581
Sn	I 283.999
Ti	II 338.376
Zn	I 213.856

according to Equation 1 and 2:

$$LOD = \frac{3 \times sd_{blank}}{sensitivity} \quad (1)$$

$$LOQ = \frac{10 \times sd_{blank}}{sensitivity} \quad (2)$$

Where sd_{blank} is the standard deviation of blank solutions signals.

2.2 Exploratory analysis

With the concentrations obtained by ICP OES determination, PCB element distribution maps, scores maps and loading plot, besides correlation plots were performed in order to visualize and interpret the data. For the scores and loading, the data were auto-scaled and the images were constructed according to the results from Principal Component Analysis (PCA). For correlation plot, the values were calculated with Pearson correlation. More details about these plots are written in the section "Results and Discussion". All data organization, treatment, calculation, and figures preparation were made in MATLAB 2017b (Matworks, Natick, MA, USA.

3. RESULTS AND DISCUSSION

3.1 Concentration values acquired by ICP OES

A PCB from HDD was studied and, in this case, the goal was to verify the distribution of the elements on the board without milling process. The main advantages are minimum sample preparation and maximum recovery of the elements, since each small fragment is analyzed individually. On the other hand, for some fragments the resulting mineralized solution was not entirely free of solid residues. These samples contain a lot of polymers and silicon.

Table 3 presents the concentration values obtained by ICP OES for Al, Au, Ba, Ca, Co, Cr, Fe, Mg, Mn, Nd, Ni, Pb, Pd, Pt, Sn, Ti and Zn. For Ag, the results were obtained using FAAS. LOD and LOQ are also showed in Table 3. The PCB was split in 77 sub-samples, which were named according to the position of them on the board. For example, row 1 and column 1 is the first sub-sample. There are 11 rows and 7 columns. The concentration values are in a range from the minimum to maximum of each row among the 7 columns. In the case of Ag, concentration obtained in the row 1 (R: 1) and the 7 columns (C: 1 to 7) ranged from 201 to 415 mg kg^{-1} (see Table 3).

The most abundant element on the PCB is Cu with maximum concentration around 30% m m^{-1} in row 11 and column 3 (see Table 3, concentration value of 299482 mg kg^{-1}), followed by Fe (~ 11% m m^{-1}, row 7, column 3), Sn (~ 8% m m^{-1}, row 11, column 3), Ca (~ 7% m m^{-1}, row 8, column 6) and Pb (~ 4% m m^{-1}, row 11, column 2). Among the precious or noble metals, Pd is the most abundant on the PCB with 0.31% m m^{-1} in row 3 and column 2, followed by Au (0.15% m m^{-1}, row 10, column 3), Pt (0.11% m m^{-1}, row 7, column 3) and Ag (0.07% m m^{-1}, row 9, column 6).

Harmful elements, as Cr and Pb, were determined on the PCB with low concentration for Cr (maximum of 43 mg kg^{-1}). On the other hand, high concentrations for Pb were determined (from 0.16 to 4% m m^{-1}), which is present on the solder material. Neodymium, a REE, was also determined with high concentrations for some fragments (0.90% m m^{-1} for row 3 and column 4). Therefore, it can be observed huge variability of different elements that are present on a PCB from HDD.

3.2 Exploratory analysis using different tools

As described in the last section and Table 3, the results obtained for a single PCB are chemically rich, but how these elements are correlated? Is it possible to identify a group of elements that can be recycled together? These questions will be clarified in this section. For better visualization of the data, several images were built. The scores map and loading plot are based on PCA, as mentioned before, that describe the original dataset, simplifying and reducing the number of variables without losing information (Sperança et al., 2017; Carvalho et al., 2015; Santos et al., 2018). The data were organized in a matrix with 77 samples (sub-samples) and 21 variables (elements concentration) and, this dataset was auto-scaled to give the same importance to all variables. The dataset is represented in a new space with principal components (PC's). In this case, 21 variables or dimensions (elements concentration) were reduced to 2 new variables with 20% and 18% of explained variance for PC1 and PC2, respectively. Figure 1 shows the original PCB before the lathe process (split in 77 sub-samples with 11 rows and 7 columns), the scores and loadings for PC1

TABLE 3: Concentration acquired by ICP OES and FAAS (Ag), LOD and LOQ for all elements determined.

Fragments	Range	Ag	Al	Au	Ba	Ca	Co	Cr	Cu	Fe	Mg	Mn	Nd	Ni	Pb	Pd	Pt	Sb	Sn	Ti	Zn
R: 1 C: 1 to 7	Min	201	2875	< LOD	86	6974	<LOD	<LOD	39546	106	126	< LOD	<LOD	227	2448	< LOD	<LOD	<LOD	3358	< LOD	<LOD
	Max	415	29104		8708	65459	29	40	126196	11249	755	5464	4163	5217	8798	1336	143	1047	11910	2816	1753
R: 2 C: 1 to 7	Min	291	8733	< LOD	114	20212	<LOD	17	106846	308	245	< LOD	<LOD	977	4590	17	<LOD	<LOD	6525	102	195
	Max	457	28836	548	18411	64668	27	31	189153	8438	661	485	498	4018	11688	740	73	2750	16588	3088	951
R: 3 C: 1 to 7	Min	236	4883	< LOD	272	11019	<LOD	<LOD	88702	142	145	< LOD	<LOD	853	6796	28	<LOD	<LOD	9378	221	228
	Max	400	29409	111	24962	64790	27	30	160208	13625	693	5249	9046	5324	13158	3146	122	837	15999	2316	1681
R: 4 C: 1 to 7	Min	222	7576	< LOD	103	16517	<LOD	<LOD	108210	208	204	< LOD	<LOD	230	2559	29	<LOD	<LOD	3032	121	228
	Max	437	23482	490	14102	52864	12	22	200032	605	598	18	5547	2274	12568	789		1955	15034	2028	497
R: 5 C: 1 to 7	Min	115	6095	< LOD	<LOD	12931	<LOD	<LOD	88280	192	164	< LOD	<LOD	<LOD	2608	8	<LOD	187	4772	58	121
	Max	357	17339	385	4522	40698	70	32	181054	33442	446	324	12	16368	14619	96	332	3480	18275	1018	368
R: 6 C: 1 to 7	Min	90	2186	< LOD	<LOD	<LOD	<LOD	<LOD	85272	93	< LOD	< LOD	<LOD	<LOD	1571	< LOD	<LOD	<LOD	3193	< LOD	94
	Max	360	17945	308	6906	40461	1801	25	131434	25632	481	5535	5248	13606	13062	284	230	3540	16801	1648	465
R: 7 C: 1 to 7	Min	108	2456	< LOD	<LOD	6901	<LOD	<LOD	82691	326	120	< LOD	<LOD	<LOD	4440	< LOD	<LOD	<LOD	6144	< LOD	138
	Max	577	15188	355	8346	34296	2623	24	211269	107030	424	399	566	17008	14692	273	1058	2077	19523	1487	14174
R: 8 C: 1 to 7	Min	122	7837	< LOD	92	18060	<LOD	10	92856	341	229	< LOD	<LOD	<LOD	5212	< LOD	<LOD	<LOD	6735	102	171
	Max	489	31256	747	13138	67034	36	29	278284	6138	662	3408	15	3956	13492	228	48	2314	14383	172	330
R: 9 C: 1 to 7	Min	111	2017	< LOD	<LOD	4027	<LOD	<LOD	84071	445	< LOD	< LOD	<LOD	<LOD	5331	14	<LOD	<LOD	7845	< LOD	213
	Max	652	21807	255	9409	49073		29	213297	842	699	11129	17	3427	22926	427		974	25428	1992	5464
R: 10 C: 1 to 7	Min	135	1979	< LOD	<LOD	3935	<LOD	<LOD	67185	75	139	< LOD	<LOD	<LOD	4243	< LOD	<LOD	<LOD	6170	< LOD	155
	Max	518	31477	1477	174	61094	145	43	219580	26718	760	202		13258	26107	106	275	3280	31426	50	317
R: 11 C: 1 to 7	Min	429	9981	< LOD	110	20421	<LOD	<LOD	76793	287	275	< LOD	<LOD	269	8692	15	<LOD	<LOD	12342	125	128
	Max	548	23444	334	8729	47686		23	299482	571	492	17	16	2183	42288	318			78318	1701	11976
LOD		0.03	0.4	0.08	0.5	0.3	0.07	0.08	0.3	0.5	0.6	0.09	0.06	0.4	0.03	0.08	0.07	0.5	0.07	0.4	0.4
LOQ		0.09	1	0.3	2	0.9	0.2	0.3	1	2	2	0.3	0.2	1	0.1	0.3	0.2	2	0.2	1	1

** For each row (R), from column (C) 1 to 7, is presented the concentration range with minimum (Min) and maximum (Max) values for each element determined. The concentrations are in mg kg^{-1}*

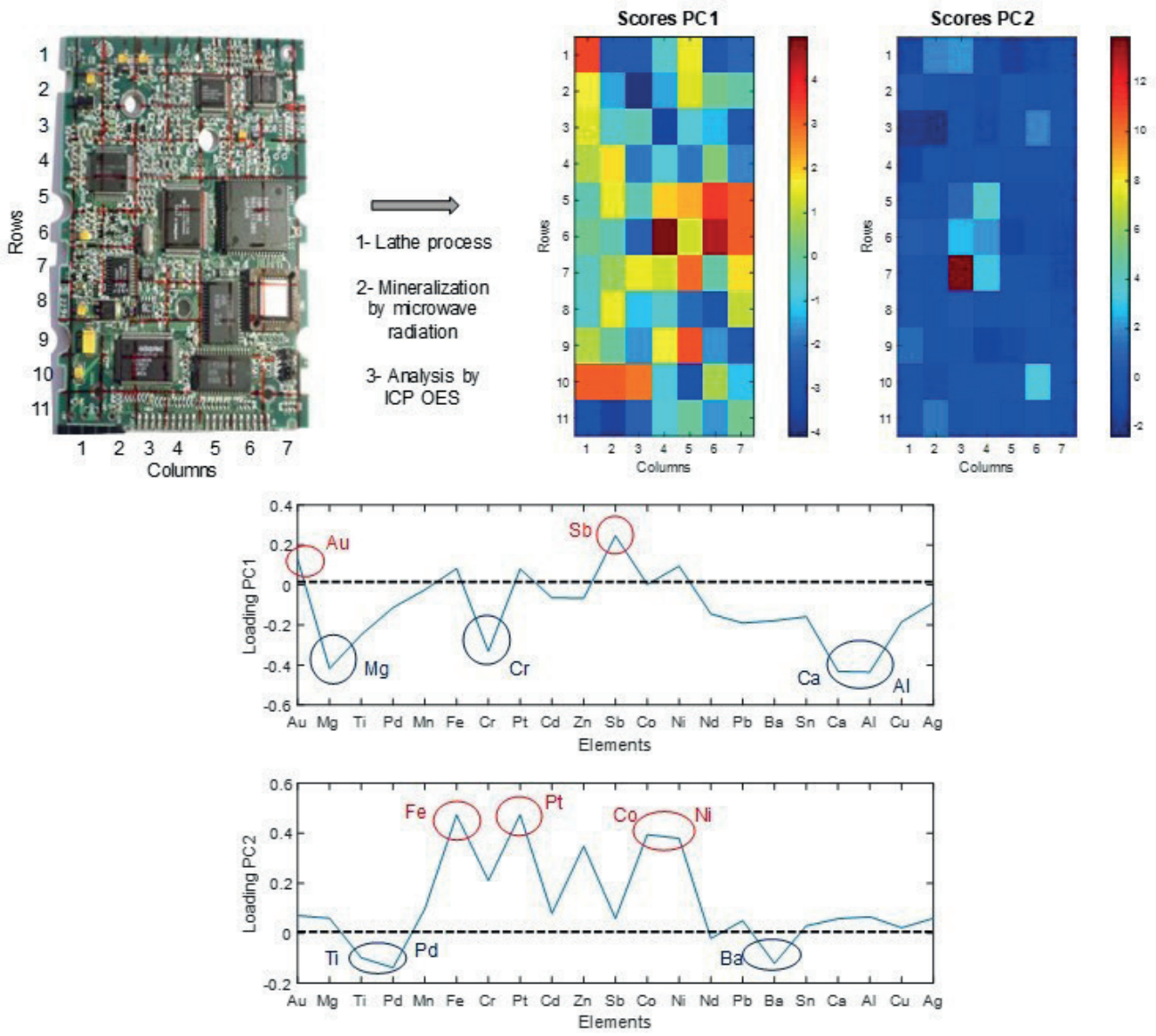

FIGURE 1: Scores map and loading plot of the PCB with decomposition in two principal components (PC1 and PC2).

and PC2. The scores represent the sub-samples and, the loadings the variables.

In this case, the red and blue colors are correlated with positive and negative loadings, respectively. According to PC1, the red spots (scores PC1) are more correlated with Au and Sb (loading PC1), and the blue spots with Mg, Cr, Ca and Al. For PC2, the red spot (scores PC2) is more correlated with Fe, Pt, Co and Ni (loading PC2), and the blue spots with Ti, Pd and Ba.

Another way to visualize this data is with the correlation plot that is shown in Figure 2. This plot is based on Pearson correlation, that shows how close two variables are to obtaining a linear relationship. The correlation value (R) range from -1 to 1 and this number refers: (1) correlations close to 1, that means a positive correlation where the variables change in the same direction; (2) null correlation (close to 0), none relationship between variables; (3) correlations close to -1, that means negative correlation where the variables change in an opposite way. The red spots have a positive correlation (close to 1), while the blue spots negative correlation (see the color bar for better interpretation).

Ca, Al and Mg, for instance, have a correlation close to 1 (maximum), and these three elements are correlated with Cr in a range of 0.8. Figure 3 shows the individual distribution on the PCB of these four elements using the concentrations acquired from ICP OES. The plots were made using the function “imagesc” from MATLAB. With Figure 3, it is possible to observe that Ca, Al and Mg have the same profile, with high concentration on the same sub-samples (rows 1 and 2 with columns 2 and 3, for example). And low concentration (blue spots) for sub-samples on the rows 5 and 6 with columns 5, 6 and 7 (also similar for Cr). The correlation of these three elements with Cr is not so high because just in some fragments the profile of Cr is similar with Ca, Al and Mg (row 1 with columns 2 and 3, for example). Ca, Al and Mg are present in the glass fiber used on the PCB. This material is composed of SiO_2 with the highest concentration, followed by CaO_2 and Al_2O_3. MgO is also

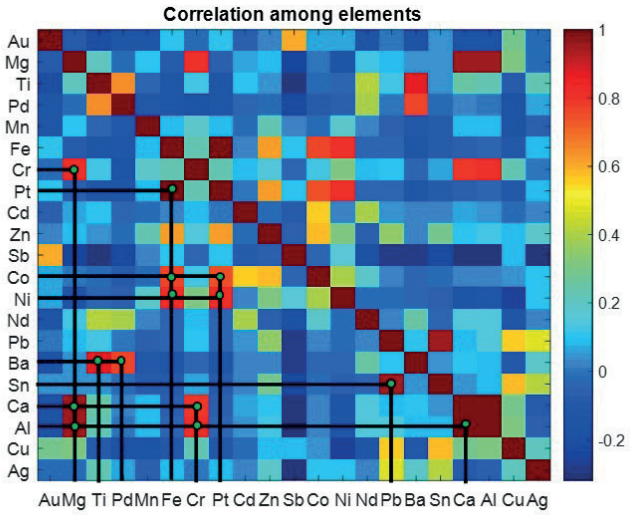

FIGURE 2: Correlation plot for all elements determined by ICP OES.

in the composition but with a lower concentration than Ca and Al (Sanapala, 2008), and this can be also observed in Figure 3 (see the color bar with the concentration values).

Other elements that have correlation close to 1 are Sn and Pb (Figure 2), which are on the solder material used to assemble the components on the PCB. The lead-based solders are banned in European Union, but in some regions are still used due to physic-chemical properties, high degree of "wetting" and the cost of Pb. Sn-Ag-Cu (Sanapala, 2008) and Ga-Sb-Zn (Dervisevic et al., 2013) alloys can be used as free-lead solder material, being the Sn-Ag-Cu alloy more used than Ga-Sb-Zn alloy. Figure 4 shows the individual distribution of Pb and Sn on the PCB and can be observed the same behavior for both elements, mainly concentrated on the row 11. Sn concentration is much higher than Pb concentration, which can be also found in anticorrosive coatings of other metals.

According to PC2 loading plot (Figure 1), Ba, Ti and Pd are correlated and observing Figure 2, this correlation is around 0.8. On the other hand, it is more about Ba/Ti and Ba/Pd. The relationship between Ba and Ti may be due to the barium titanate present on the ceramic material as dielectric in capacitors. Figure 5 shows the individual distribution of Ba, Ti and Pd. It can be observed the similar profile between Ba and Ti. But, for Ba and Pd, it can be considered an indirect correlation, where on row 3 and columns 1, 2 and 4, there are high concentration of Ba and Pd. The platinum group elements are used as coatings in switches and sensors.

Elements as Pt, Fe, Co and Ni appear correlated in PC2 loading plot (Figure 1) with Zn being also in the same plot quadrant. The correlation plot (Figure 2) contain Pt with Fe in a correlation close to 1, Co/Ni with Fe and Co/Ni with Pt in a correlation close to 0.8, but for Zn the correlation decrease around 0.6. Figure 6 shows the individual distribution for these elements. They have a similar behavior, mainly on the row 7 and columns 3 and 4. These elements can be found in some components on PCB, Fe in magnetic components and Ni in conductive films in resistors, for example.

A last correlation in the PC1 loading plot (Figure 1) is for Au and Sb with a value around 0.6 (Figure 2, correlation plot). Figure 7 shows the individual distribution on the PCB. The profile is a little bit similar with high concentration on row 10 and column 3, for example. Gold is used as coating of connection pins of micro-chips and in integrated circuits. Antimony can be used in soldering, Cu plating or connect to it on the connecting pins, as a semiconductor dopant, in addition, as additive of flame retardant polymeric composites.

There are other elements in Figure 2, but with low correlations with each other. For example, Cu is the most abundant element on the PCB and, in Figure 2 appears with low correlation with other elements. Cu is used on printed circuit tracks and in the connecting pins, in addition, it is also used in some electronic components.

4. CONCLUSIONS

The possibility of sample preparation without gridding

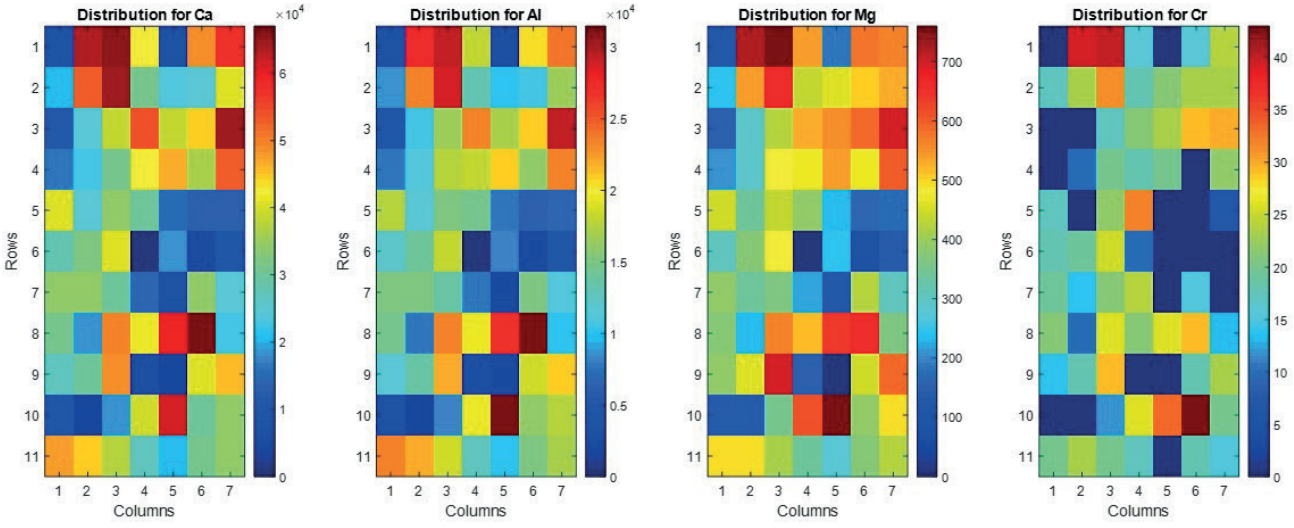

FIGURE 3: Distribution of Ca, Al, Mg and Cr on the PCB with individual concentration acquired by ICP OES.

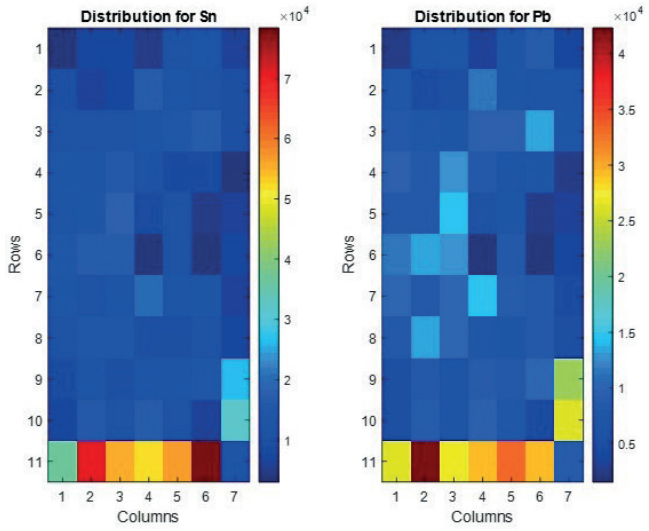

FIGURE 4: Distribution of Sn and Pb on the PCB with individual concentration acquired by ICP OES.

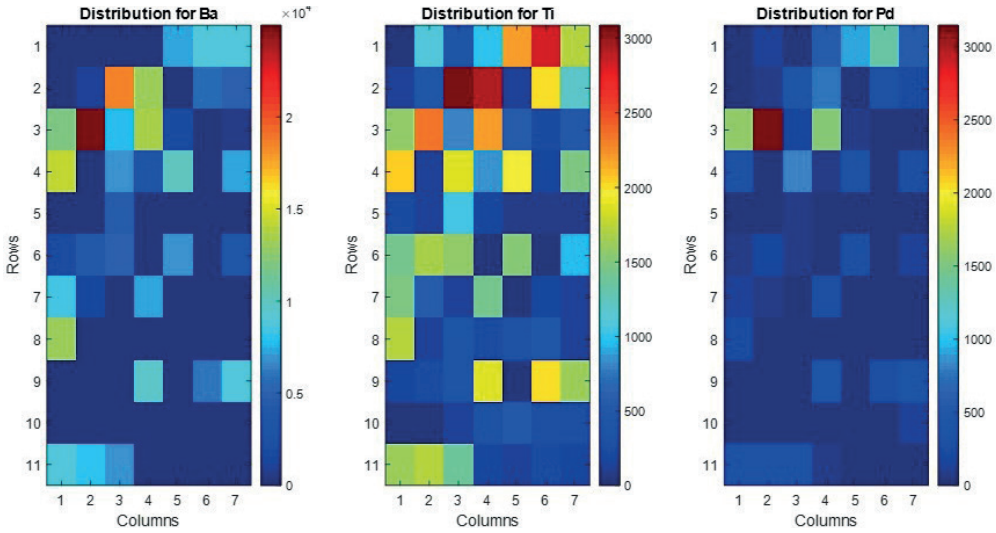

FIGURE 5: Distribution of Ba, Ti and Pd on the PCB with individual concentration acquired by ICP OES.

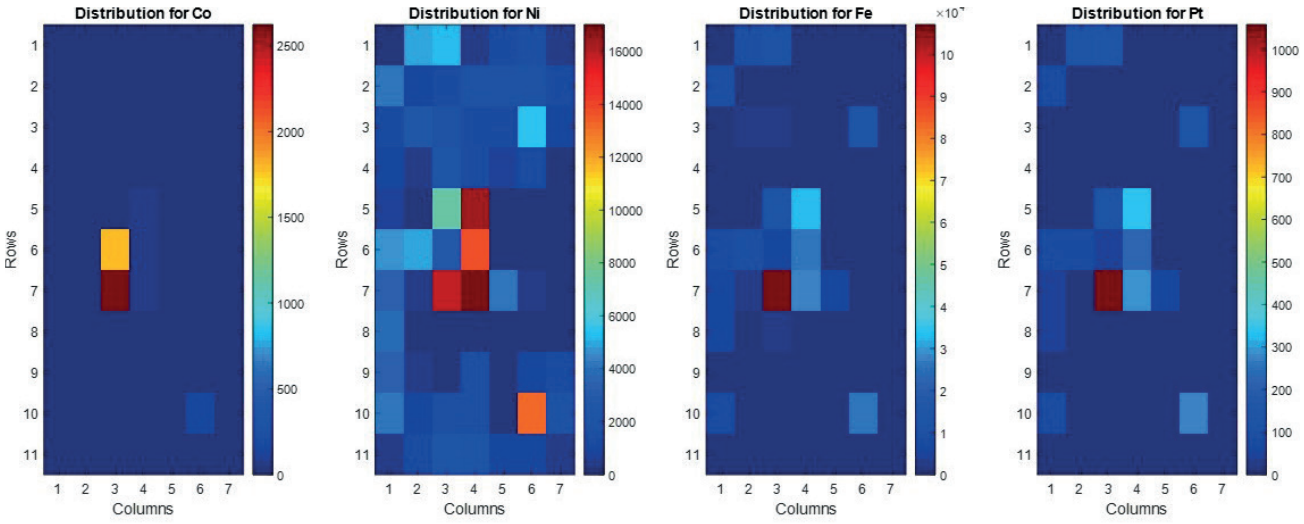

FIGURE 6: Distribution of Co, Ni, Fe and Pt on the PCB with individual concentration acquired by ICP OES.

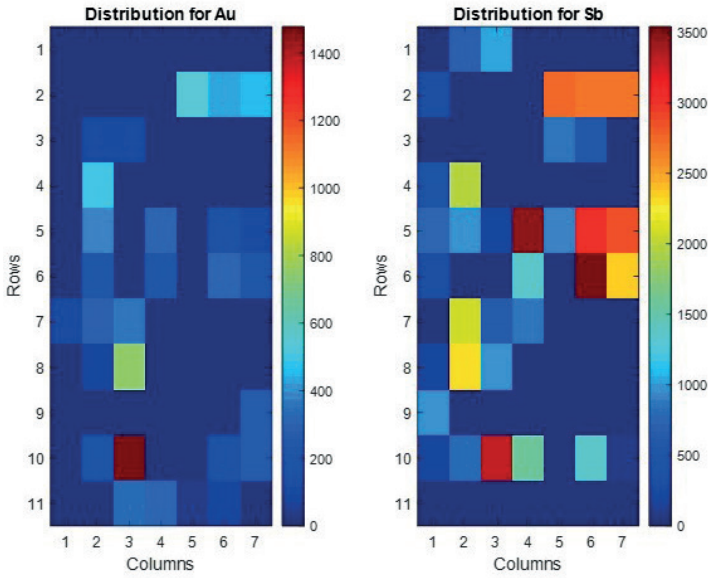

FIGURE 7: Distribution of Au and Sb on the PCB with individual concentration acquired by ICP OE.

process may avoid material loss, improving the detectability, and figures of merit of the proposed method. In addition, the use of several images contributed to better interpretation of ICP OES results. Each figure complements the other, while scores map and loading plot show the main correlation among elements, correlation plot presents how closely correlated these elements are and, individual distribution shows how is this correlation around the PCB components. Therefore, it is a promising way to visualize and interpret the data, contributing to urban mining and recycling.

ACKNOWLEDGMENTS

This study was supported by the São Paulo Research Foundation (FAPESP, grants 2012/01769-3, 2012/50827-6, 2014/22408-4, 2016/01513-0, 2016/17221-8 and 2018/17753-5) and Conselho Nacional de Desenvolvimento Científico e Tecnológico (CNPq, 401074/2014-5, 305637/2015-0 and 141311/2017-7). This study was financed in part by the Coordenação de Aperfeiçoamento de Pessoal de Nível Superior - Brasil (CAPES) - Finance Code 001.

REFERENCES

Andrade, D. F., Romanelli, J. P., & Pereira-Filho, E. R. (2019a). Past and emerging topics related to electronic waste management: top countries, trends, and perspectives. Environmental Science and Pollution Research, 26, 17135-17151. https://doi.org/10.1007/s11356-019-05089-y.

Andrade, D. F., Machado, R. C., Bacchi, M. A., & Pereira-Filho, E. R. (2019b). Proposition of electronic waste as a reference material - Part 1: sample preparation, characterization and chemometric evaluation. Journal of Analytical Atomic Spectrometry, 34, 2394-2401. DOI: 10.1039/C9JA00283A.

Andrade, D. F., Machado, R. C., & Pereira-Filho, E. R. (2019c). Proposition of electronic waste as a reference material – part 2: homogeneity, stability, characterization, and uncertainties. Journal of Analytical Atomic Spectrometry, 34, 2402-2410. DOI: 10.1039/c9ja00284g.

Baldé, C. P., Forti, V., Gray, V., Kuehr, R., & Stegmann, P. (2017). The Global E-waste Monitor 2017. United Nations University (UNU), International Telecommunication Union (ITU) & International Solid Waste Association (ISWA), Bonn/Geneva/Vienna.

Bookhagen, B., Obermaier, W., Opper, C., Koeberl, C., Hofmann, T., Prohaska, T., & Irrgeher, J. (2018). Development of a versatile analytical protocol for the comprehensive determination of the elemental composition of smartphone compartments on the example of printed circuit boards. Analytical Methods, 10, 3864-3871. DOI: 10.1039/c8ay01192c.

Carvalho, R. R. V., Coelho, J. A. O., Santos, J. M., Aquino, F. W. B., Carneiro, R. L., & Pereira-Filho, E. R. (2015). Laser-induced breakdown spectroscopy (LIBS) combined with hyperspectral imaging for the evaluation of printed circuit board composition. Talanta, 134, 278-283. https://doi.org/10.1016/j.talanta.2014.11.019.

Castro, J. P., & Pereira-Filho, E. R. (2018). Spectroanalytical method for evaluating the technological elements composition of magnets from computer hard disks. Talanta, 189, 205-210. https://doi.org/10.1016/j.talanta.2018.06.062.

Cayumil, R., Ikram-Ul-Haq, M., Khanna, R., Saini, R., Mukherjee, P. S., Mishra, B. K., & Sahajwalla, V. (2018). High temperature investigations on optimising the recovery of copper from waste printed circuit boards. Waste Management, 73, 556-565. http://dx.doi.org/10.1016/j.wasman.2017.01.001

Costa, V. C., Castro, J. P., Andrade, D. F., Babos, D. V., Garcia, J. A., Sperança, M. A., Catelani, T. A., & Pereira-Filho, E. R. (2018). Laser-induced breakdown spectroscopy (LIBS) applications in the chemical analysis of waste electrical and electronic equipment (WEEE). Trends in Analytical Chemistry, 108, 65-73. https://doi.org/10.1016/j.trac.2018.08.003.

Cucchiella, F., D'Adamo, I., Koh, S. C. L., & Rosa, P. (2015). Recycling of WEEEs: An economic assessment of present and future e-waste streams. Renewable and Sustainable Energy Reviews, 51, 263-272. http://dx.doi.org/10.1016/j.rser.2015.06.010.

Cui, J., & Zhang, L. (2008). Metallurgical recovery of metals from electronic waste: A review. Journal of Hazardous Materials, 158, 228-256. Doi: 10.1016/j.jhazmat.2008.02.001.

Dervisevic, I., Minic, D., Kamberovic, Z., Cosovic, V., & Ristic, M. (2013). Characterization of PCBs from computers and mobile phones, and the proposal of newly developed materials for substitution of gold, lead and arsenic. Environmental Science and Pollution Research, 20, 4278-4292. DOI 10.1007/s11356-012-1448-1.

El-Nasr, R. S., Abdelbasir, S. M., Kamel, A. H., & Hassan, S. S. M. (2020). Environmentally friendly synthesis of copper nanoparticles from waste printed circuit boards. Separation and Purification Technology, 230, 115860. https://doi.org/10.1016/j.seppur.2019.115860.

Huang, K., Guo, J., & Xu, Z. (2009). Recycling of waste printed circuit boards: A review of current technologies and treatment status in China. Journal of Hazardous Materials, 164, 399-498. Doi: 10.1016/j.jhazmat.2008.08.051.

Mesquita, R. A., Silva, R. A. F., & Majuste, D. (2018). Chemical mapping and analysis of electronic componentsfrom waste PCB with focus on metal recovery. Process Safety and Environmental Protection, 120, 107-117. https://doi.org/10.1016/j.psep.2018.09.002.

Moosakazemi, F., Ghassa, S., Soltani, F., & Mohammadi, M. R. T. (2020). Regeneration of Sn-Pb solder from waste printed circuit boards: A hydrometallurgical approach to treating waste with waste. Jounal of Hazardous Materials, 385, 121589. https://doi.org/10.1016/j.jhazmat.2019.121589.

Park, Y. J., & Fray, D. J. (2009). Recovery of high purity precious metals from printed circuit boards. Journal of Hazardous Materials, 164, 1152-1158. Doi: 10.1016/j.jhazmat.2008.09.043.

Rao, M. D., Singh, K. K., Morrison, C. A., & Love, J. B. (2020). Challenges and opportunities in the recovery of gold from electronic waste. Royal Society of Chemistry Advances, 10, 4300-4309. DOI: 10.1039/c9ra07607g.

Sanapala, R. (2008). Characterization of FR-4 Printed Circuit Board Laminates Before and After Exposure to Lead-free Soldering Conditions. Thesis submitted to the Faculty of the Graduate School of the University of Maryland.

Santos, M. C., Dai, C., & Pereira, F. M. V. (2018). Chemical element profiles in commercial woven fabric combining laser-induced breakdown spectroscopy and chemometrics. Journal of Applied Spectroscopy, 85, 543-551. DOI 10.1007/s10812-018-0685-6.

Silvas, F. P. C., Correa, M. M. J., Caldas, M. P. K., De Moraes, V. T., Espinosa, D. C. R., & Tenório, J. A. S. (2015). Printed circuit board recycling: Physical processing and copper extraction by selective leaching. Waste Management, 46, 503-510. http://dx.doi.org/10.1016/j.wasman.2015.08.030.

Sperança, M. A., Aquino, F. W. B., Fernandes, M. A., Lopez-Castillo, A., Carneiro, R. L., & Pereira-Filho, E. R. (2017). Application of Laser-induced breakdown spectroscopy and hyperspectral images for direct evaluation of chemical elemental profiles of coprolites. Geostandards and Geoanalytical Research, 41, 273-282. https://doi.org/10.1111/ggr.12155.

Tanvar, H., Barnwal, A., & Dhawan, N. (2020). Characterization and evaluation of discarded hard disc drives for recovery of copper and rare earth values. Journal of Cleaner Production, 249, 119377. https://doi.org/10.1016/j.jclepro.2019.119377.

Yamane, L. H., De Moraes, V. T., Espinosa, D. C. R., & Tenório, J. A. S. (2011). Recycling of WEEE: Characterization of spent printed circuit boards from mobile phones and computers. Waste Management, 31, 2553-2558. Doi: 10.1016/j.wasman.2011.07.006.

Zhang, S., Ding, Y., Liu, B., Chang, C-C. (2017). Supply and demand of some critical metals and present status of their recycling in WEEE, Waste Management, 65, 113-127. http://dx.doi.org/10.1016/j.wasman.2017.04.003.

Chapter 3. Alternative calibration methods for direct solid analysis techniques

3. Alternative calibration methods for direct solid analysis techniques

In this chapter, two studies approaching the analysis of high-performance magnet are shown employing two techniques: LIBS and WD XRF. In both studies, some calibration strategies were proposed to overcome the problems with matrix effect due to direct analysis of solids. A brief description about this topic are presented in the next pages.

3.1. Direct analysis of solids

There are several steps to achieve a final result in a chemical analysis, such as, material collect; pretreatment (washing, drying, milling, sifting, polishing); sampling; weighing; sample treatment (digestion, dissolution, lixiviation, fusion); separation (interferents – analyte) and preconcentration in some cases; calibration and, final result. Due to several steps, the possibility of contamination is huge, so, the elimination of some steps is advantageous. Besides eliminate contamination possibility, direct analysis of solids is much faster than traditional analysis [41–44].

With direct analysis of solids is necessary the collect of material, pretreatment (normally, milling), sampling and weighing to perform pellets, for example, which means, several advantages: higher analytical frequency, lower reagent consumption (sample treatment is excused), lower residue generation, lower risk of contamination, lower risk of analyte losses, higher detectability (there is no dilution) and microanalytic characteristic [41–44].

On the other hand, quantitative analysis presents challenges. Due to the possibility of generating chemical information through small masses, the sample's representativeness needs to be adequate with reduced sample particle size to obtain a homogeneity and minimize matrix effect, obtaining an efficient atomization with a good precision [41–44].

3.2. Calibration methods

In the literature is common to find many studies using the traditional approaches for univariate models, such as, external calibration (EC), matrix-matching (MMC), internal standardization (IS) and standard addition (SA) [45]. For direct analysis of solids, the MMC is the most used due to its characteristics to minimize the matrix effect, where it is possible using a set of samples with reference values or certified reference material (CRM) or solid standards with the

interference as standards being similar with sample matrix. On the other hand, as disadvantages, it is necessary a huge dataset if use samples as standards, few CRMs are available with appropriate mass in a microanalytic analysis and the necessity to know the matrix with all interferents to make a solid standard [45].

Therefore, the search for alternative models is increasing and new proposals are emerging. Multi-energy calibration (MEC) is a recent strategy proposed by Virgilio et al. [46]. It is a simple matrix-matching procedure that uses two solid standards of calibration (two pellets): (1) a portion of sample and standard; and (2) a portion of sample and blank. The proportions sample:standard and sample:blank need to be constant to overcome the strong matrix effects. The blank is a diluent that can be a salt or binder, for example. And the standard used can be a CRM or sample with reference values of the interest analytes. Normally, calibration curve is built fixing the energy (E, wavelength), varying the concentration (C) and adopting I (instrumental response) as dependent variable. But, in this case, the C is fixed and the E is varied (analytical signals obtained in several wavelength). Therefore, the calibration is performed by analysis of each pellet, where multiple analytical signals from the same element are acquired in several wavelengths. Relationships can be considered and are showed in Eq. 1 and 2:

$$I_{\lambda i}^{(sam+std)} = m(C^{sam} + C^{std}) \quad \text{Eq. 1}$$

$$I_{\lambda i}^{(sam)} = m(C^{sam}) \quad \text{Eq. 2}$$

Where the $I_{\lambda i}^{(sam+std)}$ and $I_{\lambda i}^{(sam)}$ are the instrumental responses for the pellet with sample + standard and, for the pellet with sample + blank, respectively, m is the proportionality constant, C^{sam} is the analyte concentration in the sample and C^{std} is the analyte concentration in the standard. With the same matrix (sample amount constant in both pellets) and same experimental conditions, the Eq. 1 and 2 may be combined as showed in Eq. 3 and, rearranged in Eq. 4:

$$\frac{I_{\lambda i}^{(sam)}}{C^{sam}} = \frac{I_{\lambda i}^{(sam+std)}}{C^{sam}+C^{std}} \quad \text{Eq. 3}$$

$$I_{\lambda i}^{(sam)} = I_{\lambda i}^{(sam+std)} \times \left[\frac{C^{sam}}{C^{sam}+C^{std}}\right] \quad \text{Eq. 4}$$

The linear curve is built plotting $I_{\lambda i}^{(sam)}$ on the y-axis vs. $I_{\lambda i}^{(sam+std)}$ on the x-axis with several instrument responses in different wavelengths, so, the slope will be (Eq. 5):

$$Slope = \left[\frac{C^{sam}}{C^{sam+C^{std}}}\right] \quad \text{Eq. 5}$$

As C^{std} is known, the analyte concentration in the sample is found by Eq. 6:

$$C^{sam} = \frac{Slope \times C^{std}}{(1-Slope)} \quad \text{Eq. 6}$$

Virgilio et al. proposed this strategy for microwave-induced plasma optical emission spectrometry (MIP OES), ICP OES and high-resolution continuum source flame atomic absorption spectrometry (HR-CS FAAS) in different matrices [46]. For LIBS, the first approach using MEC was made by Babos et al. [47], where the authors determined Ca, Cu, Fe, Mn and Zn in solid samples of cattle mineral supplements with satisfactory results. There are also applications for brick clay and sediment [48], liquid crystal displays (LCD) [49], dietary supplements [50], and nickeliferous ores [51].

One-point gravimetric standard addition (OP GSA) is another alternative strategy proposed by Babos et al. [52], in which is based on SA calibration with only one standard addition, increasing the analytical frequency and decreasing the amount of sample used. Two standards are used like MEC: one with sample + standard and, the other one with sample + blank. In addition, masses are considered, instead of volumes being more appropriate for direct analysis of solids. The calibration curve is built with two points, where x_{axis} and y_{axis} are showed in Eq.7 and 8, respectively:

$$x_{axis} = \frac{m_s C_s + m_D C_D}{m_x} \quad \text{Eq. 7}$$

$$y_{axis} = \frac{m_x + m_s}{m_x} S \quad \text{Eq. 8}$$

Where the m_s is the standard mass, C_s is the standard concentration (known), m_D is the diluent mass, C_D is the concentration of the analyte in the diluent, m_x is the sample mass, S is the analytical signal. The concentration of the analyte in the diluent is 0, so the term $m_D C_D$ is neglected in Eq. 7. In x_{axis} has

the standard concentration added, being 0 for the pellet with sample + blank. In y_{axis} is the analytical signal referring to one wavelength multiplied by the masses of pellet with sample + standard or sample + blank. The concentration of the interest analyte in the sample (C_x) is calculated by extrapolation of calibration curve (Eq. 9):

$$C_x = \frac{Intercept}{Slope} \quad \text{Eq. 9}$$

In addition, for being a model with two points, it is necessary calculate the F-test to confirm the significance of the models.

The characteristics of MEC and OP GSA are similar because both present the same sample preparation being a crucial factor to obtain a good final result due to the homogeneity of the mixtures [45]. With MEC is possible to observe spectral interferences and remove them from the model. In addition, both models present an excellent matrix-matching procedure using only two standards for each sample. On the other hand, the selection of appropriate blank and standard can be a challenge [45].

The two-point calibration transfer (TP CT) was a strategy proposed in this thesis, where the general idea is based on the amount of sample influenced by the plasma. This strategy is derived by the Slope ratio calibration (SRC) [53] with one difference: the TP CT uses only two points to build the linear model instead of several points as shown in Nunes et al. [53]. With well-established experimental conditions, the emission intensity (I) is directly proportional to the ablated mass of the analyte (m) showed in Eq. 10, being also proportional to the number of pulses (Np) collected as Eq. 11. Therefore, the I is proportional to the Np, as Eq.12:

$$I = k_1 m \quad \text{Eq.10}$$

$$m = k_2 Np \quad \text{Eq.11}$$

$$I = KNp \quad K = k_1 k_2 k_n \quad \text{Eq.12}$$

The linear model is built plotting the intensity related to emission line of the interest analyte in y_{axis} as a function of the number of laser pulses in x_{axis}. It is made two linear models: for an unknown sample and, a sample considered standard. This standard sample can be a CRM or a sample with reference values.

Using the C_{std} (analyte concentration in the standard) and, both slopes of the two linear models, the C_{sample} is obtained with Eq. 13:

$$C_{sample} = \frac{Slope_{sample}}{Slope_{standard}} \times C_{std} \quad \text{Eq.13}$$

As mentioned before, the model is built with two points that refer to two sets of laser pulses. It is important that the second set is bigger than the first and, the intensity in y_{axis} is related to the sum of the both sets of laser pulses. As the model has two points, the F-test is calculated to verify the significance, as mentioned for OP GSA.

As advantages, the sample preparation and data treatment are simple. But, to choose a standard is a difficult task. In order to obtain a good accuracy, the concentrations of the interest analyte in the unknown and the standard samples must be similar [45]. This strategy was also applied for cocoa beans [54], waste PCB [55] and recycled polypropylene from car batteries [56].

There is also the multivariate analysis that is the study of several variables measured in a number of samples, appointed by first-order calibration. Some advantages over univariate approach are noted: multiple responses improve the precision and reduce noise; if all variation source (interferent and analyte) is present in calibration model and both signals are different, this model will be able to handle the interferents; and many parameters are calculated where it is possible to understand, investigate and improve the model [57]. Multiple Linear Regression (MLR), Principal Component Regression (PCR), Partial Least Square (PLS) and Artificial Neural Networks (ANN) are the most common multivariate approaches. In this chapter, MLR and PLS were studied.

MLR assumes that the concentration is an absorbance function (Eq. 14) and the regression coefficient can be calculated by Eq. 15:

$$\hat{\boldsymbol{y}} = \boldsymbol{X}\boldsymbol{b} + \boldsymbol{e} \quad \text{Eq.14}$$

$$\boldsymbol{b} = (\boldsymbol{X}'\boldsymbol{X})^{-1}\boldsymbol{X}'\boldsymbol{y} \quad \text{Eq.15}$$

Where $\hat{\boldsymbol{y}}$ is the vector containing the predicted concentration, $\boldsymbol{X}$ is the data matrix, **b** is the vector with the coefficients of the model, $\boldsymbol{e}$ is the vector with residue and **y** is the vector with the real concentration. All the calculations are evaluated by Anova Table. In this model, it is necessary more samples than variables and, the variables need to have low correlation each other [58,59].

Some studies are found in the literature with LIBS and MLR for Ti quantification in sunscreen [60], Pb quantification in tea leaves [61] and total carbon concentration in soil [62].

In PLS approach, a subspace is generated by latent variables (LV), which are linear combinations of original data, with information from data of matrix **X** (Eq. 16) and property of interest **y** (Eq. 17) [58,59,63]. The main goal is the correlation between **X** and **y** maximizing the covariance between the scores **T** and **U**, as Eq. 18:

$$\boldsymbol{X} = \boldsymbol{T}\boldsymbol{P}' + \boldsymbol{E} \quad \text{Eq. 16}$$

$$\boldsymbol{y} = \boldsymbol{U}\boldsymbol{Q}' + \boldsymbol{e} \quad \text{Eq. 17}$$

$$\boldsymbol{U} = \boldsymbol{R}\boldsymbol{T} \quad \text{Eq.18}$$

Where **T** and **U** are the scores for **X** and **y**, respectively, **P** and **Q** are the loadings for **X** and **y**, respectively. Some algorithms are used for calculations, such as, Nonlinear Iterative Partial Least Squares (NIPALS):

- Calculate weights (**W**) from **U** random;
- Scores of **X** (**T**) from **W**;
- Loadings of **y** (**Q**) considering **T**;
- Scores of **y** (**U**) with **Q**;
- Loadings of **X** (**P**) considering **T**.

The regression coefficient (**b**) and the prediction values ($\hat{\boldsymbol{y}}$) are calculated by Eq. 19 and 20, respectively:

$$\boldsymbol{b} = \boldsymbol{W}(\boldsymbol{P}'\boldsymbol{W})^{-1}\boldsymbol{Q} \quad \text{Eq. 19}$$

$$\hat{\boldsymbol{y}} = \boldsymbol{X}\boldsymbol{b} \quad \text{Eq. 20}$$

It is important a special care with overfitting and underfitting, which means, information in excess (high factors number, error and explained variance) and, important information was not considered (low factors number and high prediction error), respectively [58,59,63].

A sure rule is to validate the model. There are two options: cross-validation (CV) and prediction of new samples. The best option is to obtain a large dataset with the possibility of sharing it in two sets (calibration and validation) and, also calculate the CV, mainly to choose the adequate number of factors [58,59,63].

Among the methods of multivariate calibration, PLS is the most employed with many applications in different fields for LIBS [64–66] and WD XRF [67–69].

3.3. Laser-induced breakdown spectroscopy (LIBS)

LIBS is a technique based on emission spectroscopy, where a short pulse of high energy is generated by a laser and focused on sample surface through lens and mirrors. When this high energy reaches the sample, a plasma (~10,000 K) is formed with its characteristics (fusion/vaporization of a small amount of sample). Plasma material will be dissociated into several atomic and ionic species and, with the cooling of the plasma the ions and atoms emit optical radiation, in which is collected by optical fiber and taken to spectrometer to be diffracted and, detected. After all, the spectra are processed in the computer [70–72]. The LIBS scheme is shown in the Figure 2.

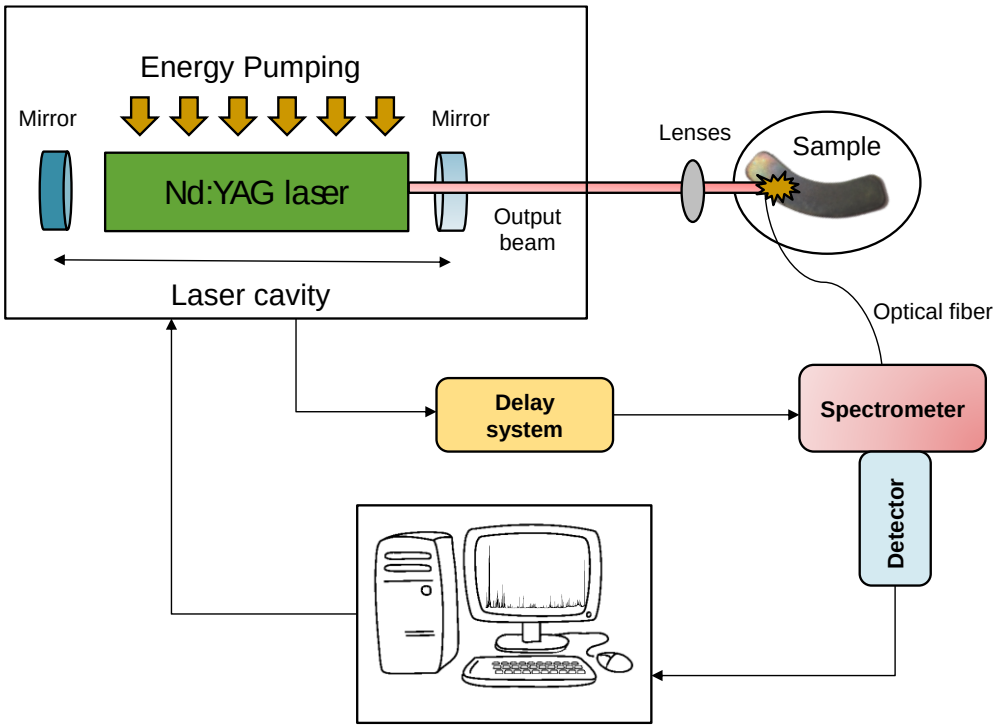

Figure 2. LIBS instrumentation.

The advantages of this technique are countless: (i) versatile sampling; (ii) none or few sample preparation (minimizing interference); (iii) ablation with small amount of sample; (iv) material analysis with difficult mineralization; (v) long distance analysis (portable LIBS); (vi) analysis of the sample micro-region; (vii) multi elementary analysis; (viii) simple and fast analysis (high analytical frequency). But limitations are also present: spectral and matrix interferences; low availability of calibration standard in µg range; problems with heterogeneity (high heterogeneity: low precision and high relative standard deviation - RSD), low sensitivity and repeatability [70–72].

Some parameters may be optimized to obtain reliable results in LIBS [73]. Laser pulse energy and spot size (size of ablated area) are observed together in the laser pulse fluency term (laser pulse energy per unit area, J cm^{-2}) [70]. And delay time, that is the necessary time between plasma creation and data acquisition to isolate the region where there is a maximum of signal-to-background ratio [70]. In addition, the signal can suffer fluctuations due to sample-laser interaction, being minimized with spectra normalization [74,75].

In order to compare with ICP OES, the main differences in LIBS instrumentation are the plasma that is formed in situ in the sample surface by laser beam (there is no sample transport), different types and shapes of samples can be analyzed and temporal resolution to avoid continuum emission.

Over the years the interest in analysis by LIBS is increasing with many applications in different areas: agriculture [76], environmental [77], food [78], pharmaceutical [79], biological [80], forensic [81], metallurgical [82], e-waste [3]. In a Web of Science search, 5,005 papers were found from 1991 to 2021 using the topic “Laser-induced breakdown spectroscopy and LIBS”.

3.4. Wavelength Dispersive X-ray Fluorescence (WD XRF)

The XRF analysis is a qualitative and quantitative method based on intensity measurements (number of X-rays detected per time) of the characteristic X-rays emitted by the sample elements [83].

The primary X-ray photons can be produced in an X-ray tube where a large number of electrons from the cathode are accelerated to bombard the anode with high kinetic energy being converted into X-ray photons to reach the sample surface. These X-ray photons reach an electron of the innermost layer of the atom, which is removed leaving a vacancy. This vacancy is filled by an electron of a higher energy level that emits an X-ray fluorescent photon characteristic of the electronic transition of the elements present in the sample. With an appropriate crystal considering the characteristics of the analyte, the radiation is dispersed at different wavelengths according to Bragg’s law. Collimators are used before the radiation dispersion to ensure an effectively parallel beam and after, where the different diffracted wavelengths are sent to the detector (flow proportional counter – FPC or scintillation counter - SC). The signal is amplified and transformed into a digital counting (intensity in count per second – cps versus

2Θ degrees) being processed to obtain analytical data [83]. The WD XRF scheme is shown in Figure 3.

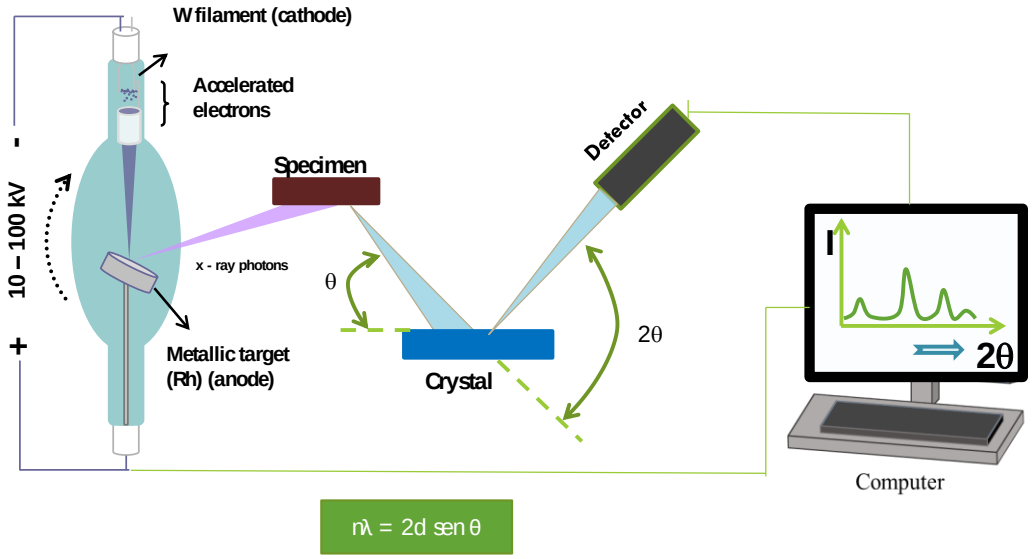

Figure 3. WD XRF instrumentation.

The most common characteristics of this technique are non-destructive analysis, robustness, sequential determination of several elements, qualitative and quantitative analysis and minimum sample preparation. On the other hand, some disadvantages are present such as: matrix effect, high limits of detection and higher interference mainly for light elements and, light elements as H, C, N, O are not detected [83–85].

Different applications are found in the literature: qualitative approach for chemical speciation [67] and spectral image [86], besides quantitate analysis (determinations in a range from ppm to %) for several types of samples [87–90].

3.5. Calibration strategies for the direct determination of rare earth elements in hard disk magnets using laser-induced breakdown spectroscopy

Talanta 208 (2020) 120443

Contents lists available at ScienceDirect

Talanta

journal homepage: www.elsevier.com/locate/talanta

Calibration strategies for the direct determination of rare earth elements in hard disk magnets using laser-induced breakdown spectroscopy

Jeyne Pricylla Castro, Diego Victor Babos, Edenir Rodrigues Pereira-Filho*

Group of Applied Instrumental Analysis, Chemistry Department, Federal University of São Carlos, São Carlos, São Paulo State, P. O. Box 676, 13565-905, Brazil

ARTICLE INFO

Keywords:
E-waste
Multi-energy calibration
One-point gravimetric standard addition
Two-point calibration transfer
Matrix effects
Multivariate calibration

ABSTRACT

This study is dedicated to the direct determination of base (B and Fe) and some rare earth elements (REE; Dy, Gd, Nd, Pr, Sm and Tb) in hard disk magnets. Five calibration strategies were tested and compared. Two of them are related to multivariate calibration: multiple linear regression (MLR) and partial least squares (PLS). Both presented adequate trueness values within a range of 80–120% for almost all analytes. The only exception was Tb, which was probably due to matrix effects. The use of MLR and PLS permits the testing of calibration models in the presence of interference, but matrix effects are not corrected. Because of this, three other univariate calibration methods were also tested and compared: multi-energy calibration (MEC), one-point gravimetric standard addition (OP GSA) and two-point calibration transfer (TP CT). These three calibration approaches permit matrix effects corrections, but an appropriate selection of the blank and standard is mandatory. The standard error obtained ranged from 0.01 to 6% using these univariate calibration methods.

1. Introduction

The amount of electrical and electronic equipment (EEE) is growing rapidly due to several anthropogenic factors such as disposable income, urbanization and industrialization. These technological devices bring new economic opportunities to several industries and countries. In many countries, individuals own more than one electronic device, which is replaced frequently in time periods shorter than one year. A consequence of this high consumption cycle is a continuous and alarming increase in electronic waste (e-waste) generation. In 2016, for instance, the worldwide generation of e-waste was approximately 45 million metric tons. For 2021, the generation of e-waste is projected to be approximately 50 million metric tons [1].

Thus, the recycling of e-waste is very important to avoid contamination of the air, water and soil, where potentially toxic elements and organic molecules can put human and animal health at risk [2–4]. In addition, the recovery of precious and strategic metals, such as rare earth elements (REEs), in e-waste is a growing demand and a reality due to the reduction in their natural reserves [5].

According to Chemical & Engineering News from the American Chemical Society (ACS) [6], scientists from the U.S. Department of Energy are spearheading research to develop different processes for the monitoring of REEs in coal waste. A particular process is the use of laser-induced breakdown spectroscopy (LIBS) systems. The researchers are trying to optimize the method to detect lower concentrations of REEs and, also to development a field-portable LIBS instrument. Another source of information is an European project named “Next generation urban mining – automated disassembly, separation and recovery of valuable materials from electronic equipment” (ADIR) [7], which explores and demonstrates innovative technologies for the automated disassembly and separation of mobile phones and electronic printed circuit boards (PCBs) from computers for the recovery of valuable materials. In this European project, the LIBS technique is used to measure the chemical composition of e-waste. Some tests were performed, and recovery rates of > 90% for tantalum, tungsten and neodymium were achieved. The authors mentioned that one of the features of LIBS is the possibility to measure samples of a distance from few centimeters to up to hundreds of meters with high analytical frequency, in addition to the other characteristics and possibilities. In 2018, Costa et al. [8] published a review presenting several applications of LIBS for e-waste, focusing on direct chemical characterization of polymers and PCBs.

In addition to LIBS, other analytical techniques are used to characterize these materials. Inductively coupled plasma optical emission spectrometry (ICP OES) or inductively coupled plasma-mass spectrometry (ICP-MS) are employed in many laboratories, but this analysis involves acid digestion to transform a solid material into a homogeneous aqueous solution. This step of the analytical sequence is clearly

* Corresponding author
E-mail address: erpf@ufscar.br (E.R. Pereira-Filho).

https://doi.org/10.1016/j.talanta.2019.120443
Received 8 July 2019; Received in revised form 1 October 2019; Accepted 3 October 2019
Available online 08 October 2019
0039-9140/

laborious and requires a longer time to accomplish [9,10].

Therefore, the search for analytical instrumental techniques able to perform direct analysis is growing. LIBS is one example, based on atomic emission spectrometry, which uses a laser as the excitation source. Some advantages such as its high analytical frequency, real-time and on-site analysis, non-destructiveness, minimum sample preparation and multi-element capability, enable LIBS technology to be widely used in several applications [11–13].

In the majority of cases, when solid or powder samples are analyzed, it is faster and easier to obtain a spectrum rather than directly determine the property of interest. Therefore, calibration models relate the concentration of an analyte to the intensity of its emission line [14]. However, when the sample is analyzed without preparation, analyte and matrix are simultaneously analyzed, and matrix effects can compromise the atomic emission phenomena, jeopardizing some of the figures of merit such as the accuracy and precision. In this way, calibration strategies should be evaluated and developed to efficiently minimize these drawbacks when using LIBS for the quantitative analysis of solid samples.

There are reports in the scientific literature of several univariate calibration strategies for LIBS, such as matrix-matching calibration [15], standard addition [16], internal standardization [17], and calibration-free [18]. However, new calibration procedures for LIBS, such as multi-energy calibration (MEC) [19–22], one-point gravimetric standard addition (OP GSA) [23] and calibration based on number of pulses named slope ratio calibration [24] have recently been reported in the scientific literature. These strategies present satisfactory results for quantitative determination by LIBS because they employ an efficient matrix-matching method for the samples and standards, which minimizes the matrix effects related to the direct analysis of solids.

In the case of multivariate calibration strategies, partial least squares (PLS) [25,26] and multiple linear regression (MLR) have been successfully applied in LIBS [12,15,27–29]. One of the main advantages of these methods is the possibility of developing a calibration model in the presence of interferents.

Thus, the goal of this study is to propose and evaluate reliable calibration strategies for LIBS, such as PLS, MLR, MEC, OP GSA and a promising calibration strategy named two-point calibration transfer (TP CT), for the determination of six REEs (Dy, Gd, Nd, Pr, Sm and Tb) and two base elements (B and Fe) in high-performance magnets from hard disks (HDs). This material is composed of a Nd-Fe-B alloy including a high amount of REEs. REEs can be recycled and returned to the electronics industry to obtain new EEEs. One previous study is documented in the literature using LIBS with magnets, which covered only the spectral and qualitative analyses of these materials [30].

2. Materials and methods

2.1. Sample preparation and reference values

HDs are devices where data are stored. It is highly complex with several parts as polymers, metals, printed circuit boards (PCBs) and two magnets: the actuator and the spindle motor magnets. In this study, only the actuator magnets were used, and several samples (~56 HDs) were obtained from 8 different manufacturers. These samples were acquired, and the magnets were combined in groups (8 different groups named M1-M8) according to their manufacturers.

The first step of the sample preparation involved heating the magnets in a furnace at 500 °C (approximately 2 h) to eliminate the magnetic field. After that, the sample groups were ground in a knife mill (IKA, A11), and the particle size was estimated to be lower than 500 µm.

To obtain analytes reference values, an analytical method using diluted nitric acid and digestion by a digester block, followed by determination with ICP OES was used. This method was already published by Castro and Pereira-Filho [31], which presents more detailed information about the samples.

2.2. LIBS setup

A LIBS system model J200 (Applied Spectra, Fremont, CA) equipped with a 1064-nm Nd:YAG laser and a spectrometer 6-channel charge-coupled device (CCD) with 12,288 pixels ranging from 186 to 1042 nm was used in this study. The operational conditions that can be modified in the instrument are the delay time (0–2 µs), laser pulse energy (0–100 mJ), spot size (50–250 µm), and laser repetition rate (1–10 Hz). The gate width is fixed at 1.05 ms. The irradiance and laser fluence ranges varies from 0.255 GW cm^{-2} and 2 J cm^{-2} (250 µm spot size and 1 mJ laser pulse energy) to 636.62 GW cm^{-2} and 5093 mJ cm^{-2} (50 µm spot size and 100 mJ laser pulse energy), respectively.

In this study, the instrumental conditions used were 1924 mJ cm^{-2} for the laser fluence (85 mJ laser pulse energy and 75 µm spot size), a 0.5 µs delay time and a 5 Hz laser repetition rate. The analyses were performed in raster mode.

2.3. Calibration strategies

2.3.1. Multivariate calibration

The sample preparation for LIBS was simple and consisted of mixing 1 g of milled sample with 0.2 g of microcrystalline cellulose (as a binder). This mixture was homogenized with a mortar and pestle and pressed (60 kN for 2 min) to form pellets (approximately 12 mm diameter). The whole procedure was performed in triplicate.

For each pellet, approximately 330 spectra were acquired to obtain a representative analysis, and 12 normalization modes [32] were applied to the raw data and codified as:

- Norm 1 and Norm 5: average and sum of the spectra, respectively
- Norm 2 and Norm 6: each individual spectrum is divided by its Euclidean norm. After this, the average (2) or sum (6) is calculated.
- Norm 3 and Norm 7: each individual spectrum is divided by its area (sum of all signal intensity). After this, the average (3) or sum (7) is calculated.
- Norm 4 and Norm 8: each individual spectrum is divided by its maximum intensity value. After this, the average (4) or sum (8) is calculated.
- Norm 9 and Norm 10: each individual spectrum is divided by the intensity of the C I 193.09 nm emission line (normalization by internal standard). After this, the average (9) or sum (10) is calculated.
- Norm 11 and Norm 12: each individual spectrum is divided by the intensity of the C I 247.85 nm emission line. After this, the average (11) or sum (12) is calculated.

After calculate the normalizations, several emission lines were selected for B and Fe (base elements) and Dy, Gd, Nd, Pr, Sm and Tb (REEs). These lines were chosen according to the Aurora software (Applied Spectra) in combination with information from the National Institute of Standards and Technology (NIST) [33]. The emission lines selected for each analyte are shown in Table 1, and the area and height of each signal were calculated and, the average of the replicates was recorded.

After this process, two multivariate calibration models were evaluated for each element: PLS and MLR.. These data sets were autoscaled, and leave-one-out (loo) cross validation was applied. The best results were observed through the standard error of cross validation (SECV) and trueness after comparison to reference values obtained with acid digestion and ICP OES determination. Low SECV values and trueness values of approximately 100% are expected for the results.

For MLR, an analysis of variance (ANOVA) table was calculated for each model, and some emission lines were removed due to insignificant regression coefficients. The confidence level used was 95% in all cases. For some analytes, the number of variables (emission lines) was equal to or higher than the number of samples (8), preventing the use of MLR.

Table 1
All of the emission lines selected and evaluated in the calibration strategies for the elements B, Dy, Fe, Gd, Nd, Pr, Sm and Tb.

Emission lines (nm)	B*	Dy	Fe*	Gd	Nd	Pr	Sm	Tb
λ1	206.66	353.17	234.34	279.69	410.94	410.07	359.26	334.94
λ2	208.89	364.54	239.56	303.28	415.60	414.31	443.43	336.22
λ3	249.67	389.85	259.94	308.19	430.35	511.07	466.94	337.88
λ4	345.13	404.59	263.13	310.05	482.54	517.39	484.17	350.91
λ5	–	421.17	273.95	333.13	485.90	525.97	–	354.02
λ6	–	–	275.57	335.86	490.18	–	–	356.85
λ7	–	–	522.84	336.22	524.95	–	–	–
λ8	–	–	527.03	–	–	–	–	–

*B and Fe are base elements, while the others are REE.

Therefore, several combinations of variables were tested for these cases, using loo cross validation to select the best emission line combination. Fe, with 8 emission lines, is a good example, and 28 MLR models were calculated by combining the emission lines in groups of 6: ($\frac{8!}{6!\times 2!} = 28$ *combinations*). After defining the regression model, another loo cross validation was performed, but this time it was for samples in order to calculate SECV.

All calculations were performed using Microsoft Excel®, MATLAB® 2018a (Matworks, Natick, MA, USA) and Pirouette version 4.5 (Informetrix, Bothell, WA, USA).

2.3.2. Univariate calibration strategies

Three univariate strategies were tested and compared: MEC, OP GSA and a calibration procedure named two-point calibration transfer (TP CT). These univariate calibrations utilize a matrix-matching procedure. The MEC and OP GSA methods require only two calibration standards for each sample. The sample preparation procedure is similar for both, but the data treatment is different. Two standards (pellets) are used: the first one (P1) with sample plus blank and the second (P2) with sample plus standard. P1 was composed of 0.30 g of blank (Na_2CO_3), 0.25 g of sample and 0.05 g of binder (microcrystalline cellulose). P2 was composed of 0.30 g of standard, 0.25 g of sample and 0.05 g of binder. Both mixtures were homogenized with a mortar and pestle and pressed (60 kN for 2 min) to form pellets (approximately 12 mm diameter). These pellets were also prepared in triplicate.

The concentrations of analytes in the samples are very high, so a sample named #M8 containing 0.65% w w^{-1} B, 1.53% w w^{-1} Dy, 64% w w^{-1} Fe, 0.09% w w^{-1} Gd, 24.51% w w^{-1} Nd, 3.9% w w^{-1} Pr, 0.34% w w^{-1} Sm, and 0.18% w w^{-1} Tb was used as a standard to prepare P2 for both MEC and OP GSA calibrations. The LIBS spectra were recorded as mentioned in section 2.3.1. Multivariate calibration, followed by the normalization calculations and, emission lines selection (Table 1).

For MEC, a linear model was built with the different emission lines of each analyte (Table 1). The model was calculated for all of the normalizations and for the area and height of the emission lines. The x-axis is the intensity of P2 (sample + standard) and the y-axis is the intensity of P1 (sample + blank). Through the obtained slope of the calculated linear model and the concentration of standard added (known), C_{std}, the concentration of analyte (unknown), C_{sample}, is calculated, as shown in Eq. (1) [19,34].

$$C_{sample} = \frac{Slope \times C_{std}}{1 - Slope} \quad (1)$$

The best results were selected after observing the relative standard deviation (RSD) and trueness after comparison with reference values.

In the case of OP GSA, a calibration curve is calculated with only two points: P1 (sample + blank) and P2 (sample + standard) for each emission line (Table 1) of the analyte, employing the 12 normalization modes, in order to select the best condition. On the x-axis, the concentration of the analyte in the sample is plotted: 0 for P1 (sample + blank) and for P2 the concentration of the added standard (known). On the y-axis, the intensities of the selected emission lines of the analyte for both pellets are plotted. The sample concentration is calculated from the intercept and slope of the calibration curve, as shown in Eq. (2) [23].

$$C_{sample} = \frac{Intercept}{Slope} \quad (2)$$

The best results were identified by the RSD and trueness according to reference values. Additionally, an F-test was performed in order to observe the significance of the calculated models and their linearity. Both F-values, $F_{experimental}$ and $F_{tabulated}$, were calculated and compared. The F-values were obtained after calculations of mean of square of regression and residue (MSR and MSr, respectively). For the model to be considered statistically valid with good linearity, the $F_{experimental}$ had to be higher than $F_{tabulated}$, with this ratio preferably being higher than 10 [35].

The other calibration procedure tested was the TP CT method. In this study, we also used #M8 as the standard due to the lack of certified reference materials with a similar matrix. The sample preparation is the same as in section 2.3.1 *Multivariate calibration*, where the samples (sample + cellulose as binder) were pressed to form pellets.

First, the 330 spectra obtained for each pellet (n = 3) are split into two spectra sets (two points): the first one with 100 spectra (from the first up to the 100th spectra) and the second with the remaining 230 spectra. These spectra sets were separately summed (normalization mode number 5), and the intensity of point 2 is obviously higher than point 1. After this, the area and height of the emission lines (Table 1) of each analyte were selected. Thus, a linear model is calculated with only two points for each emission line evaluated, where the x-axis is the number of spectra (100 or 230) and the y-axis is the intensity of both points. This was done for the interrogated sample and for the sample chosen as the standard. The combination of the slopes from both models and the standard concentration (known) permits the calculation of the sample concentration, as shown in Eq. (3) [24].

$$C_{sample} = C_{std} \times \frac{Slope_{sample}}{Slope_{std}} \quad (3)$$

As the pellets were made in triplicate, the RSD and trueness were calculated according to the reference values obtained from ICP OES determination. In addition, through the F-test, the ratio of $F_{experimental}$:$F_{tabulated}$ was also evaluated, to verify the linearity of the calibration curve calculated from the two points, as described in OP GSA. Fig. 1 shows graphs of the three univariate calibration models for Fe. In Fig. 1a, MEC with 8 emission lines (from λ1 to λ8) is shown, 1b, OP GSA using only the data from λ8 and 1c, TP CT using only the data from λ6. In all cases, M6 and M8 are the interrogated sample and the standard, respectively.

3. Results and discussion

The matrix effects are challenging characteristics that make quantitative analyses difficult using LIBS, compromising the accuracy and precision. In this way, as the analyte and matrix are simultaneously

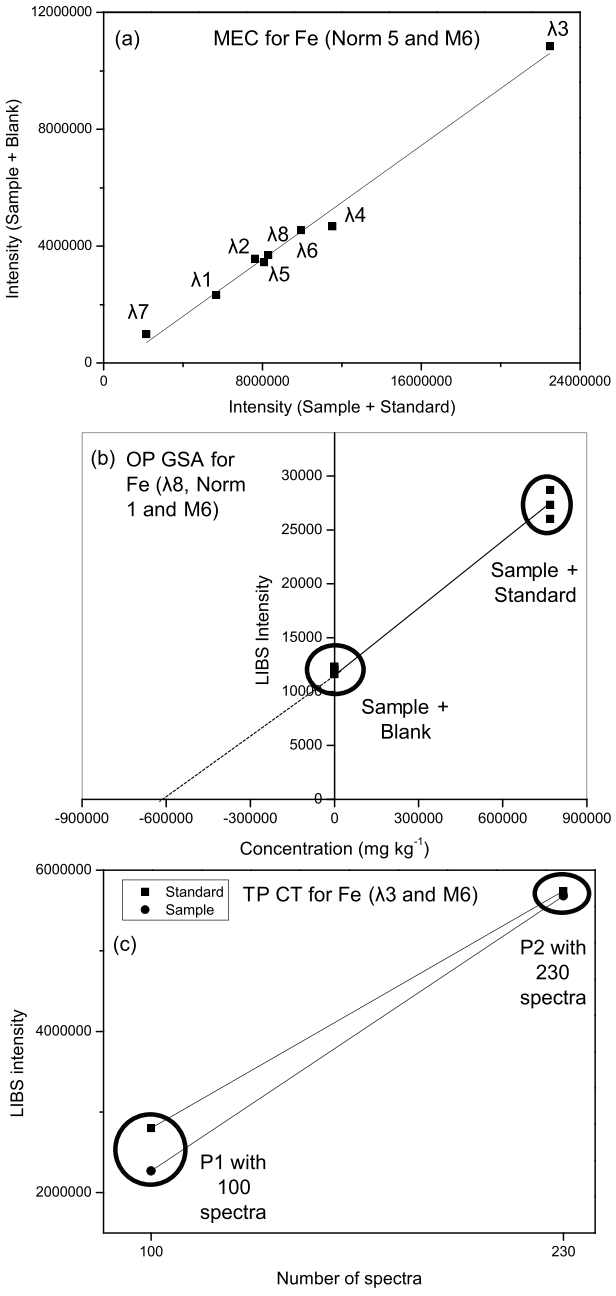

Fig. 1. Graphical description of the three univariate calibration strategies: (a) MEC, (b) OP GSA and (c) TP CT.

ablated by LIBS, the phenomena of the atomic/ionic/molecular emissions of the analyte that occur in the formed plasma may be subject to effects of the sample matrix that are directly analyzed by the LIBS.

In this paper, the main goal is to study and compare several calibration strategies and discuss the advantages and limitations of each one for a sample of e-waste, such as magnets. The emission spectrum obtained by LIBS for the magnets is very complex, presenting thousands of emission lines due to the high amount of Fe in their composition (approximately 60% w w^{-1}). As a consequence, many emission lines appear, which are able to interfere with each other. An additional difficulty is the fact that REE emission lines can mutually interfere.

3.1. Evaluation of multivariate calibrations for LIBS

The MLR and PLS methods present some intriguing features for their use as calibration strategies in LIBS for the analysis of complex samples as magnets. These strategies make it possible to develop calibration models in the presence of interferents.

Table 2 shows some of the parameters used in the proposed models. In addition, Fig. 2 shows the trueness values calculated by comparing the predicted concentrations of all the calibration strategies that were evaluated to the reference concentrations obtained by ICP OES (mentioned in section 2.1. *Sample preparation and reference values*).

For almost all elements and samples, the trueness values were within the range of 80–120%, with the exception of Tb (Fig. 2h), showing that the PLS and MLR calibration models efficiently predicted the concentrations of the majority of the analytes in the magnet samples.

For Tb, the SECV values calculated for the PLS and MLR methods were 0.231 and 0.237% w w^{-1}, respectively, as seen in Table 2. The Tb concentration in the ICP OES analyzed samples was between 0.02 and 0.53% w w^{-1}. Therefore, the calculated SECV values were 12-fold higher than the lowest concentration determined for Tb (#M2). As such, a trueness value above 120% was obtained for the prediction of Tb in the sample that possessed concentration lower than the SECV value. In addition, strong matrix effects were observed for the prediction of the Tb concentration in some samples, with trueness values varying from approximately 26 to 2000% for PLS and from 0 to 500% for MLR (see Fig. 2).

The normalization type was chosen by observing the lowest value of SECV and the best trueness (between 80 and 120%). These models were calculated from the signal area. PLS models were calculated with all of the emission lines shown in Table 1, and the number of latent variables varied from 1 for B, Gd, Nd and Tb to 3 for Pr.

Alternatively, for the MLR models, some of the emission lines were removed due to the fact that their calculated coefficients were not significant, as shown in Table 2. In the case of Fe, for instance, the coefficients relating to λ1, λ4 and λ8 were not significant at a confidence level of 95%.

Table 2
Parameters for the multivariate calibration models.

Element (Concentration range)	Normalization		Latent Variables for PLS	Valid coefficients for MLR[a]	SECV (% w w^{-1})	
	PLS	MLR			PLS	MLR
B (0.63–0.71% w w^{-1})	3	2	1	b0; bλ4	0.033	0.098
Dy (0.72–1.75% w w^{-1})	1	4	2	b0; bλ1; bλ2; bλ3; bλ4	0.101	0.351
Fe (59–64% w w^{-1})	2	12	2	b0; bλ2; bλ3; bλ5; bλ6; bλ7	0.997	3.994
Gd (0.09–0.11% w w^{-1})	1	3	1	bλ4; bλ6; bλ7	0.007	0.039
Nd (24–26% w w^{-1})	11	3	1	b0; bλ1; bλ3; bλ4	0.898	3.237
Pr (2–4% w w^{-1})	9	9	3	All (from λ1 to λ5)	0.067	0.078
Sm (0.31–0.38% w w^{-1})	9	11	2	b0; bλ1; bλ2; bλ3	0.020	0.048
Tb (0.02–0.53% w w^{-1})	4	11	1	b0; bλ1; bλ3; bλ5; bλ6	0.231	0.237

[a] See description in Table 1.

The SECV values varied from 0.007% for Gd (PLS) to 3.994% for Nd (MLR). In general, the PLS and MLR methods were good models with predictive capacity and robustness for all elements; although, the prediction of Tb in some samples, was not possible due to the high values of SECV and strong matrix effects that were observed. Both methods had similar predictive capabilities, but the SECV values were lower for PLS than for MLR.

3.2. Evaluation of univariate calibrations for LIBS

For univariate models, almost all of the elements were in the range from 80 to 120%, with some exceptions, mainly the MEC method (see Fig. 2). For example, for Dy (Fig. 2b), two samples were below 80% for the MEC method, which may be related to the unsuitable proportions of the sample and standard. This parameter was not investigated in this study. On the other hand, for Tb, the trueness values were within the acceptable range. The parameters used in these univariate strategies are shown in Table 3.

The normalizations were chosen according to the best trueness and lowest RSD, as indicated in Table 3. Both peak area and height were used in these models, depending on the sample and element. These normalizations are important to compensate the signal fluctuations (area or height) and sample matrix differences during data acquisition. The RSD values are also presented, which were calculated from the replicate samples (n = 3). For MEC, the RSD varied from 3 to 44%, for OP GSA from 2 to 44% and for TP CT from 2 to 28%, which is considered acceptable for LIBS measurements when direct solid analyses are performed.

3.3. What is the best calibration strategy for LIBS?

This is a very difficult question and depends on the situation; all calibration strategies evaluated have advantages and limitations. Multivariate models are calculated in the presence of interference but do not correct for matrix effects. In addition, the calculations to construct these models are complex, and knowledge about chemometrics is necessary. However, if the samples are similar and do not have appreciable matrix effects, the models are able to predict values with acceptable accuracy.

The univariate models studied in this paper, such as MEC and OP GSA, are efficient alternatives to compensate matrix effects. In the case of MEC, spectral interference (outlier in the linear model calibrations) can also be observed because several emission lines are used, and, if some of them present interference, it is possible to exclude their respective signals and correct the model. This is an advantage when compared with the other methods. However, the sample preparation for MEC and OP GSA is laborious, and the choice of an appropriate blank is difficult in some cases. On the other hand, in several situations, only these methods are able to solve the matrix problems.

For OP GSA, the data treatment is simpler than that of MEC because only one emission line is used. The F-test ratio varied from 2 to 356 among all of the elements and samples, showing the good linearity of the models.

Among the three univariate models tested, TP CT is a new strategy and is very promising for LIBS. The general idea is based on the amount of sample influenced by the plasma. If this amount is greater, the intensity of the analyte in the sample will be greater. The sample preparation and data treatment are simpler in TP CT than in the other methods. A standard (certified reference material or sample that has a reference value) and sample are necessary. If the reference matrix is similar to the sample, the results are excellent. It is necessary only to split the spectra into two sets, sum the spectral information from both sets and select the emission lines of interest. Point 2 must be at least twice as large as point 1 to obtain this difference. Multiple normalizations were not necessary because this strategy uses only the sum of the spectra (normalization number 5), and the F-test ratio varied from 3

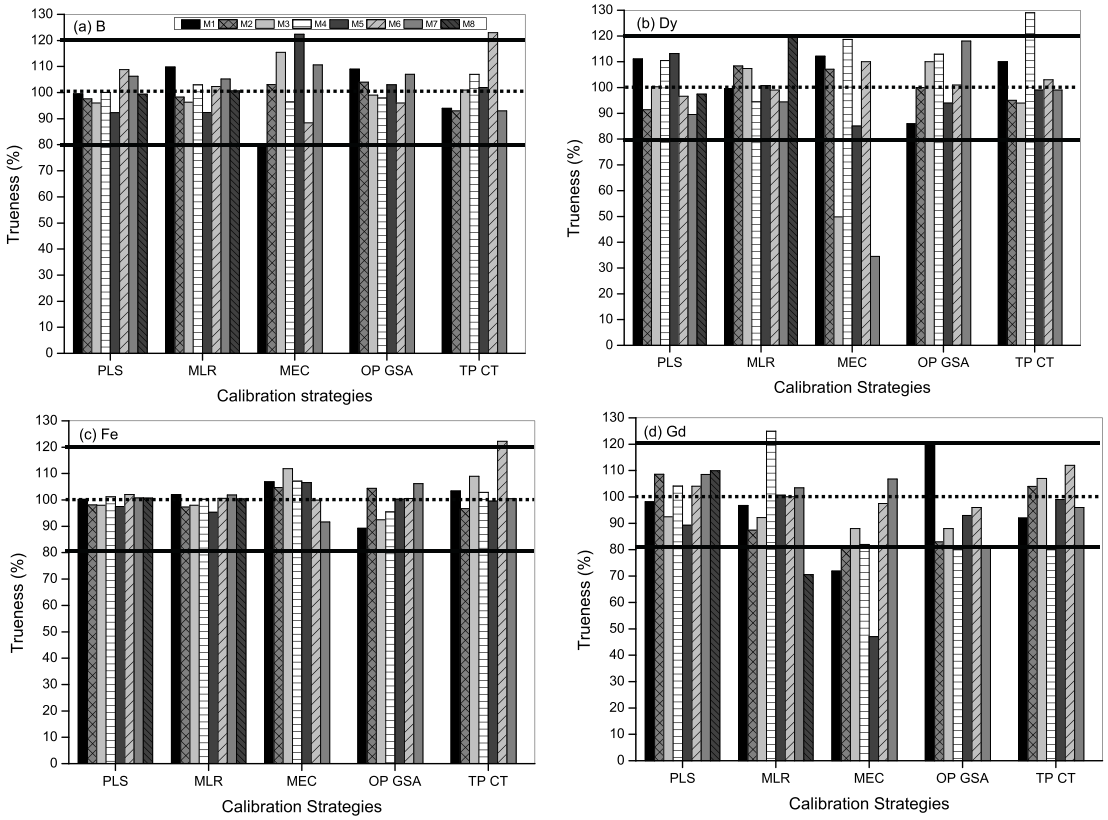

Fig. 2. Trueness (%) value of each element according to reference values for the five calibration strategies: (a) B, (b) Dy, (c) Fe, (d) Gd, (e) Nd, (f) Pr, (g) Sm and (h) Tb.

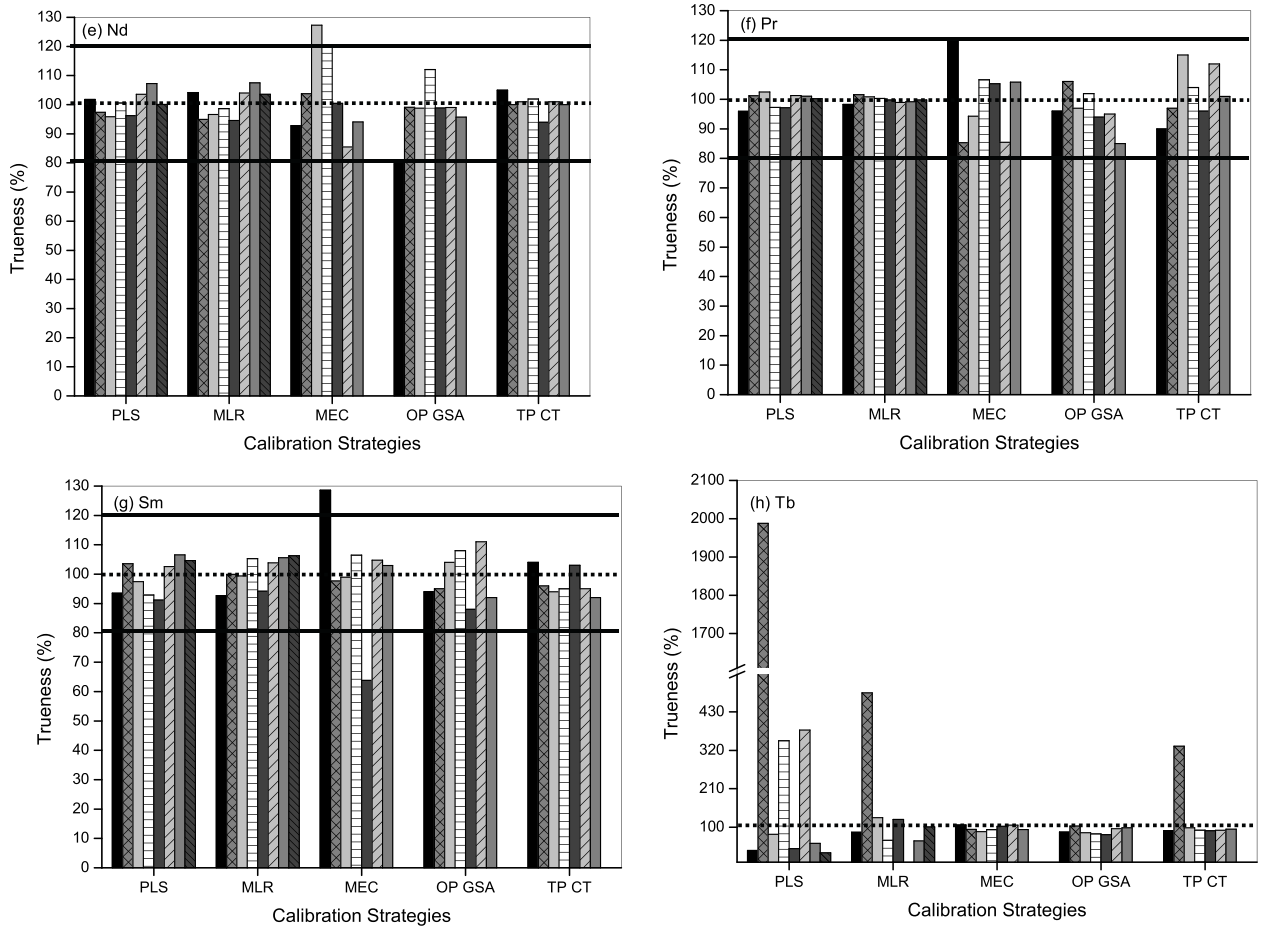

Fig. 2. (*continued*)

to 959, showing good linearity of the models.

An interesting note are the RSD values calculated from determinations employing the TP CT method (2–28%), are low when compared with those from other calibrations (for MEC 3–44% and for OP GSA, 2–44%). However, one limitation is that the physicochemical properties of the standard and the analyzed samples must be similar, to be efficient matrix-matching. In addition, the concentration of the analytes presents in the samples to be analyzed, cannot have great variability, when compared to the concentration of the analytes present in the standard used for the quantification calculations. If there is great variability of the concentration, an under or overestimation of the concentration of the analyte present in the sample may occur, thus compromising the accuracy of the determinations.

Tb is a good example in this case. The Tb concentrations in the samples varied from 0.018% to 0.52% w w^{-1}, being a very wide range. In this case, the PLS and MLR models were not able to correctly predict the concentrations of Tb in the samples due to the difference among them, as can be observed in Fig. 2. On the other hand, MEC and OP GSA

Table 3
Parameters for the univariate calibration models.

Element	MEC			OP GSA			TP CT		
	Normalization	Signal type	RSD (% - Range)	Normalization	Signal type and Emission line	RSD (% - Range)	Signal type	Emission line	RSD (% - Range)
B	9 and 10	Area/ Height	10–43	1, 3 and 9	Area/Height λ.2, λ.3 and λ.4	10–36	Area/ Height	λ.2, λ.3 and λ.4	4–18
Dy	2 and 3	Area/ Height	6–19	3 and 7	Area/Height λ.2 – λ.5	7–21	Area/ Height	λ.1, λ.2, λ.4 and λ.5	2–18
Fe	1, 5 and 9	Area/ Height	4–32	1 and 9	Area λ.1, λ.4, λ.7, λ.8	5–25	Height	λ.2, λ.3 and λ.8	6–24
Gd	1, 3 and 5	Area/ Height	10–36	1, 5 and 9	Area/Height λ.4 – λ.7	11–44	Area/ Height	λ.3 and λ.4	2–20
Nd	1, 3, 9 and 10	Area/ Height	6–43	1, 3, 7, 9 and 10	Area/Height λ.1 – λ.3, λ.5, λ.6	2–24	Area/ Height	λ.2 – λ.6	3–16
Pr	1, 3, 7 and 9	Area	3–41	1, 3, 7 and 9	Area/Height λ.1 – λ.3	4–25	Area/ Height	λ.2, λ.4 and λ.5	5–17
Sm	1 and 3	Area/ Height	6–37	1, 3, 9 and 11	Height λ.1, λ.3, λ.4	5–40	Area/ Height	λ.2 and λ.3	7–28
Tb	1, 3, 4, 7 and 9	Area/ Height	19–44	1, 3 and 4	Area/Height λ.4 – λ.6	10–36	Area/ Height	λ.1, λ.3, λ.4 and λ.5	10–23

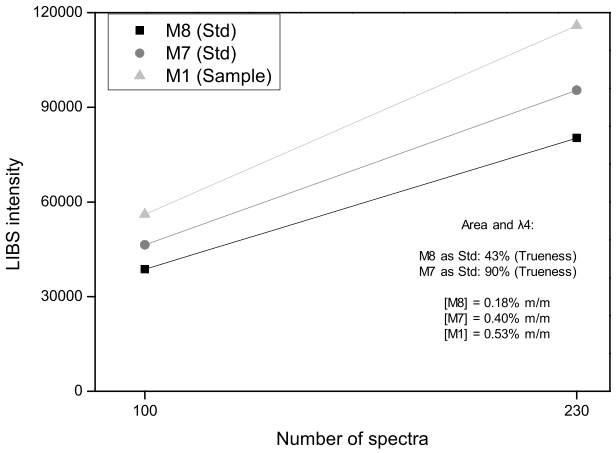

Fig. 3. TP CT method with two different Tb standards in the M1 sample.

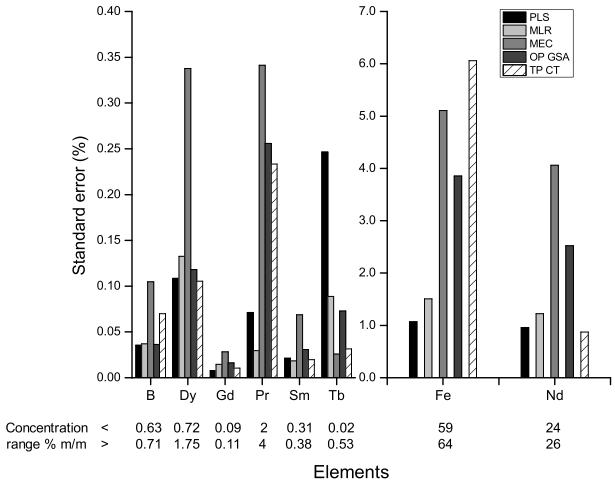

Fig. 5. Standard error (%) values for all elements determined using each calibration model proposed (PLS, MLR, MEC, OP GSA and TP CT), and concentration range for the analytes.

were able to correctly predict the Tb due to the matrix-matching method, which is an advantage in this case. In the TP CT method, the standard used was initially M8 (0.18% w w^{-1} Tb), but for Tb, it was necessary to change the standard according to the concentrations, as can be observed in Fig. 3, which shows an example of an M1 sample (0.53% w w^{-1}) and the use of two different standards (M7 and M8) with their respective trueness.

An example of the three univariate models is shown in Fig. 4. The linear models for MEC with (Fig. 4a) and without (Fig. 4b) spectral interferences, OP GSA (Fig. 4c) and TP CT (Fig. 4d) methods with their respective parameters are shown for Nd. It is possible to observe spectral interference in the MEC model and exclude it, improving the trueness and R^2. Another observation is the best results are seen for TP CT, with a low RSD (7%) and excellent trueness (100%).

A parameter that was calculated for all of the strategies was the standard error (SE) according to Eq. (4):

$$SE = \sqrt{\frac{\sum (y_i - \hat{y}_i)^2}{n-1}} \quad (4)$$

where y_i is the analyte reference concentration, $\hat{y}$ is the concentration predicted by the calibration model, and n is the number of samples.

Fig. 5 shows the SE results for all of the elements in each calibration model. According to these calculations, it is possible to note that the errors were low and that the majority of the elements were similar among the different strategies. All errors are below the concentration of the elements in the samples, with the exception of Tb, which had a sample with a concentration of 0.018% w w−1, and the lowest error for Tb was 0.025% in the MEC model. Even so, the MEC model was able to predict the Tb concentration in this sample with a trueness of 94%.

In this study, raw data were hardly employed for PLS, MLR, MEC

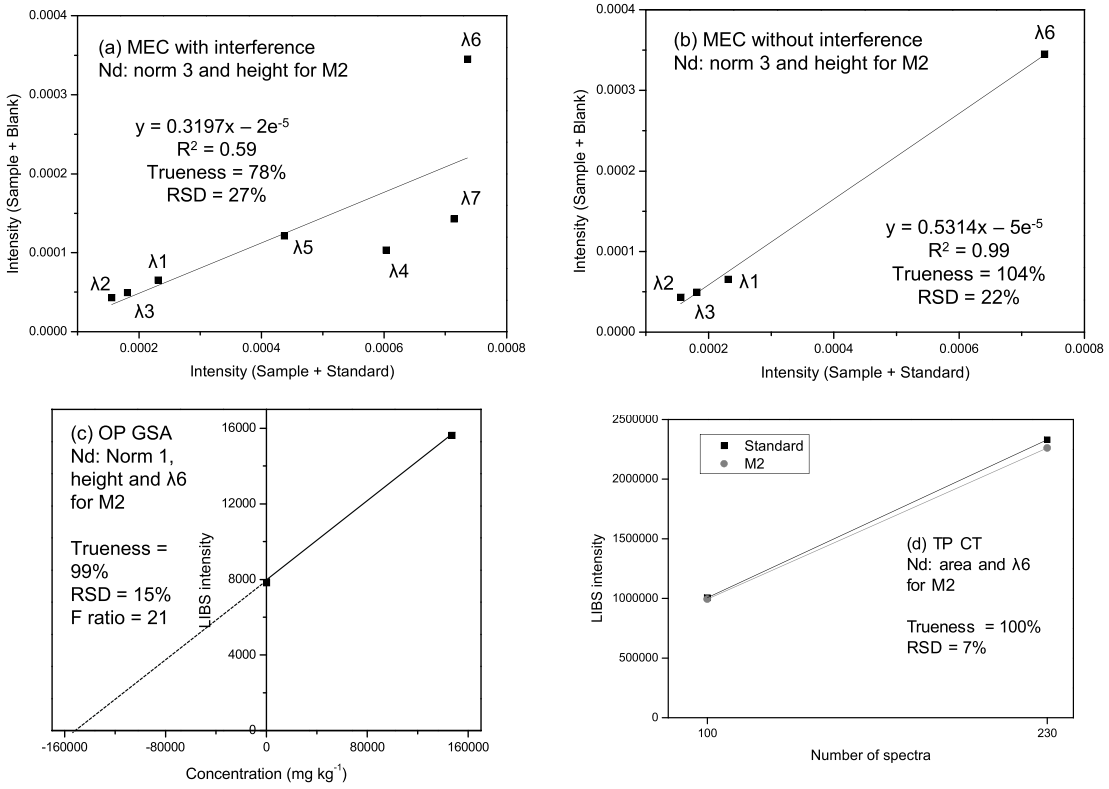

Fig. 4. Three univariate models for Nd: (a) MEC with spectral interference, (b) MEC without spectral interference, (c) OP GSA and (d) TP CT.

and OP GSA. Normalizations are always useful for these data due to the complexity of laser-sample and laser-plasma interactions, in addition to the responsiveness of plasma according to the physical and chemical characteristics of the samples [36]. However, for TP CT, only the normalization number 5 (sum) is necessary.

To compare these calibration approaches for LIBS with an ICP OES analysis for the same material, it is notable that the analysis in LIBS is much faster than ICP OES, besides is not necessary to convert the solid sample into an appropriate aqueous solution for analysis, collaborating with the principle of green chemistry. Even with the problems in solids direct analysis, it is possible to save time and resources with these approaches. However, it is necessary to use reference values, at least, for some samples to ensure the quality of the measurements.

4. Conclusion

Five calibration strategies were proposed and compared for the direct analysis of HD magnets by LIBS, focusing on the determination of base and REEs. The models obtained presented good results with robustness and precision. Each calibration approach has its advantages and limitations and can be chosen according to its necessity and the intrinsic characteristics of the sample and the analyte. In this case, the TP CT stands out over the other calibration strategies evaluated, with sample preparation and data treatment simpler and faster, obtaining excellent figures of merit.

The characteristics of LIBS together with either chemometric (PLS and MLR) or univariate (MEC, OP GSA and TP CT) models make it a powerful analytical technique that can be used in recycling industries to directly characterize e-waste.

Acknowledgments

This study was supported by the São Paulo Research Foundation (FAPESP, grants 2012/01769-3, 2012/50827-6, 2014/22408-4, 2016/01513-0 and 2016/17221-8) and Conselho Nacional de Desenvolvimento Científico e Tecnológico (CNPq, 401074/2014-5, 305637/2015-0 and 141311/2017-7). This study was financed in part by the Coordenação de Aperfeiçoamento de Pessoal de Nível Superior - Brasil (CAPES) - Finance Code 001.

Appendix A. Supplementary data

Supplementary data to this article can be found online at https://doi.org/10.1016/j.talanta.2019.120443.

References

[1] C.P. Balde, V. Forti, V. Gray, R. Kuehr, P. Stegmann, The Global E-Waste Monitor 2017, Quantities, Flows and Resources, United Nations University, Geneva, Bonn, Vienna –, 2017 November.
[2] C. Luo, C. Liu, Y. Wang, X. Liu, F. Li, G. Zhang, X. Li, Heavy metal contamination in soils and vegetables near an e-waste processing site, south China, J. Hazard Mater. 186 (2011) 481–490.
[3] J. Zheng, K-h. Chen, X. Yan, S.-J. Chen, G.-C. Hu, X.-W. Peng, J-g. Yuan, B.-X. Mai, Z.-Y. Yang, Heavy metals in food, house dust, and water from an e-waste recycling area in South China and the potential risk to human health, Ecotoxicol. Environ. Saf. 96 (2013) 205–212.
[4] Y. Yang, M. Xue, Z. Xu, C. Huang, Health risk assessment of heavy metals (Cr, Ni, Cu, Zn, Cd, Pb) in circumjacent soil of a factory for recycling waste electrical and electronic equipment, Mater. Cycles Waste Manag. 15 (2013) 556–563.
[5] S. Zhang, Y. Ding, B. Liu, C.-C. Chang, Supply and demand of some critical metals and present status of their recycling in WEEE, Waste Manag. 65 (2017) 113–127.
[6] B. Erickson, New Source of Rare Earths. U.S. Efforts to Extract Valuable Elements from Coal Waste Surge, Chemical & Engineering News C&EN, Washington, 2018, p. 28 July 9.
[7] R. Noll, C. Fricke-Begemann, S. Connemann, C. Meinhardt, V. Sturm, LIBS analyses for industrial applications – an overview of developments from 2014 to 2018, J. Anal. At. Spectrom. 33 (2018) 945–956.
[8] V.C. Costa, J.P. Castro, D.F. Andrade, D.V. Babos, J.A. Garcia, M.A. Sperança, T.A. Catelani, E.R. Pereira-Filho, Laser-induced breakdown spectroscopy (LIBS) applications in the chemical analysis of waste electrical and electronic equipment (WEEE), Trends Anal. Chem. 108 (2018) 65–73.
[9] M. Ueberschaar, V.S. Rotter, Enabling the recycling of rare earth elements through product design and trend analyses of hard disk drives, J. Mater. Cycles Waste Manag. 17 (2015) 266–281.
[10] D.D. Munchen, H.M. Veit, Neodymium as the main feature of permanent magnets from hard disk drives (HDDs), Waste Manag. 61 (2017) 372–376.
[11] C. Pasquini, J. Cortez, L.M.C. Silva, F.B. Gonzaga, Laser induced breakdown spectroscopy, J. Braz. Chem. Soc. 18 (2007) 463–512.
[12] T. Zhang, H. Tang, H. Li, Chemometrics in laser-induced breakdown spectroscopy, J. Chemom. e2983 (2018) 1–18.
[13] M.A. Aguirre, M. Hidalgo, A. Canals, J.A. Nóbrega, E.R. Pereira-Filho, Analysis of waste electrical and electronic equipment (WEEE) using laser induced breakdown spectroscopy (LIBS) and multivariate analysis, Talanta 117 (2013) 419–424.
[14] M.M.C. Ferreira, Quimiometria. Conceitos, Métodos e Aplicações, first ed., UNICAMP, Campinas, 2015.
[15] A.S. Augusto, P.L. Barsanelli, F.M.V. Pereira, E.R. Pereira-Filho, Calibration strategies for the direct determination of Ca, K, and Mg in commercial samples of powdered milk and solid dietary supplements using laser-induced breakdown spectroscopy (LIBS), Food Res. Int. 94 (2017) 72–78.
[16] R.X. Yi, L.B. Guo, X.H. Zou, J.M. Li, Z.Q. Hao, X.Y. Yang, X.Y. Li, X.Y. Zeng, Y.F. Lu, Background removal in soil analysis using laser- induced breakdown spectroscopy combined with standard addition method, Opt. Express 24 (2016) 2607–2618.
[17] G.G.A. Carvalho, M.B.B. Guerra, A. Adame, C.S. Nomura, P.V. Oliveira, H.W.P. Carvalho, D. Santos Jr., L.C. Nunes, F.J. Krug, Recent advances in LIBS and XRF for the analysis of plants, J. Anal. At. Spectrom. 33 (2018) 919–944.
[18] A. Ciucci, M. Corsi, V. Palleschi, S. Rastelli, A. Salvetti, E. Tognoni, New procedure for quantitative elemental analysis by Laser-induced plasma spectroscopy, Appl. Spectrosc. 53 (1999) 960–964.
[19] D.V. Babos, A. Virgílio, V.C. Costa, G.L. Donati, E.R. Pereira-Filho, Multi-energy calibration (MEC) applied to laser-induced breakdown spectroscopy (LIBS), J. Anal. At. Spectrom. 33 (2018) 1753–1762.
[20] F.M. Fortunato, T.A. Catelani, M.S. Pomares-Alfonso, E.R. Pereira-Filho, Application of Multi-energy calibration for determination of chromium and nickel in nickeliferous ores by laser-induced breakdown spectroscopy, Anal. Sci. 34 (2018) 165–168.
[21] A.S. Augusto, J.P. Castro, M.A. Sperança, E.R. Pereira-Filho, Combination of multi-energy calibration (MEC) and laser-induced breakdown spectroscopy (LIBS) for dietary supplements analysis and determination of Ca, Mg and K, J. Braz. Chem. Soc. 30 (2019) 804–812.
[22] D.F. Andrade, F.M. Fortunato, E.R. Pereira-Filho, Calibration strategies for determination of the in content in discarded liquid crystal displays (LCD) from mobile phones using laser-induced breakdown spectroscopy (LIBS), Anal. Chim. Acta 1061 (2019) 42–49.
[23] D.V. Babos, A.I. Barros, J.A. Nóbrega, E.R. Pereira-Filho, Calibration strategies to overcome matrix effects in laser-induced breakdown spectroscopy: direct calcium and phosphorus determination in solid mineral supplements, Spectrochim. Acta B 155 (2019) 90–98.
[24] L. C. Nunes, F. R. P. Rocha, F. J. Krug, Slope ratio calibration for analysis of plant leaves by laser-induced breakdown spectroscopy), J. Anal. At. Spectrom. Doi: 10.1039/C9JA00270G.
[25] R.G. Brereton, Introduction to multivariate calibration in analytical chemistry, Analyst 125 (2000) 2125–2154.
[26] M.M.C. Ferreira, A.M. Antunes, M.S. Melgo, P.L.O. Volpe, Quimiometria I: calibração multivariada, um tutorial, Quim. Nova 22 (1999) 724–731.
[27] D.A. Cremers, L.J. Radziemski, Handbook of Laser-Induced Breakdown Spectroscopy, second ed., Wiley, United Kingdom, 2013 cap. 7.
[28] M.A. Sperança, D.F. Andrade, J.P. Castro, E.R. Pereira-Filho, Univariate and multivariate calibration strategies in combination with laser-induced breakdown spectroscopy (LIBS) to determine Ti on sunscreen: a different sample preparation procedure, Opt. Laser. Technol. 109 (2019) 648–653.
[29] R. Hernández-García, M.E. Villanueva-Tagle, F. Calderón-Piñar, M.D. Durruthy-Rodríguez, F.W.B. Aquino, E.R. Pereira-Filho, M.S. Pomares-Alfonso, Quantitative analysis of Lead Zirconate Titanate (PZT) ceramics by laser-induced breakdown spectroscopy (LIBS) in combination with multivariate calibration, Microchem. J. 130 (2017) 21–26.
[30] M.Z. Martin, R.V. Fox, A.W. Miziolek, F.C. DeLucia, N. André, Spectral analysis of rare earth elements using laser-induced breakdown spectroscopy, Next-Gener. Spectrosc. Technol. VIII (2015) 9482, https://doi.org/10.1117/12.2178192.
[31] J.P. Castro, E.R. Pereira-Filho, Spectroanalytical method for evaluating the technological elements composition of magnets from computer hard disks, Talanta 189 (2018) 205–210.
[32] J.P. Castro, E.R. Pereira-Filho, Twelve different types of data normalization for the proposition of classification, univariate and multivariate regression models for the direct analyses of alloys by laser-induced breakdown spectroscopy (LIBS), J. Anal. At. Spectrom. 31 (2016) 2005–2014.
[33] NIST electronic database, https://www.nist.gov/pml/atomicspectra-database.
[34] A. Virgilio, D.A. Gonçalves, T. McSweeney, J.A.G. Neto, J.A. Nóbrega, G.L. Donati, Multi-energy calibration applied to atomic spectrometry, Anal. Chim. Acta 982 (2017) 31–36.
[35] R.H. Myers, D.C. Montgomery, C.M. Anderson-Cook, Response Surface Methodology Process and Product Optimization Using Designed Experiments, Wiley, Hoboken, 2009.
[36] E. Tognoni, G. Cristoforett, Signal and noise in laser induced breakdown spectroscopy: an introductory review, Opt. Laser. Technol. 79 (2016) 164–172.

3.6. Neodymium determination in hard drive disks magnets using different calibration approaches for wavelength dispersive X-ray fluorescence

Spectrochimica Acta Part B 164 (2020) 105763

Contents lists available at ScienceDirect

Spectrochimica Acta Part B

journal homepage: www.elsevier.com/locate/sab

Neodymium determination in hard drive disks magnets using different calibration approaches for wavelength dispersive X-ray fluorescence☆

Jeyne Pricylla Castro, Marco Aurelio Sperança, Diego Victor Babos, Daniel Fernandes Andrade, Edenir Rodrigues Pereira-Filho*

Group of Applied Instrumental Analysis, Chemistry Department, Federal University of São Carlos, São Carlos, São Paulo State, P. O. Box 676, Zip Code 13565-905, Brazil

ARTICLE INFO

Keywords:
Matrix-matching
One-point gravimetric standard
Multi-energy calibration
Two-point calibration transfer
E-waste

ABSTRACT

Due to matrix effects and limitations in the calibration process for direct analysis of solids, the search for different calibration approaches is very important. This study is aimed to Nd determination in high-performance magnets from hard disk using direct solid analysis by wavelength dispersive X-ray fluorescence. Three univariate calibration methods were evaluated: multi-energy calibration, one-point gravimetric standard addition and two-point calibration transfer. These strategies employ an efficient matrix-matching method, minimizing the matrix effects related to the direct analysis of solids. The trueness values were calculated according to reference concentration by inductively coupled plasma optical emission spectrometry and the concentration obtained by univariate models. For almost all samples, the trueness values were within an acceptable range from 80 to 120%. Besides that, relative standard deviation values ranged from 3 to 27% for all cases and, the standard error ranged from 2 to 6% w w^{-1} Nd among the calibration methods. These parameters show the potential of these alternative calibration methods over traditional ones.

1. Introduction

In the field of elemental determination, direct solids analysis minimizes the number of preliminary sample preparation operations in the analytical sequence when compared to wet-based traditional approaches. Analysis of solid samples permits several advantages as, minimizes the risks associated with sample handling (*i.e.*, contamination and analyte losses), avoids the use of hazardous reagents and waste generation [1]. However, calibration is still one of the most challenging steps in direct analysis of solid samples. The lack of matrix compatibility between calibration standards and samples may jeopardize the correlation of the analytical signals with the element concentrations. These problems of matrix effects are particularly true for matrix-dependent calibration methods, such as X-ray fluorescence (XRF), laser-induced breakdown spectroscopy (LIBS) and laser ablation (LA) systems coupled with plasma optical emission spectrometry/mass spectrometry [2–4].

External calibration (EC) using univariate methods is a strategy commonly sought due to its simplicity of application, data handling and interpretation. Different strategies have been used as well as matrix-matching calibration (MMC) employing certified reference materials (CRMs) or standards with similar sample matrix composition [5]. For these cases, the low similarity in physical and chemical properties between CRMs/standards and test samples is often the reason of biased results. For instance, the MMC can be combined with internal standardization (IS) [6] to overcome this problem and avoid matrix effects.

Another widespread calibration approach is the standard additions (SA) [7] based upon the preparation of a set of calibration standards by spiking the analytes in gradually crescent concentrations on the sample. The test sample itself is used for calibration, hence the matrix effects can be corrected. However, this method typically requires five calibration standards (*i.e.*, five successive additions), generally consumes large amount of sample, and requires long period of time for analysis, becoming more convenient for small batches. Alternatively, Babos et al. [8] used one-point gravimetric standard addition (OP GSA) as a strategy for Ca and P determination in mineral supplements for cattle using direct solid analysis by LIBS. In addition, OP GSA method requires only two calibration standards: sample + blank (S1) and sample + standard (S2). A calibration curve with two points is calculated with the added analyte concentration on the *x*-axis (0 for S1 and

☆ Selected Paper from the Colloquium Spectroscopicum Internationale XLI & I Latin American Meeting on Laser Induced Breakdown Spectroscopy (CSI XLI - I LAMLIBS) held in Mexico City, Mexico, June 9–14, 2019.

* Corresponding author.
E-mail address: erpf@ufscar.br (E.R. Pereira-Filho).

https://doi.org/10.1016/j.sab.2019.105763
Received 3 October 2019; Received in revised form 10 December 2019; Accepted 28 December 2019
Available online 30 December 2019
0584-8547/

the concentration added of standard for S2). And on the *y*-axis, the intensities of the analyte emission line for both calibration standards. According to intercept and slope, the concentration of the element in the sample can be calculated. Although it has been exploited for LIBS [8] and inductively coupled plasma mass spectrometry (ICP-MS) [9,10] so far, OP GSA can be an alternative for XRF, specially for direct analysis of solid samples, because this strategy requires a small amount of sample and enables simple and rapid data processing.

Others non-traditional and effective approaches for matrix effects correction have been developed, named as multi-energy calibration (MEC) [11] and, more recently, two-point calibration transfer (TP CT) [12]. Similar to OP GSA, MEC applies only two calibration standards, on the other hand, different electronic transition energies (emission lines) are used to obtain a linear model. This linear model is built plotting the intensities from S1 (sample + blank) on the *y*-axis and the intensities from S2 (sample + standard) on the *x*-axis. With the slope of the linear model and the analyte concentration added to S2 (C_{std}), the analyte concentration in the sample can be obtained.

The performance of MEC has been evaluated for various complex samples and instrumental methods such as inductively coupled plasma optical emission spectrometry (ICP OES) [11], microwave-induced plasma optical emission spectrometry (MIP-OES) [11,13], high-resolution continuum source flame atomic absorption spectrometry (HR-CS FAAS) [11], ultraviolet-visible spectroscopy (UV–Vis) and fluorescence spectroscopy [14], and LIBS [8,15–18].

Two-point calibration transfer was successfully applied for LIBS analysis of electronic waste based on the amount of sample ablated [12]. The linear model is calculated with only two points for each emission line, where the *x*-axis is the reached area of these two points and the *y*-axis is the signal intensity of both points. This strategy is applied for a standard and test samples, so the analyte concentration can be determined by the combination of the slopes from both curves and the standard concentration (known) using, Eq. (1) [12,19]:

$$C_x = C_{std} \times \frac{slope_x}{slope_{std}} \quad (1)$$

where C_x is the unknown sample concentration; C_{std} is the standard concentration; $slope_x$ is the slope of the linear model from the unknown sample and $slope_{std}$ is the slope of the linear model from the standard concentration.

Usually matrix effects are associated to complex samples, particularly when appropriate CRMs are not available for calibration. For instance, electronic waste (e-waste) is among the most complex matrix in terms of composition, heterogeneity, and contain a large amount of hazardous, base and precious elements including rare earth elements (REEs) [20–22]. In the present study, magnet samples from computer hard drive disks (HDDs) were interrogated in terms of technological composition by XRF using direct analysis. From electronic aspects, these magnets are made of Nd-Fe-B alloys composed of several REEs with magnetic, luminescent, optical and thermal properties [23–25].

The goal of this study was to evaluate different approaches of calibration methods not reported for XRF. For instance, Nd determination in HDD was exemplified and special attention was given to overcome problems related to matrix effects for complex samples. To the best of our knowledge, OP GSA, MEC, and TP CT methods have not yet been applied to WD XRF technique.

2. Material and methods

2.1. Instrumentation

A Perform-X ARL (Thermo Fischer, Madison, WI, USA) wavelength dispersive X-ray fluorescence (WD XRF) was used for direct analyses of high-performance magnets. The samples were irradiated with X-ray emission provided by a Rh tube with a maximum power of 4200 W. The instrument is equipped with five different crystals that can be used in the wavelength dispersion, ranging from 0.124 Å (0.0124 nm, LiF220) to 162.662 Å (16.2662 nm, AX16c), and the choice is based on which crystal can disperse the characteristic wavelength from the analyte. The instrument is also equipped with four different collimators (0.15 mm, 0.40 mm, 1.00 mm and 2.60 mm) and two detectors: a flow proportional counter (FPC) and a scintillation counter (SC). Two elliptical masks of 0.50 mm and 10 mm were used to perform the analysis. The electronic transitions Nd $L\gamma_1$ (0.187 nm), Nd $L\beta_2$ (0.203 nm), Nd $L\beta_3$ (0.212 nm), Nd $L\beta_4$ (0.216 nm) and Nd $L\alpha_1$ (0.237 nm) were monitored. The current and the voltage applied to the X-ray source were 50 mA and 60 kV (3000 W), respectively.

Reference Nd concentrations were obtained using an inductively coupled plasma optical emission spectrometer (ICP OES) (iCAP 7000, Thermo Scientific, Waltham, MA, USA), after acid decomposition of the samples ($n = 3$) in hot block digestor (Marconi, Piracicaba, São Paulo State, Brazil). The emission line monitored was Nd 378.425 nm using axial viewing, and the instrumental conditions were established as the manufacturer recommendations

2.2. Reagents, solutions and samples

All solutions used in the ICP OES determinations were prepared using high purity water (18.2 MΩ cm resistivity) obtained from a Milli-Q® Plus Total Water System (Millipore Corp., Bedford, MA, USA). Nitric acid was purified by a Distillacid™ BSB-939-IR sub-boiling distillation system (Berghof, Eningen, Germany) and used to digest the samples. All glassware and polypropylene vessels were prior decontaminated by detergent washing, soaking in 10% (*v*/v) HNO_3 for 24 h, and then thorough rinsing with distilled-deionized water.

Standard solutions used to build the ICP OES calibration curve were prepared by the appropriate dilution of stock standard solutions containing 1000 mg L^{-1} Nd (Specsol, São Paulo, Brazil) in 10% (*v*/v) HNO_3.

In order to prepare solid calibration standards, sodium carbonate (Merck, Darmstadt, Germany) and microcrystalline cellulose (Synth, São Paulo, Brazil) were used as diluent (blank) and binder, respectively.

In HDDs, there are two types of high-performance magnets: actuator and spindle motor, but, in this study, only the actuator magnets were used. The small size of the magnets limited the milling process of each magnet individually. Then, the strategy was separate the 56 magnets into 8 different groups (named M1-M8) from 5 to 13 individual subsamples, according to devices manufacturer to obtain sufficient mass for the milling process. More details can be seen in Castro & Pereira-Filho [21].

2.3. Sample preparation for Nd determination by ICP OES

An ICP OES was used as analytical technique to determine the reference concentrations of Nd in magnets after acid decomposition of the samples. First, the samples were heated in a furnace at 500 °C approximately two hours for the elimination of the magnetic field. Then, they were ground in a knife mill (IKA, A11) to obtain a more homogeneous sample. Approximately 100 mg was accurately weighed in perfluoroalkoxy (PFA) tubes and subsequently added 10 mL of 7 mol L^{-1} HNO_3 for decomposition ($n = 3$) in hot block digestor during two hours at 100 °C, as optimized by Castro & Pereira-Filho [21].

2.4. Univariate calibration strategies for Nd determination

Three univariate calibration strategies for determination of the Nd in magnets by WD XRF were evaluated: i) MEC, ii) OP GSA and iii) TP CT. All these strategies use an efficient matrix-matching method, because the calibration curve and linear models are obtained using standards in the presence of the matrix of each sample. Data handling is the main difference among these three strategies.

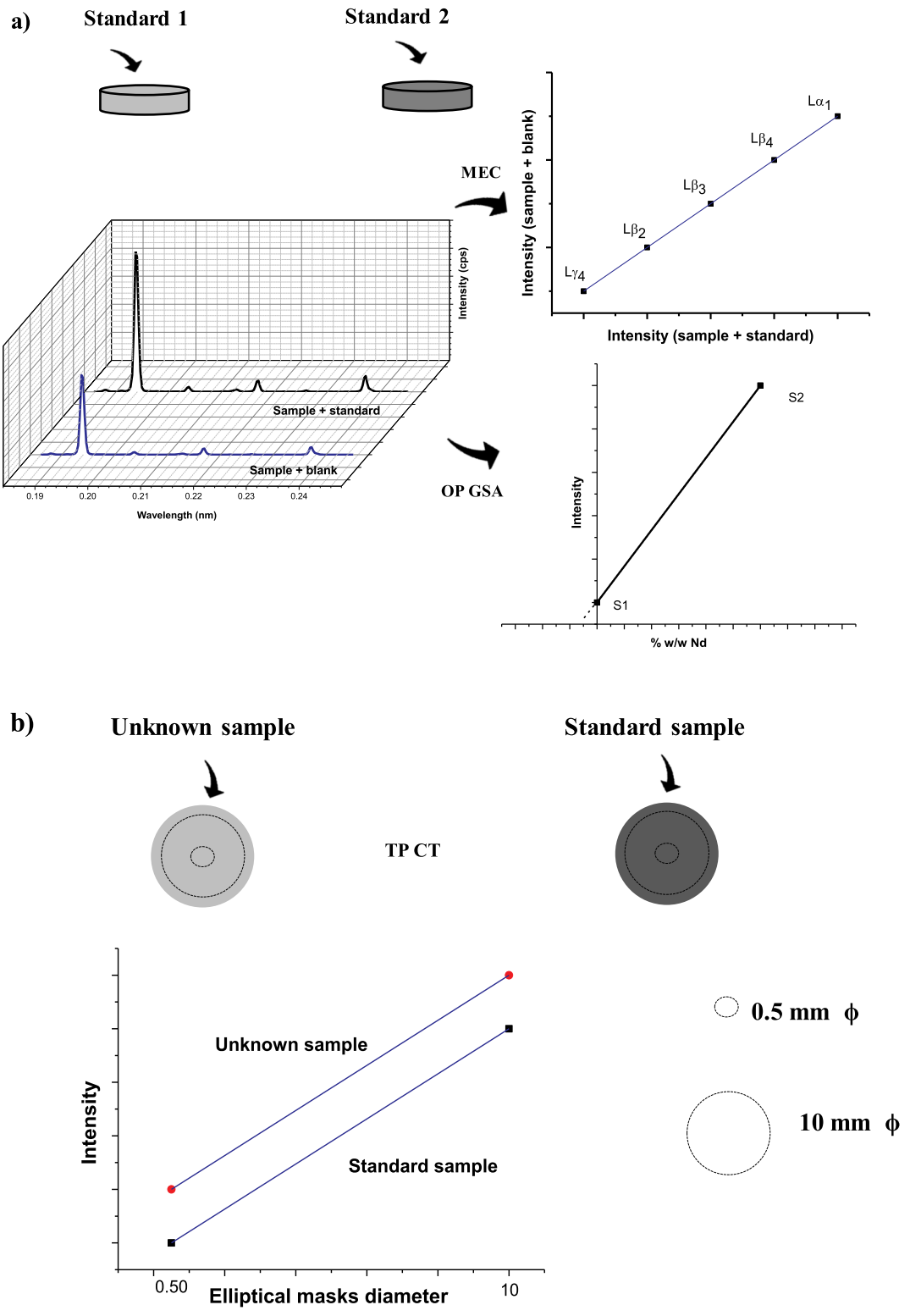

Fig. 1. Schematic representation of (a) MEC and OP GSA, standard 1 (Sample + Blank): 0.25 g sample, 0.3 g Na_2CO_3 and 0.05 g microcrystalline cellulose, and standard 2 (Sample + Standard): 0.25 g sample, 0.3 g M8 sample and 0.05 g microcrystalline cellulose, (b) TP CT, unknown sample: 1 g sample and 0.2 g microcrystalline cellulose, and standard sample: 1 g M8 sample and 0.2 g microcrystalline cellulose, for WD XRF analysis procedure.

For MEC and OP GSA, only two calibration standards are required for each sample. The standard 1 (S1) consisting of sample + blank; and the standard 2 (S2) consisting of sample + Nd standard. The S1 was composed of 0.25 g of sample, 0.30 g of blank (Na_2CO_3) and 0.05 g of binder (microcrystalline cellulose). The S2 was composed of 0.25 g of sample, 0.30 g of Nd standard and 0.05 g of binder. The sample named M8 containing 24.51% w w^{-1} Nd, was used as a standard to prepare S2 for both MEC and OP GSA calibrations.

For TP CT, the sample preparation for WD XRF analysis was simple and consisted of mixing 1 g of milled magnet sample with 0.2 g of microcrystalline cellulose (as a binder). The sample M8 (1 g of M8 sample with 0.2 g of microcrystalline cellulose) was also used as a

standard for TP CT.

All mixtures were homogenized with a mortar and pestle and pressed (60 kN for 2 min) to form pellets (approximately 13 mm diameter). These pellets were also prepared in triplicate. Fig. 1 shows a schematic representation of the MEC, OP GSA (both Fig. 1a) and TP CT (Fig. 1b) procedures for WD XRF analysis.

Using the counting time of 2 s, 0.15 mm collimator, elliptical masks of 0.50 mm (for TP CT) and 10 mm (for MEC, OP GSA, TP CT), 0.1° increment, LiF 200 as diffraction crystal, and scintillation counter detector, all solid samples and standards were analyzed in the scan mode by monitoring spectral windows for diffraction angles 2θ from 57 to 75° related to Nd $L\gamma_1$ (2θ - 55.606° or λ1–0.187 nm), Nd $L\beta_2$ (2θ - 60.746° or λ2–0.203 nm), Nd $L\beta_3$ (2θ - 63.781° or λ3–0.212 nm), Nd $L\beta_4$ (2θ - 65.120° or λ4–0.216 nm), and Nd $L\alpha_1$ (2θ - 72.125° or λ5–0.237 nm) electronic transitions.

Three authentic replicates were prepared to evaluate the precision of the model according to relative standard deviation (RSD). Besides that, the standard error (SE) was calculated for all calibration strategies according to Eq. (2):

$$SE = \sqrt{\frac{\sum (y_i - \hat{y}_i)^2}{n - 1}} \quad (2)$$

where y_i is the Nd reference concentration obtained by ICP OES, $\hat{y}_i$ is the concentration predicted by the linear model using WD XRF and n is the number of samples.

3. Results and discussion

In this study, three univariate calibration methods (MEC, OP GSA and TP CT) were performed in order to determine Nd in samples of high-performance magnets.

One of the advantages to determine Nd is the possibility to use only one crystal with five different electronic transitions, which make the analysis faster than when it is necessary to change the crystal. Besides that, there is a lot of interference between Nd and Pr. But, in this case, it was not a problem due to a high amount of Nd in the magnets. The typical Pr concentration in the analyzed samples ranged from 1 to 5% w w^{-1} [21]. Fig. 2 shows the intensity of the different transitions chosen for Nd. Fig. 2a presents the signal used for MEC and OP GSA, for both pellets (S1 and S2), while Fig. 2b and c is for TP CT with 0.50 mm and 10 mm of elliptical mask, respectively.

The analysis for TP CT was made in two different diameters of elliptical mask. This approach is necessary due to the fact that is needed 2 points to build the linear model. Fig. 2b shows the signal with 0.50 mm of elliptical mask, a smaller area of the sample was irradiated, retrieving, as expected, lower intensity when compared to 10 mm of elliptical mask, where the irradiated area is larger. It is important that the intensity of point 2 must be higher than the point 1. As can be observed in Fig. 2b and c, even with low intensities, using 0.50 mm of elliptical mask (Fig. 2b), it was possible to build the linear models with good statistical parameters. The linearity was evaluated calculating an F-test, where the ratio between the $F_{calculated}$ and $F_{tabulated}$ being higher than 10 is preferably. These F values were accounted using the mean of square for Regression (MSR) and residue (MSr).

Fig. 3 shows the three univariate models for sample M3. For MEC (Fig. 3a), a linear model was calculated with the 5 transitions of Nd with a R^2 close to 1, trueness of 94% and RSD of 14%. The Nd concentration was determined using Eq. (3):

$$C_{Nd} = \frac{Slope \times C_{std}}{1 - Slope} \quad (3)$$

One of the advantages for MEC is the possibility to identify spectral interference in electronic transition used in the linear model. If any specific transition has spectral interference, the point (Nd transition) can be removed from the linear model, improving the correlation. But in this case, the Nd concentration in the samples is very high and spectral interferences were not identified in the monitored electronic transitions to Nd by WD XRF. The trueness for all models was calculated according to reference values obtained by ICP OES.

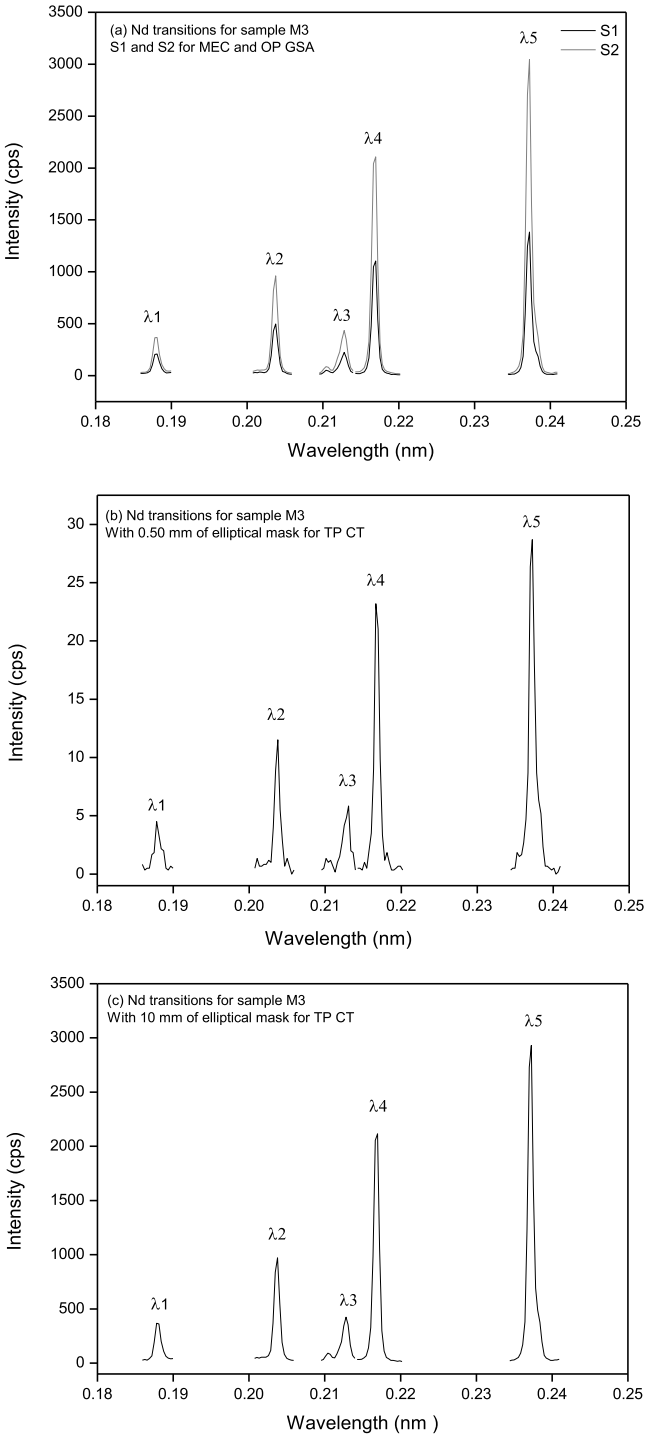

Fig. 2. Spectral intensities of Nd electronic transitions for (a) MEC and OP GSA, (b) TP CT with 0.50 mm of elliptical mask, and (c) TP CT with 10 mm of elliptical mask.

For OP GSA (Fig. 3b), the calibration curve was built according to gravimetric approach, considering the masses of standard, unknown sample and diluent (*x*-axis and *y*-axis) [8]. The Nd concentration is based in the extrapolation method and is calculated by Eq. (4):

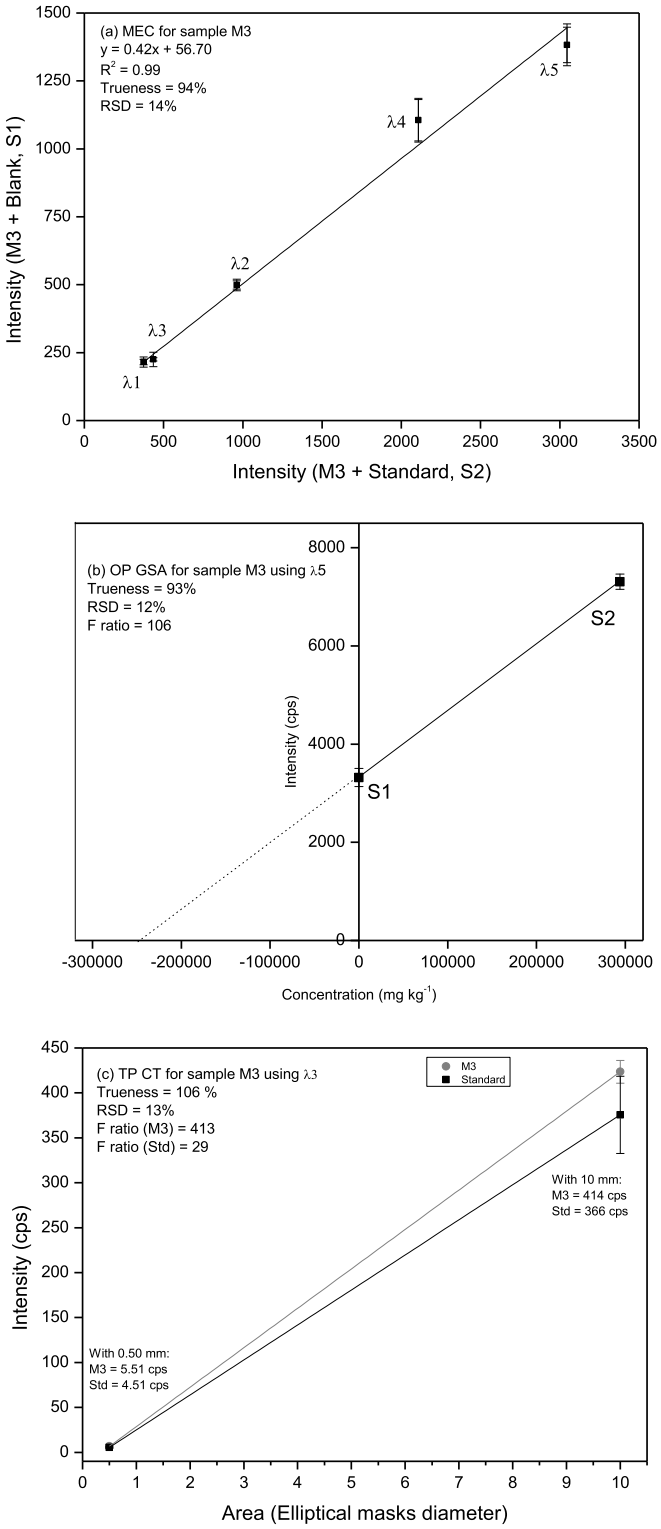

Fig. 3. Univariate models for sample M3 using (a) MEC, (b) OP GSA and (c) TP CT. These results are the average of triplicate values and the error bars are the standard deviation of the triplicate.

$$C_{Nd} = \frac{Intercept}{Slope} \quad (4)$$

In this method, only two calibration standards are necessary (S1 and S2) monitoring only one Nd electronic transition, as it can be observed in Fig. 3b. The linearity was also tested by F test, which, in this case, the ratio between $F_{experimental}$ and $F_{tabulated}$ was 106, demonstrating the variances from regression and residue are statistically different at 95% confidence level, so the model can be considered linear. Besides that, trueness of 93% and RSD of 12% were obtained.

Fig. 3c shows the TP CT model for sample M3. As in the OP GSA, only one Nd transition is monitored and is made a calibration transfer between the standard and unknown sample. The Nd concentration in the unknown sample is calculated by Eq. (1).

One crucial aspect in the TP CT is the similarity between the standard and unknown sample. Good results are obtained if they are similar. In this case, trueness of 106%, RSD of 13% and an F ratio higher than 10 for both (standard and sample M3) were obtained.

All the parameters of the calibration methods for each sample are showed in Table 1, as well as the Nd concentration obtained by ICP OES and the RSD values. Five Nd transitions were tested for OP GSA and TP CT, but the best transition for each sample was chosen according to trueness and RSD, as observed in Table 1. But, even with the selection of one electronic transition for each sample, for TP CT, it is important to mention that all the 5 transitions presented good results for all samples (M1 – M7). The trueness ranged from 97 to 118% and RSD from 5 to 19% among all samples and transitions, this is an advantage because is possible use any Nd transition with good figures of merit and repeatability.

On the other hand, for OP GSA, the results change from one sample to other. For M7, just the transition 5 (λ5) presented good result (even being a little bit above 120% trueness), but for other samples (M4 and M5), this transition 5 presented low values of trueness (bellow 80%). Another example is the transition 1 (λ1), that presented high values of trueness for all samples, except for M5.

Another parameter presented in Table 1 is the F ratio for OP GSA and TP CT. In addition, Fig. 4 shows the trueness obtained according to Nd concentration calculated with the WD XRF models and the Nd reference concentration determined by ICP OES.

For almost all samples, the trueness values were in the acceptable range from 80 to 120% (between the lines in Fig. 4). The values ranged from 65 to 126% for MEC, 80 to 127% for OP GSA and 99 to 114% for TP CT. The RSD values ranged from 3 to 26%, from 4 to 27% and from 5 to 13% for MEC, OP GSA and TP CT, respectively. The F tests performed for OP GSA and TP CT presented ratios ($F_{calculated}/F_{tabulated}$) above 10, showing a good linearity for both cases. The standard errors were 2, 4 and 6% w w^{-1} Nd for TP CT, OP GSA and MEC, respectively, being far below the average Nd concentration (see Table 1). Another advantage of these proposed methods is the use of the raw data, none normalization was performed.

When comparing the three methods, is notable that MEC presented trueness values worse than the other methods for some samples. But note that, in MEC, all the electronic transitions of Nd are used, while in the other methods, it is necessary only to choose the best one. An advantage to use more than one transition of Nd is the possibility to observe the spectral interferences, as already mentioned.

A favorable aspect for MEC and OP GSA is the powerful matrix-matching procedure using only two calibration standard *per* sample, which efficiently corrects or minimizes matrix effects enabling quantitative results with satisfactory accuracy and precision. These two calibration standards require a certain amount of time to prepare and are laborious if the number of samples is high. Other crucial point is the choice of the diluent in these standards. In some cases, the transition lines for diluent can interfere in the transition lines for the element of interest. Therefore, a special careful is needed.

For TP CT, the sample preparation and data treatment are very simple and fast, the only aspect that needs attention is the choice of the standard, which have to present similar matrix with the unknown sample. This can be a problem when the interest element has a very large concentration range in the samples.

Table 1
Nd reference concentration obtained by ICP OES for all samples, RSD value for all calibration strategies, wavelength (electronic transition used for OP GSA and TP CT), and F ratio calculated (for OP GSA and TP CT linear models).

Samples	Nd concentration – ICP OES (% w w^{-1})	RSD (%)			Wavelength (nm), see details in Fig. 2		F ratio		
		MEC	OP GSA	TP CT	OP GSA	TP CT	OP GSA	TP CT (sample)	TP CT (Std)
M1	25.62	25	6	12	λ3	λ1	19	295	36
M2	25.55	4	6	11	λ5	λ4	249	1272	37
M3	26.33	14	12	13	λ5	λ3	106	413	29
M4	25.75	26	27	5	λ3	λ5	34	200	55
M5	25.93	3	4	13	λ4	λ2	593	202	44
M6	24.99	5	5	10	λ4	λ3	243	1535	29
M7	23.52	8	7	11	λ5	λ1	233	1050	36
Range	23.52–26.33	3–26	4–27	5–13	–	–	19–593	295–1535	29–55
Average	25.38	12	10	11	–	–	211	710	38

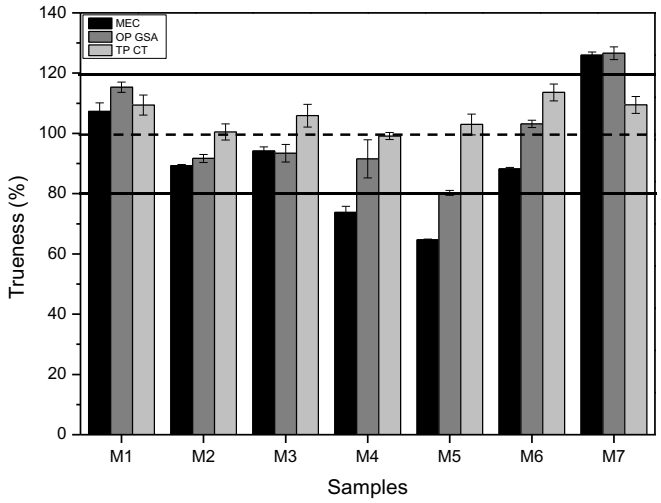

Fig. 4. Trueness (%) for all samples using the three univariate calibration strategies (MEC, OP GSA and TP CT). These results are the average of triplicate values and the error bars are the standard deviation of the triplicate.

4. Conclusion

After testing three new methods of calibration for WD XRF analysis, it is notable that there is no perfect and standardized procedure for overcoming all analytical problems. Each strategy can be useful for a given situation such as identify spectral interferences (MEC), overcome severe matrix effects (OP GSA), or use of a single standard for calibration (TP CT). All the proposed models presented good results for direct Nd determination in magnets, making a powerful combination between these three univariate calibration approaches and WD XRF for characterization of Nd in the recycling process of e-waste. On the other hand, TP CT seems to be more robust because good results were obtained for all samples and the Nd electronic transition selection was not a critical aspect.

Declaration of Competing Interest

The authors declare that they have no known competing financial interests or personal relationships that could have appeared to influence the work reported in this paper.

Acknowledgments

This study was supported by the São Paulo Research Foundation (FAPESP, grants 2012/01769-3, 2012/50827-6, 2014/22408-4, 2016/01513-0, 2016/17221-8, 2016/17304-0 and 2018/17753-5) and Conselho Nacional de Desenvolvimento Científico e Tecnológico (CNPq, 401074/2014-5, 305637/2015-0, 160152/2015-1, and 141311/2017-7). This study was financed in part by the Coordenação de Aperfeiçoamento de Pessoal de Nível Superior - Brasil (CAPES) - Finance Code 001. The authors are also grateful to Thermo Scientific for WD XRF measurements.

References

[1] U. Kurfürst, Solid Sample Analysis, Springer-Verlag, Berlin, 1998.
[2] G.G.A. Carvalho, M.B.B. Guerra, A. Adame, C.S. Nomura, P.V. Oliveira, H.W.P. Carvalho, D. Santos Jr., L.C. Nunes, F.J. Krug, Recent advances in LIBS and XRF for the analysis of plants, J. Anal. At. Spectrom. 33 (2018) 919–944.
[3] M. West, A.T. Ellis, P.J. Potts, C. Streli, C. Vanhoof, D. Wegrzynekf, P. Wobrauschek, Atomic spectrometry update – a review of advances in X-ray fluorescence spectrometry, J. Anal. At. Spectrom. 28 (2013) (2013) 1544–1590.
[4] G.L. Donati, R.S. Amais, Fundamentals and new approaches to calibration in atomic spectrometry, J. Anal. At. Spectrom. 34 (2019) 2353–2369.
[5] D.V. Babos, V.C. Costa, M.A. Sperança, E.R. Pereira-Filho, Direct determination of calcium and phosphorus in mineral supplements for cattle by wavelength dispersive X-ray fluorescence (WD-XRF), Microchem. J. 137 (2018) 272–276.
[6] Z. Mzyk, J. Anyszkiewicz, T. Gorewoda, Special tablets containing cellulose binder and Sr internal standard for simplifying X-ray fluorescence analysis of powder samples, Spectrochim. Acta, Part B 114 (2015) 15–19.
[7] J.C. Chan, P.T. Palmer, Determination of calcium in powdered milk via X-ray fluorescence using external standard and standard addition based methods, J. Chem. Educ. 90 (2013) 1218–1221.
[8] D.V. Babos, A.I. Barros, J.A. Nóbrega, E.R. Pereira-Filho, Calibration strategies to overcome matrix effects in laser-induced breakdown spectroscopy: direct calcium and phosphorus determination in solid mineral supplements, Spectrochim. Acta, Part B 155 (2019) 90–98.
[9] Y. Gao, R.E. Sturgeon, Z. Mester, X. Hou, L. Yang, Multivariate optimization of photochemical vapor generation for direct determination of arsenic in seawater by inductively coupled plasma mass spectrometry, Anal. Chim. Acta 901 (2015) 34–40.
[10] Y. Gao, R.E. Sturgeon, Z. Mester, X. Hou, C. Zheng, L. Yang, Direct determination of trace antimony in natural waters by photochemical vapor generation ICP-MS: method optimization and comparison of quantitation strategies, Anal. Chem. 87 (2015) 7996–8004.
[11] A. Virgilio, D.A. Gonçalves, T. McSweeney, J.A.G. Neto, J.A. Nóbrega, G.L. Donati, Multi-energy calibration applied to atomic spectrometry, Anal. Chim. Acta 982 (2017) 31–36.
[12] J.P. Castro, D.V. Babos, E.R. Pereira-Filho, Calibration strategies for the direct determination of rare earth elements in hard disk magnets using laser-induced breakdown spectroscopy, Talanta 208 (2019) 120443.
[13] R.C. Machado, A.B.S. Silva, G.L. Donati, A.R.A. Nogueira, Multi-energy calibration as a strategy for fertilizer elemental analysis by microwave-induced plasma optical emission spectrometry, J. Anal. At. Spectrom. 33 (2018) 1168–1172.
[14] M.C. Alencar, D.A. Gonçalves, G. Nicolodelli, S.L. Oliveira, G.L. Donati, A.R.L. Caires, Evaluating the applicability of multi-energy calibration as an alternative method for quantitative molecular spectroscopy analysis, Spectrochim. Acta, Part A (2019), https://doi.org/10.1016/j.saa.2019.117221.
[15] D.V. Babos, A. Virgílio, V.C. Costa, G.L. Donati, E.R. Pereira-Filho, Multi-energy calibration (MEC) applied to laser-induced breakdown spectroscopy (LIBS), J. Anal. At. Spectrom. 33 (2018) 1753–1762.
[16] A.S. Augusto, J.P. Castro, M.A. Sperança, E.R. Pereira-Filho, Combination of multi-energy calibration (MEC) and laser-induced breakdown spectroscopy (LIBS) for dietary supplements analysis and determination of Ca, Mg and K, J. Braz. Chem. Soc. 30 (2019) 804–812.
[17] F.M. Fortunato, T.A. Catelani, M.S. Pomares-Alfonso, E.R. Pereira-Filho, Application of multi-energy calibration for determination of chromium and nickel in nickeliferous ores by laser-induced breakdown spectroscopy, Anal. Sci. 35 (2019) 165–168.
[18] D.F. Andrade, F.M. Fortunato, E.R. Pereira-Filho, Calibration strategies for

determination of the In content in discarded liquid crystal displays (LCD) from mobile phones using laser-induced breakdown spectroscopy (LIBS), Anal. Chim. Acta 1061 (2019) 42–49.

[19] L.C. Nunes, F.R.P. Rocha, F.J. Krug, Slope ratio calibration for analysis of plant leaves by laser-induced breakdown spectroscopy, J. Anal. At. Spectrom. 34 (2019) 2314–2324.

[20] C.P. Baldé, V. Forti, V. Gray, R. Kuehr, P. Stegmann, The Global E-waste Monitor – 2017, United Nations University (UNU), International Telecommunication Union (ITU) & International Solid Waste Association (ISWA), Vienna, 2017.

[21] J.P. Castro, E.R. Pereira-Filho, Spectroanalytical method for evaluating the technological elements composition of magnets from computer hard disks, Talanta 189 (2018) 205–210.

[22] D.F. Andrade, J.P. Romanelli, E.R. Pereira-Filho, Past and emerging topics related to electronic waste management: top countries, trends, and perspectives, Environ. Sci. Pollut. Res. 26 (2019) 17135–17151.

[23] K. Habib, K. Parajuly, H. Wenzel, Tracking the flow of resources in electronic waste – the case of end-of-life computer hard disk drives, Environ. Sci. Technol. 49 (2015) 12441–12449.

[24] P.C.S. Filho, O.A. Serra, Terras raras no Brasil: histórico, produção e perspectivas, Quim. Nova 37 (2014) 753–760.

[25] S. Zhang, Y. Ding, B. Liu, C.C. Chang, Supply and demand of some critical metals and present status of their recycling in WEEE, Waste Manag. 65 (2017) 113–127.

Chapter 4. Characterization of LIBS spectra by PARAFAC

4. Characterization of LIBS spectra by PARAFAC

Parallel Factor Analysis (PARAFAC) is a decomposition method for multi-way data and it is considered a principal component analysis (PCA) generalization. In a three-way data, the structural base is given by A, B and C (loadings) containing a_{if}, b_{jf} and c_{kj} related to the three dimensions of the data (Figure 4), which means, data measured as a function of three factors [91,92]. For LIBS, samples, variables (emission lines) and depths, for example.

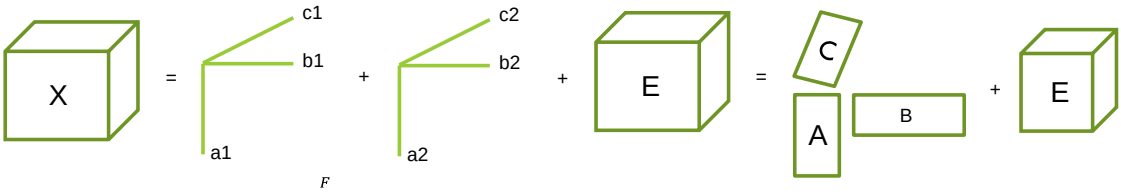

$$x_{ijk} = \sum_{f=1}^{F} a_{if} b_{jf} c_{kf} + \varepsilon_{ijk}, i = 1,\ldots,I; j = 1,\ldots,J; k = 1,\ldots,K;$$

Figure 4. Structural base for three-way data by PARAFAC.

Where x_{ijk} is the emission line intensity of sample i measured at emission line j and pulse k; ε_{ijk} is the variation not explained by the model (residuals); a_{if}, b_{jf} and c_{kf} describe the importance of the samples/variables of each component (F, number of components). The model is calculated by Alternating Least Square (ALS) and, this algorithm estimates the value of one of the loadings from the values of the others, starting with random values until reaching a convergence criterion [91].

As result, PARAFAC will provide a unique solution: mixtures of analytes can be separated, relative concentrations, pure spectra and profiles can be estimated, if the data are trilinear, number of components are chosen correctly and the data must have a good signal-to-noise ratio. This characteristic of PARAFAC is the uniqueness and, it is the great advantage of this method [91,92].

The crucial aspect is the choice of the components number and, besides the knowledge of the analyst about the system, explained variance, split-half analysis and core consistency diagnostic (CORCONDIA) can assist [93,94]. For split-half analysis, it is necessary to split the data into two sets, for example, and then calculate the PARAFAC model for both sets, if the number of components is correct, both models will provide the same result due to the uniqueness of PARAFAC [94]. The CORCONDIA method is a calculation to verify how much

the data are trilinear, the ideal model is that with higher number of components but that preserves the trilinear structure [93].

Other possibility is the constraints use, as an example, the non-negativity. This application avoids negative spectra that are not in accordance with the expected nature of LIBS data. Orthogonality and unimodality are other examples for constraints [94].

For a quantitative analysis, the estimated scores for the samples can be used to predict their real concentration with the advantage of second order: possibility of calibration in the presence of unknown interferents that are not present in the calibration set [91,92].

In this chapter, PARAFAC was used to characterize the LIBS spectra from PCB analysis by LIBS, being the first study about PARAFAC and LIBS in the literature. This study was made during my internship abroad at the University of Copenhagen under supervision of Dr. Rasmus Bro.

4.1. Laser-induced breakdown spectroscopy (LIBS) spectra interpretation and characterization using parallel factor analysis (PARAFAC): a new procedure for data and spectral interference processing fostering the waste electrical and electronic equipment (WEEE) recycling process

JAAS

ROYAL SOCIETY OF CHEMISTRY

PAPER

Cite this: *J. Anal. At. Spectrom.*, 2020, **35**, 1115

Laser-induced breakdown spectroscopy (LIBS) spectra interpretation and characterization using parallel factor analysis (PARAFAC): a new procedure for data and spectral interference processing fostering the waste electrical and electronic equipment (WEEE) recycling process†

Jeyne Pricylla Castro,[ab] Edenir Rodrigues Pereira-Filho *[b] and Rasmus Bro[a]

Laser-induced breakdown spectroscopy (LIBS) was used to characterize base (Al and Cu) and noble (Au and Ag) elements on a printed circuit board (PCB) from a hard disk (HD). A PCB was cut into 77 fragments, and a matrix of 4 rows and 4 columns with 10 laser pulses in each point of the matrix was acquired in each fragment by LIBS. For each element, a spectral range was selected with its respective emission lines and Parallel Factor Analysis (PARAFAC) was used to model the data. LIBS spectra are two-way data, but in this case, the depths were used as a third mode being the data set: samples × variables (emission lines) × depths (laser pulses from 1 to 10). PARAFAC was able to model spectral interference and analyte emission lines in separate components, which allows the removal of the contribution of the concomitants from the measured data. The scores (relative concentrations, mode 1) of the component of interest were used to create a map of the PCB colored by relative concentration, and it was possible to visualize where the element is predominantly located on the PCB. In addition, classification models were applied for Au and Ag using partial least squares discriminant analysis (PLSDA) after removal of the interferents using the PARAFAC result. Good figures of merit were obtained for calibration, cross-validation and validation data sets with accuracy ranging from 0.94 to 1.00. Therefore, the use of PARAFAC and LIBS spectra was very useful, being a great contribution to the LIBS community and urban mining.

Received 29th January 2020
Accepted 24th March 2020

DOI: 10.1039/d0ja00026d

rsc.li/jaas

1. Introduction

Electrical and electronic equipment (EEE) presents in its chemical composition several important elements due to their unique physical and chemical properties. These elements can be categorized as noble (Ag, Au), base (Al, Cu) and technological (In, among others), which make EEE functional, but as a consequence, obsolete EEE is very complex, highly heterogeneous and difficult to recycle. The worldwide number of users of technological products is growing at great speed with the social and economic advance, and innovation. Nowadays, many people have more than one electronic device (mobile phones, tablets, and personal computers, among others), which can be replaced by new ones in a short period of time, varying from 1 to 2 years in the case of mobile phones.

The huge demand for critical metals can cause their deficiency in the Earth's crust, leading to supply risks in the future, and fostering the interest in secondary resources, such as e-waste recycling. The world generation of e-waste in 2016, for example, was around 45 million metric tons, which is equivalent to almost 4500 Eiffel towers. In 2021 the expected e-waste generation can reach an alarming value of more than 50 million metric tons. This huge amount of e-waste presents complex, diverse and rich composition, being a source of scarce and valuable raw materials.[1–3]

The correct recycling of e-waste depends on proper characterization of these materials, including the development of reliable analytical methods.[4–7] Laser-induced breakdown spectroscopy (LIBS) is a technique where direct solid analysis is possible with high analytical frequency and minimum sample preparation. On the other hand, direct analysis presents several difficulties in the reproduction of the data due to the ablation process, plasma formation, microheterogeneity and matrix

[a]*Department of Food Science, University of Copenhagen, Copenhagen, Denmark*
[b]*Group of Applied Instrumental Analysis, Chemistry Department, Federal University of São Carlos, P. O. Box 676, São Carlos, São Paulo State, 13565-905, Brazil. E-mail: erpf@ufscar.br*

† Presented at the 2020 Winter Conference on Plasma Spectrochemistry, Tucson, AZ, USA.

effects, which can be circumvented by combining LIBS spectra with chemometrics.[8–13]

Due to sample heterogeneity, LIBS spectra of these materials are very complex with thousands of emission lines in which the emission line of one element may interfere with another. This can be a problem for some elements with low concentration in the sample or when all emission lines from the element of interest have some spectral interference, compromising the analysis.[14]

Parallel factor analysis (PARAFAC)[15] is a decomposition method applied for multi-way data (higher order data arranged in boxes). It can estimate the spectra and concentration profiles of the underlying chemical analytes if the data behave according to the model. The decomposition uses trilinear components, with each component consisting of one score and two loading vectors. It can be considered a generalization of Principal Component Analysis (PCA) for multi-way data, but with an advantage over bilinear methods, which is the uniqueness of the solution. This method has no limitations with rotational freedom. So, the true underlying spectra will be found if the data is trilinear, the right number of components is chosen and the signal-to-noise ratio is not prohibitively bad.[15–17]

Fluorescence[18–21] and chromatography[22–24] data are the most common application areas of PARAFAC with several examples in the literature. These examples include applications for chemical characterization,[25–27] multivariate calibration,[28] exploratory analysis,[29] and so on. But for LIBS, it is worth mentioning that there is no study combining LIBS emission spectra and PARAFAC modeling.

The aim of this study is the characterization of metals on a printed circuit board (PCB) from a hard disk (HD), an e-waste type with a very rich composition. Base (Al and Cu) and noble (Au and Ag) elements were investigated. To model the data, PARAFAC was used for the first time, being a potential and reliable approach to identify and handle spectral interferences. In addition, using the PARAFAC results, reliable classification models were applied for the noble elements using partial least squares discriminant analysis (PLSDA).

2. Materials and methods

2.1 Sample preparation

An obsolete PCB from a HD is a special type of WEEE, composed of several chips and other technological characteristics. This PCB is responsible for several actions, such as the movement of the disks and read/write heads, recording and receiving data between the disk and the computer, as well as the routines related to data security.

It is clear that these PCBs present several base, noble and technological elements that can be recycled and used in the manufacturing of new electronic devices. In this case, in order to simulate a crushing machine in industry, one PCB from a HD was chosen and cut into 77 fragments (11 rows and 7 columns) with around 10 by 10 mm. Each fragment was taken as an individual sample and it was further analyzed by LIBS.

2.2 LIBS setup, data set acquisition and organization

The LIBS instrument used in this study was a model J200 from Applied Spectra (Fremont, CA) equipped with a 1064 nm Nd:YAG laser and pulse duration of 8 ns. The spectrometer is a 6-channel charge-coupled device (CCD) with 12 288 pixels that covers a spectral range from 186 to 1042 nm. Some instrumental conditions can be varied: delay time (0 to 2 μs), spot size (50 to 250 μm), laser pulse energy (0 to 100 mJ) and laser repetition rate (1 to 10 Hz). The analysis can be acquired using raster, matrix or punctual modes.

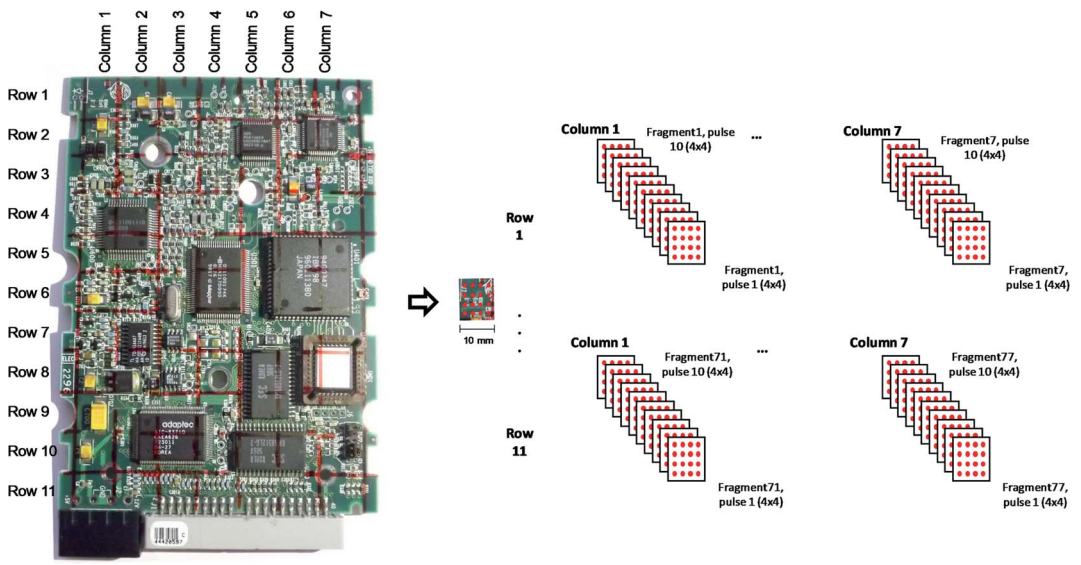

Fig. 1 Description of the data acquisition and organization.

In this study, the LIBS instrumental conditions were fixed at 100 mJ of laser pulse energy, 100 μm of spot size, 1 μs of delay time and 5 Hz of laser repetition rate. A matrix of 4 rows and 4 columns was performed on each of the 77 fragments and 10 laser pulses were acquired in each point of the matrix: ~160 spectra per fragment and a total of more than 12 000 spectra. The distance between the points was 1 mm. As the sample presents a heterogeneous feature with several components in high relief, the data acquisition was made manually. In some cases, the points fell into orifices, where the acquisition of the signal was not possible. Therefore, the final data set is 77 fragments × ~160 spectra, resulting in 12 100 spectra. Each spectrum has 12 288 variables (from 186 to 1042 nm). A pictorial description of the data acquisition and organization is shown in Fig. 1. The red horizontal and vertical lines were marked in order to visualize the PCB fragmentation. In addition, the red dots (4 × 4) represent the laser pulses applied in each fragment and from pulses 1 (surface of the sample) to 10 (bulk of the sample).

2.3 Multi-way data analysis using PARAFAC

The PARAFAC model is applied for multi-way data, which means that the acquired data set is measured as a function of three or more types of variables. For LIBS, two-way data were established for several depths, thus generating multi-way data. PARAFAC was used to model the data arranged in an $I \times J \times K$ three-way array. The first one (I) refers to the 77 samples (1210 spectra), the second (J) to the emission lines (wavelengths) and the third (K) to the pulses (depth, from 1 to 10), a pictorial description is shown in Fig. 2. In this figure only a spectrum section from 17 emission lines covering Cu 324.75 and 327.39 is shown as an example. The PARAFAC model can be written using eqn (1).

$$x_{ijk} = \sum_{f=1}^{F} a_{if} b_{jf} c_{kf} + \varepsilon_{ijk}, \quad i = 1, \ \ldots, \ I; \ j = 1 \ \ldots, \ J; \ k = 1 \ \ldots, \ K; \tag{1}$$

For LIBS analysis, x_{ijk} is the emission line intensity of sample i measured at emission line j and pulse k. The ε_{ijk} is the variation not explained by the model (residuals) and a_{if}, b_{jf} and c_{kf} describe the importance of the samples/variables of each component (F, number of components), a_{if} being proportional to the concentration of the f^{th} analyte in the sample i, b_{jf} an estimate of the emission spectrum of the f^{th} analyte up to a scaling factor and c_{kf} proportional to the depth of the f^{th} analyte in the pulse k. The model is calculated using the algorithm alternating least squares (ALS). Details about the calculation can be found in other publications.[15,30,31]

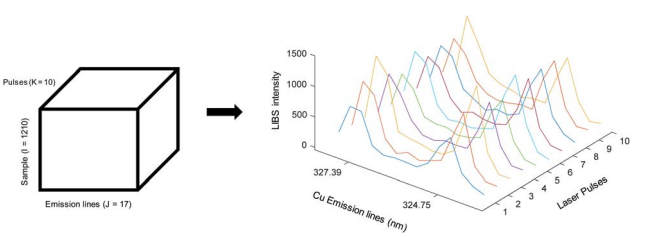

Fig. 2 Description of the $I \times J \times K$ three-way array for LIBS spectra.

Due to a high number of variables (12 288), variable selection was previously performed for each target element. Base (Al and Cu) and noble (Ag and Au) elements were studied. For Cu, for instance, two ranges of emission lines were chosen, I 324.75 and I 327.39 nm, a reduction from 12 288 to 17 variables. The index "I" means that these lines are atomic emission lines. For Al, from 12 288 to 17 variables, also two ranges of emission lines: I 394.4 and I 396.15 were chosen. In the case of Au and Ag, just one range of emission line was chosen, I 479.25 and I 338.28 nm, respectively (data reduction from 12 288 to 7 variables for each noble metal). These emission lines were selected because they had intense signals. In some cases, spectral interference was observed which was eliminated after data treatment that will be described in the next sections. So, the data set was defined by 1210 samples (77 samples × ~16 points), 24 variables for base (17 emission lines) and noble (7 emission lines) elements, and 10 pulses.

All the calculations were performed using MATLAB® 2018a (Mathworks, Natick, MA, USA) and PLS_Toolbox 8.7 software.

2.4 Classification models for noble elements' data inspection

Classification models were applied using PLSDA in order to verify the presence or absence of the noble elements in the fragments. With the results obtained from the PARAFAC model and interference removal from the data, individual PLSDA models were calculated for Au and Ag. The main step in this process was to find a suitable data set to perform the calculations, because for each fragment there are ~16 spectra (16 points), and it is impossible to perform the average of these spectra, due to the heterogeneity of the samples. Fig. 3 shows an example for fragment 1 and the problem of performing the average of the spectra. In this figure high analytical signals are observed for points 11, 1 and 5, but for the other points the analytical signal is low. The intensity of the average spectrum is too low compared to the spectrum of point 11 (high analytical signal). Therefore, several strategies were used to classify these samples and the most suitable solution is described below:

– Data sets: this part was organized into two data sets (Au and Ag) after interference removal with the dimensions 1210 samples × 7 variables × 10 pulses. First, selection of one pulse according to the PARAFAC model. Resulting data set: 1210 samples × 7 variables for the chosen pulse.

– Selection of the representative spectrum for each fragment. The strategy used was to select one of these spectra that presented higher intensity of the emission line. Final data sets: 77 samples × 7 variables.

– Due to lack of representative reference values for each fragment, one strategy for classification was to consider

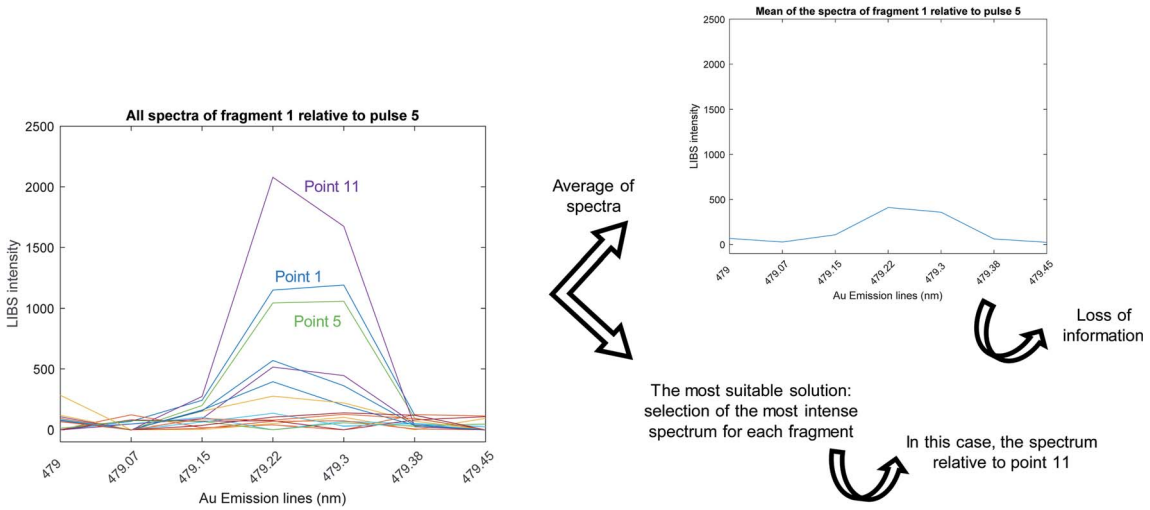

Fig. 3 Description of the heterogeneity problem for the fragments.

samples with intensity higher than 500 with Au and/or Ag (class 1) and samples with intensity below 500 without Au and/or Ag (class 0). The intensities below 500 are too low and can be confused with noise. In order to establish this threshold (500), we calculated the noise before and after the peak and multiplied it by 3 to ensure the presence of the element.

After the data set organization, mean centering was performed and two separate models were calculated. Cross validation using venetian blind with 6 and 3 splits was performed, for Au and Ag, respectively. For external validation, the data was split into calibration (66% of the data) and validation using the onion approach.[32] Figures of merit were evaluated:

– Sensitivity (true positive rate, TPR): model ability to avoid false negatives;

– Specificity (true negative rate, TNR): model ability to avoid false positives;

– Error rate (ER): estimation of the model error;

– Non-error rate (NER): capability to correctly classify;

– Accuracy: estimation of the model error, high accuracy means a good model;

– AUC: area under the ROC (Receiver Operating Characteristics) curve.

For two classes, sensitivity and specificity are "specular".[33] The strategy described in this section was performed for Au and Ag.

In order to verify the difference between the classification models from raw data and the data after removal of interference, the classification was also made for the raw data using the same parameters mentioned above.

3. Results and discussion

One of the major drawbacks related to LIBS spectra is spectral interference. In many cases, these interferences are present in the most intense emission lines of the elements jeopardizing the analysis. In order to minimize this problem, it is recommended to choose secondary emission lines that do not present any interference, which is a difficult task for some elements.[8]

The PARAFAC model has many advantages, and one of them is the uniqueness. This implies that the pure spectra, profiles and relative concentrations can be estimated and mixtures of analytes can be mathematically separated[15] if the data are following the structure of the PARAFAC model. This feature can be very important in LIBS data analysis, minimizing possible problems related to spectral interference.

A new and possibly useful contribution to the LIBS community is the use of PARAFAC to identify these interferences and removing them. In addition, the samples used in this study are several fragments from a PCB, a complex and heterogeneous matrix, that has more than 20 elements. The focus is on the base and noble elements, such as Al, Cu, Ag and Au. All of them presented some interference in the emission lines, making the application of PARAFAC in the LIBS spectra an interesting test of the ability to mathematically filter the interference signal.

3.1 PARAFAC model for Cu profile characterization

The PARAFAC model was calculated for the data using only Cu emission lines (1210 samples × 17 variables × 10 pulses) and it is shown in Fig. 4. Fig. 4a shows the spectral range chosen for Cu. In the figure, it is possible to observe the great variability among the samples and the presence of interference that can jeopardize the analysis.

The results of a PARAFAC model are given in three modes. The first mode is for the samples, and the parameters represent the relative concentrations found with the model for each component. Mode 2 is for the variables: emission lines for Cu, and mode 3 is related to the 10 pulses analyzed (depth). Fig. 4b and c show the results for modes 2 and 3, respectively.

A model with 3 components explained 88% of the variance and had a core consistency around 62%. The core consistency (CORCONDIA) is used to verify the appropriate number of

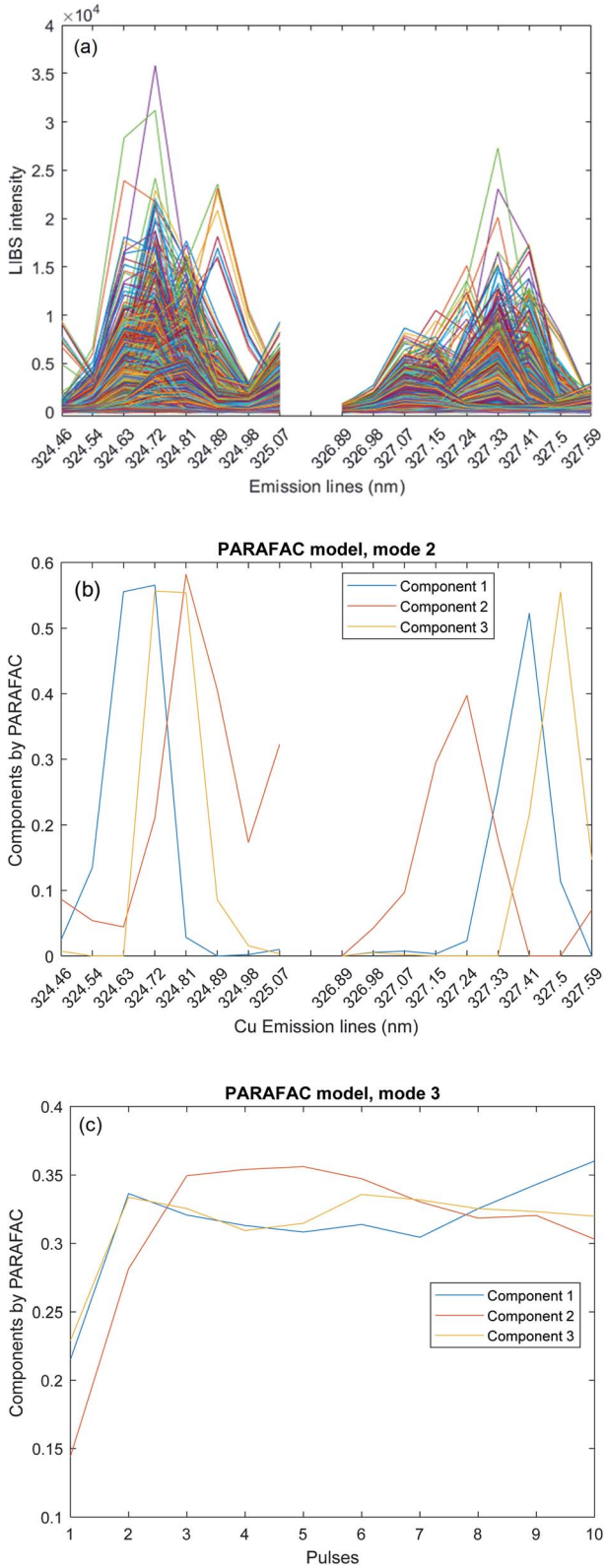

Fig. 4 PARAFAC model for Cu. (a) Spectral range for Cu; (b) mode 2 (emission lines) of the PARAFAC model; (c) mode 3 (pulses) of the PARAFAC model.

components and can be understood as the percentage of trilinear variation in the model space. We took the highest number of PARAFAC components that presented a sufficiently high core consistency (>50%).[34]

Another characteristic of PARAFAC is the possibility to apply constraints, which is helpful to interpret or for stability of the solution. Using constraints, the fit of the model is lower than that of the unconstrained model, but on the other hand, the constrained model can be more realistic. The most common constraints are non-negativity, unimodality and orthogonality. In this study, non-negativity was used for the three modes. This constraint is used to avoid negative spectra that are not in accordance with the expected nature of the LIBS data.[31,35]

As can be observed in Fig. 4b, there are 3 components describing the data, namely the components 1 (blue line) and 3 (yellow line) both of which represent the emission lines for Cu. The spectrometer used is a CCD with 12 288 pixels ranging from 186 to 1042 nm. The resolution changes from one channel to another. The resolution in the spectrometer channel where the Cu emission lines (324.75 and 327.39 nm) are present is around 0.09 nm. Therefore, both peaks appear in the following intervals: 324.72 and 324.81 nm (324.75 nm), and 327.33 and 327.41 nm (327.39 nm). There is not a pixel exactly at 324.75 or 327.39 nm. On the other hand, the component 2 (red line) can be an interference of the Ti ionic emission lines: II 324.86 and II 327.16 nm. The index "II" means that these lines are ionic emission lines.

Other useful information is observed in mode 3 (Fig. 4c), where it is possible to visualize a difference between pulse 1 and the others (from 2 to 10). According to this, Cu is more present in the bulk of the samples, even for the component 2 (interference) that present the same behavior of the target element in the depth.

In certain cases, the so-called split-half analysis[15] was used to further ascertain the number of components. This approach splits the data into two sets and then calculate PARAFAC models for both. If the number of components is chosen correctly, both models will give the same result due to the uniqueness of the PARAFAC model.[13] This strategy was performed and the similarity of both models was 89%.

With the model results, the relative concentrations (scores, mode 1) of components 1 (T1) and 3 (T3) (component 2 is related to interferences) were summed because they represent the same element with difference in the emission line position among the samples. In order to verify the distribution of Cu in the board, the final relative concentration (sum of T1 and T3) was used to construct images. Fig. 5a shows one example for fragment 61, where the yellow squares represent locations with higher amount of Cu than the blue parts. This is a good approach to observe where the element is predominantly located.

This relative concentration can also be used to estimate the real concentration using linear regression with some known values of concentration. Reference values can be obtained, for instance, using inductively coupled plasma optical emission spectrometry (ICP OES) after acid mineralization of samples. But in the case of the present study, it was not possible to obtain good agreement between the LIBS and ICP OES measurement

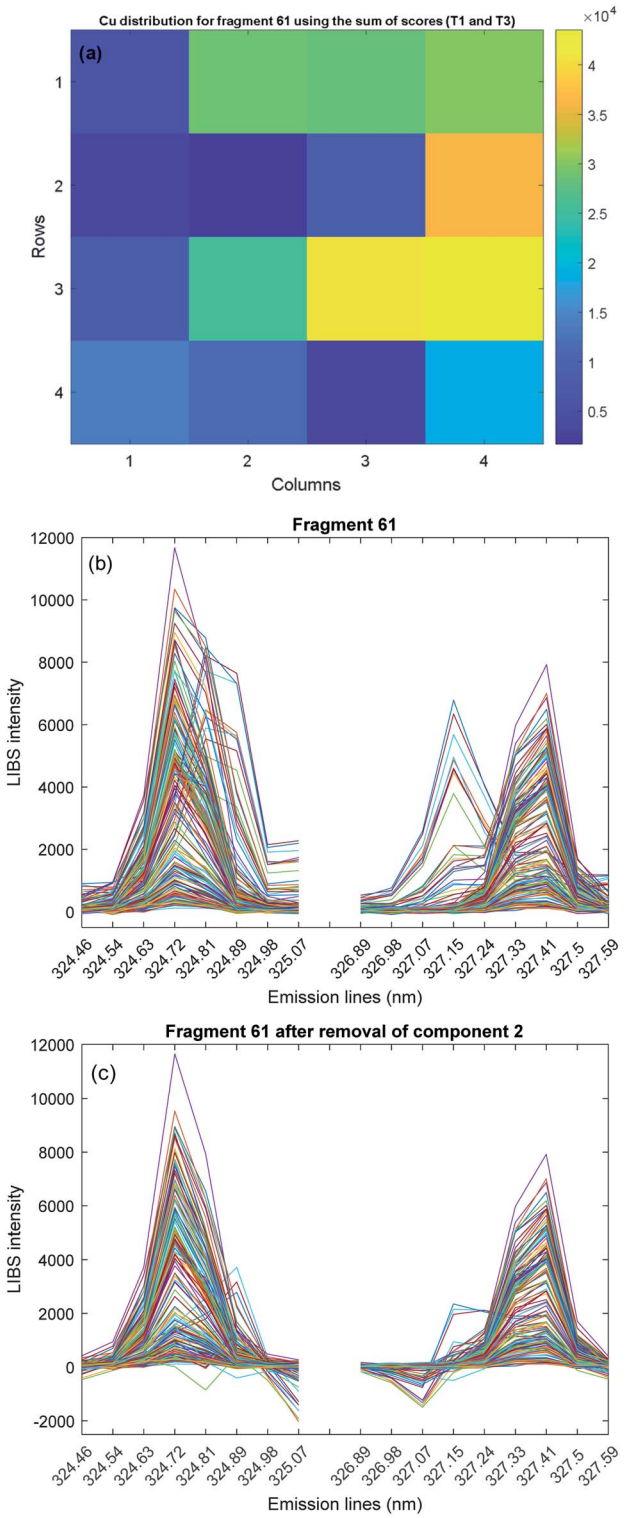

Fig. 5 Example for fragment 61. (a) Cu distribution in this fragment using the relative concentrations (sum of T1 and T3); (b) raw data; (c) spectral range after removal of component 2.

due to sampling and heterogeneity problems. While for LIBS we have 160 spectra for each fragment, for ICP OES there is one reference value per fragment. The ideal situation would be to obtain reference results for each laser pulse.

We can use the PARAFAC model to minimize the interfering signal by subtracting the interference component from the raw data. The second component was extracted using the outer product, followed by its subtraction from the initial data set, showing the applicability of PARAFAC to handle interference problems. This can be seen in Fig. 5b and c, where fragment 61 is presented using the initial data set and the same data after removal of component 2, respectively. After the interference removal it is possible to visualize a more selective spectrum.

A positive aspect observed using PARAFAC was the Ti interference at position 324.81 nm. In this case, Ti (the interferent) or Cu can be detected, but using PARAFAC it was possible to observe two different situations:

(1) Component 3 (Fig. 4b) is related to both Cu emission lines: maximum in 324.81 and 327.41 nm.

(2) Component 2 (Fig. 4b) is related to Ti emission lines: maximum in 324.81 and 327.15 nm.

This is a very positive aspect which is not possible using visual inspection or other chemometric techniques.

3.2 PARAFAC model for Al profile characterization

Another example of the applicability of PARAFAC in LIBS data was Al. In this case a spectral range with two emission lines was selected and 17 variables were organized. The results are shown in Fig. 6. For several spectra, the presence of an interferent in the second emission line (396.15 nm) is observed. A PARAFAC model with 3 components was appropriate. Fig. 6a shows mode 2 with an identified interferent in the component 3, and Fig. 6b shows mode 3.

The components 1 and 2 are very similar in mode 2 (Fig. 6a), but it is possible to observe a huge difference in the pulses (Fig. 6b, mode 3). Component 1 has a high amount of Al for pulse 1, which decreases as the depth increases until it reaches pulse 10. On the other hand, mode 3 is very similar for components 2 and 3 (interference). This interference can be Ti I 396.28 nm or Fe I 396.31 nm.

Fig. 6c shows raw data for fragment 14 with high intensity for Al in pulse 1, decreasing the intensity for pulses 5 and 10, where it is possible to observe the interference in the 396.15 nm emission line. This behavior is observed for all the samples, proving the presence of Al in the pulse 1. Therefore, component 1 refers to Al due to the presence of this element in pulse 1, as mentioned before. It means that Al is more concentrated in the surface of the board (pulse 1). This is another advantage of using multi-way data and tools that model this type of information, making it possible to visualize variations in the data using different modes.

To visualize the Al distribution in the board, images were obtained for the relative concentration of the component 1. Fig. 7a shows the fragment 14, for instance, where the yellow points are related to high amounts of Al. Besides that, the component 3 was extracted using the outer product, followed by its subtraction from the raw data set. Fig. 7b and c show the example for fragment 14, with the initial data set and after removal of component 3, respectively.

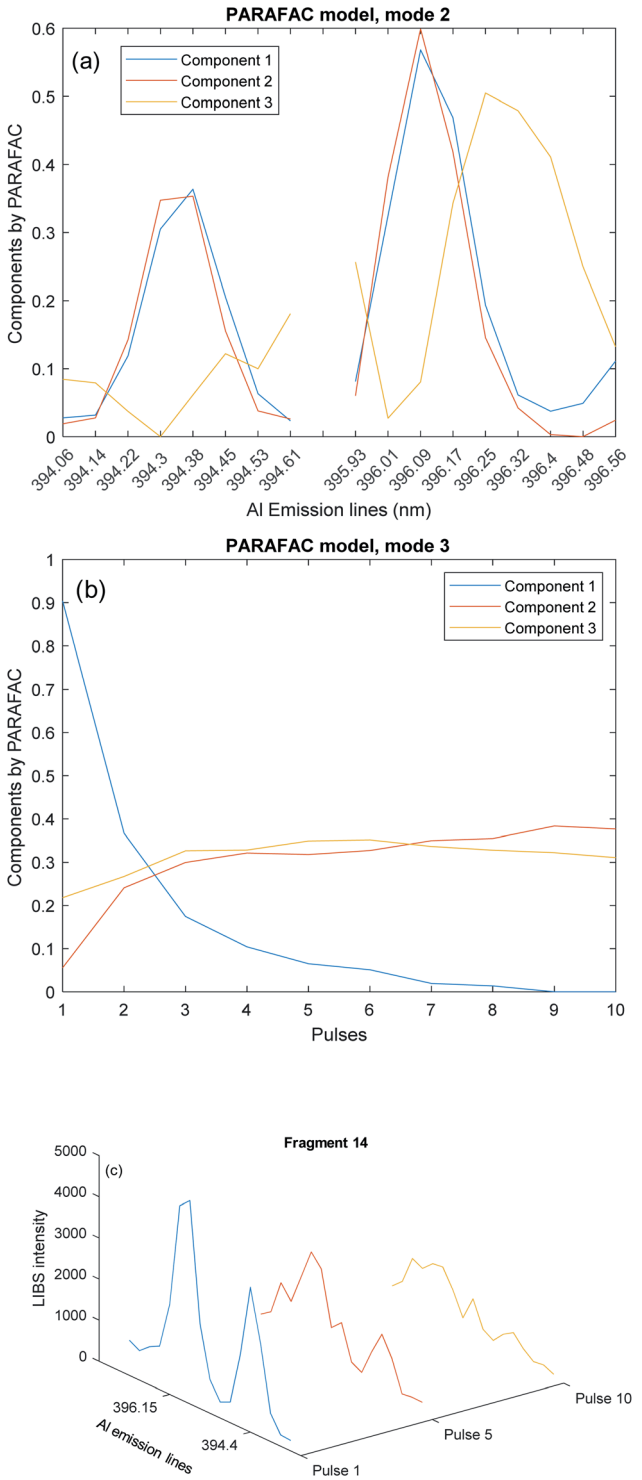

Fig. 6 PARAFAC model for Al. (a) PARAFAC model with 3 components, mode 2; (b) mode 3 (pulses) of the PARAFAC model with 3 components; (c) raw data for fragment 14 with pulses 1, 5 and 10.

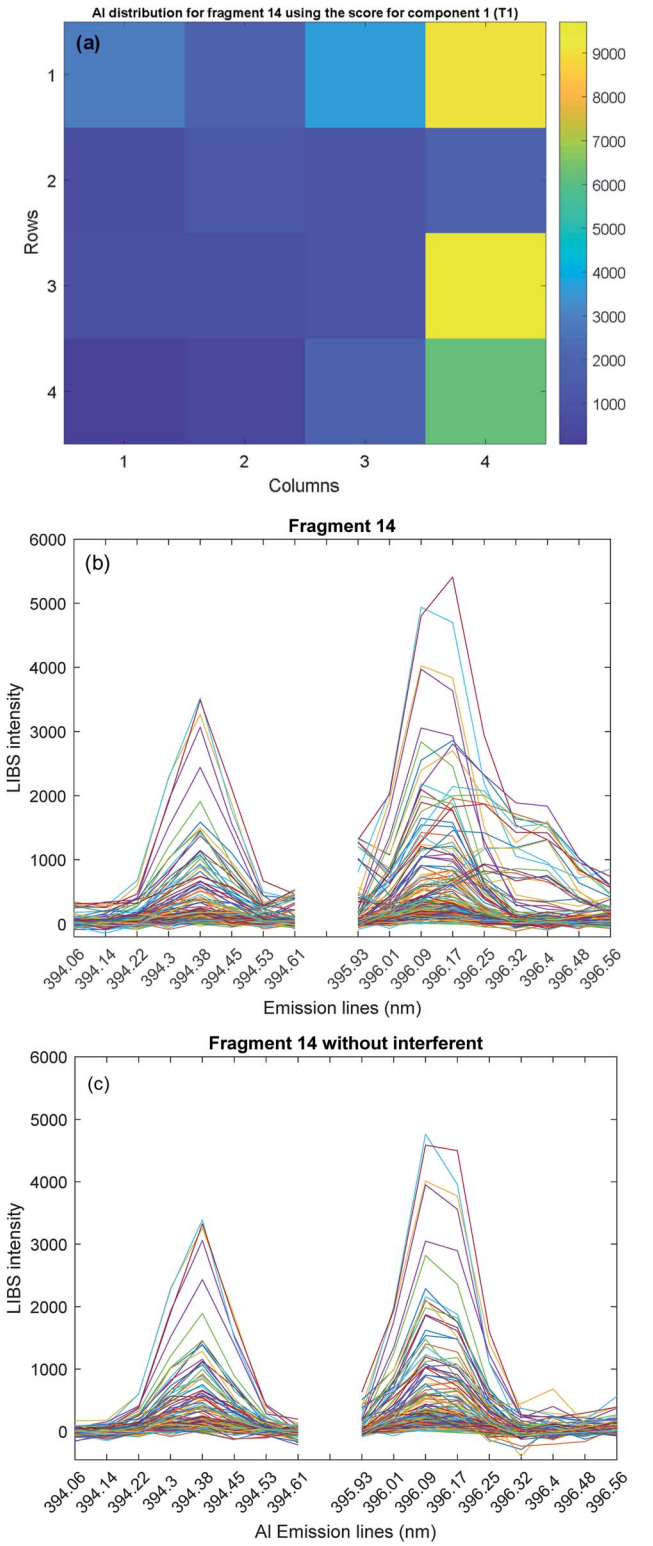

Fig. 7 Example for fragment 14. (a) Al distribution in this fragment using the relative concentration of T1; (b) raw data; (c) spectral range after removal of component 3.

3.3 Noble elements: PARAFAC and classification models

In this study, Au and Ag were investigated. For each element, one spectral range was selected and the baseline correction was made using the Automatic Whittaker Filter. Fig. 8a and d show the spectral range chosen for Au and Ag, respectively, and it is possible observe the complexity of these data, mainly due to the low concentrations that these elements have on the PCB.[36,37]

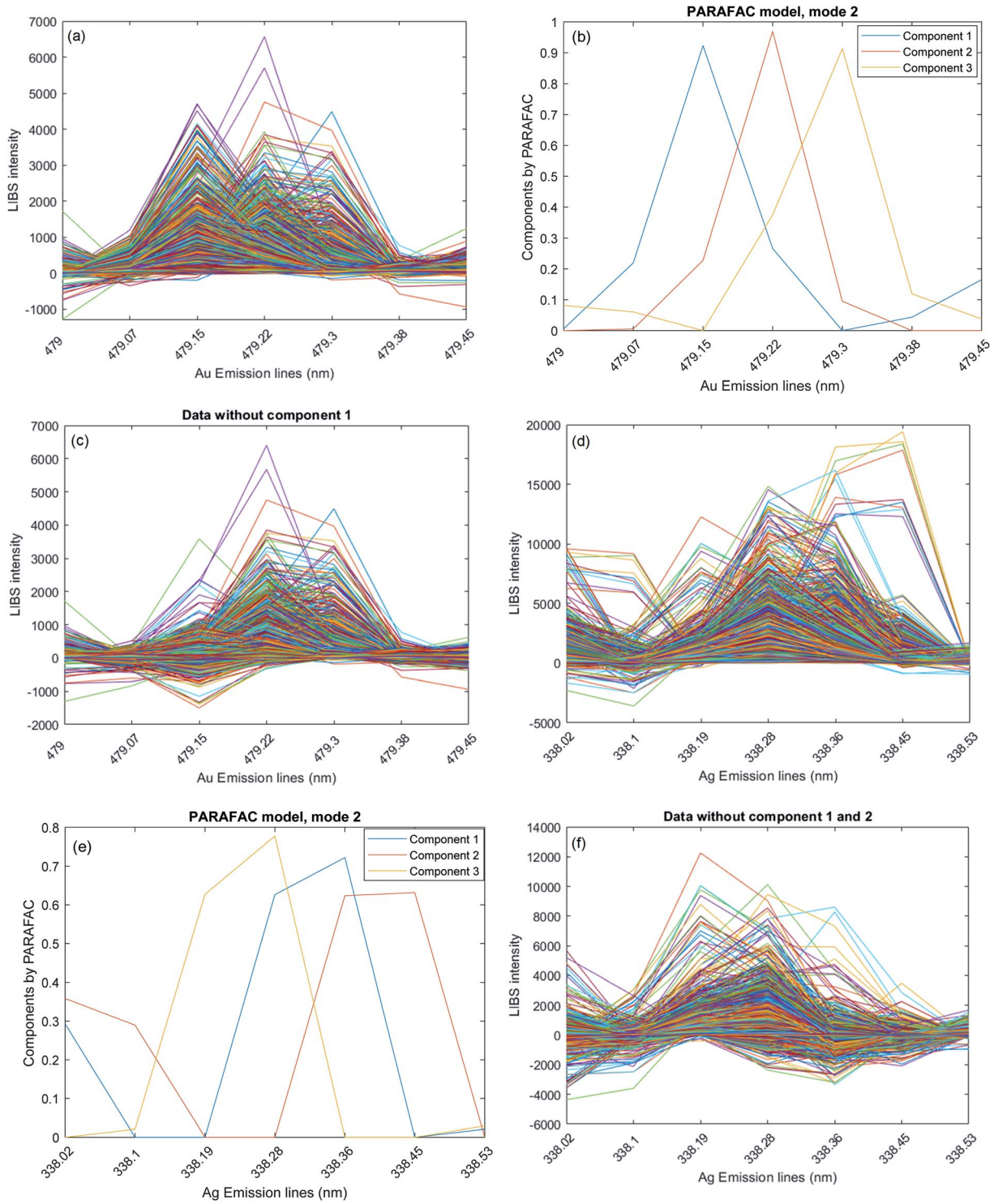

Fig. 8 PARAFAC model for Au and Ag. (a) Raw data for Au; (b) PARAFAC model for Au, mode 2 (emission lines); (c) spectral range for Au after removal of component 1; (d) raw data for Ag; (e) PARAFAC model for Ag, mode 2 (emission lines); (f) spectral range for Ag after removal of components 1 and 2.

PARAFAC models were calculated for both elements and the results can be seen in Fig. 8b and e, for Au and Ag, respectively.

For Au, 3 components were found with the PARAFAC model (Fig. 8b), with components 2 (red line) and 3 (yellow line) being the Au. The emission line of Au is 479.25 nm, but there is not a pixel exactly at this point, so the peak can appear at 479.22 (component 2) or 479.3 nm (component 3). Explained variance of 86% and CORCONDIA of 79% were obtained. In addition, the validation of the model was made using the split-half analysis with a similarity of 90% between both data sets. For Ag, three

Table 1 Figures of merit of the classification models for Au and Ag

		Results for the raw data							Results for the data after removal of interference						
		Class/no. of samples	TPR	TNR	ER	NER	Accuracy	AUC	Class/no. of samples	TPR	TNR	ER	NER	Accuracy	AUC
Au	Calibration	0/25[a]	1.00	0.92	0.04	0.96	0.96	0.99	0/27[a]	1.00	1.00	0	1.00	1.00	1.000
		1/26[b]	0.92	1.00					1/24[b]	1.00	1.00				
	Cross-validation	0/25	0.92	0.85	0.12	0.88	0.88	0.95	0/27	0.96	0.92	0.06	0.94	0.94	0.993
		1/26	0.85	0.92					1/24	0.92	0.96				
	Validation	0/16	0.94	1.00	0.03	0.97	0.97	0.98	0/14	1.00	0.92	0.04	0.96	0.96	0.994
		1/10	1.00	0.94					1/12	0.92	1.00				
Ag	Calibration	0/12[a]	1.00	0.90	0.05	0.95	0.92	0.97	0/18[a]	0.94	0.97	0.04	0.96	0.96	0.994
		1/39[b]	0.90	1.00					1/33[b]	0.97	0.94				
	Cross-validation	0/12	1.00	0.87	0.06	0.94	0.90	0.93	0/18	0.94	0.97	0.04	0.96	0.96	0.981
		1/39	0.87	1.00					1/33	0.97	0.94				
	Validation	0/14	1.00	0.83	0.08	0.92	0.92	0.98	0/8	1.00	0.94	0.03	0.97	0.96	0.993
		1/12	0.83	1.00					1/18	0.94	1.00				

[a] Without Au or Ag. [b] With Au or Ag.

components were also observed with the PARAFAC model (Fig. 8e) with variance of 90% and CORCONDIA of 68%. Using split-half analysis, the validation was performed and 60% of similarity was found between both data sets, which may be justified due to complexity of the spectral range chosen (Fig. 8d). In this case, the component 3 (yellow line) is the element of interest(Ag) and it is exactly at pixel 338.28 nm. In addition, the mode 3 (pulses analysis) of the models shows the presence of these elements at depths.

For Au and Ag, 1 (the first one) and 2 (the first and the second) components can be excluded from the raw data set, respectively. Fig. 8c is the spectral range for Au after removal of component 1, allowing us to observe a more resolved spectral range. And Fig. 8f is the spectral range for Ag after removal of components 1 and 2.

These new data with minimizing the signal of the interference were used to apply classification models using PLSDA to classify whether the sample contains the noble elements or not. The 5th and 6th pulses were selected for Au and Ag, respectively. All procedures adopted were mentioned in the section "2.4 Classification models for noble elements' data inspection". In order to compare the performance of the models, PLSDA was calculated for the raw data from Au and Ag. One latent variable was selected for the data after removal of interference, but for the raw data, two latent variables were necessary for both elements. All the figures of merit are presented in Table 1.

Table 1 shows the sensitivity (TPR) and specificity (TNR) for both classes, besides the ER, NER, accuracy and AUC for Au and Ag. Good results were observed with accuracy ranging from 0.94 to 1.00 and the error rate ranging from 0 to 0.06 for those after removal of interference. On the other hand, for the raw data, accuracy ranging from 0.88 to 0.97 and the error rate ranging from 0.03 to 0.12 were observed. Therefore, the possibility to remove the interference improved the results for the classification of the samples. This approach can be very useful for the recycling process using the PARAFAC to remove interference and then calculate classification models.

4. Conclusions

In this study, characterization of base and noble elements on a PCB was proposed using PARAFAC to model the data. This approach is useful for handling spectral interference from emission lines by extracting them from the data or using the interest scores (from the component of interest) for additional calculations. In addition, multi-way analysis aids to visualize the variations in different modes, for instance, the investigation of depths and the spectral range. Another positive aspect is the use of images with scores, which makes possible to visualize where the element is more concentrated. For noble elements, PLSDA models were built with the spectra after removal of interferents and good figures of merit were acquired. Therefore, the use of LIBS spectra and the PARAFAC model was a good approach with several advantages for characterization of analytes and contribution to urban mining.

Conflicts of interest

There are no conflicts to declare.

Acknowledgements

This study was supported by the São Paulo Research Foundation (FAPESP, grants 2012/01769-3, 2012/50827-6, 2014/22408-4, 2016/01513-0, 2016/17221-8 and 2018/17753-5) and Conselho Nacional de Desenvolvimento Científico e Tecnológico (CNPq, 401074/2014-5 and 305637/2015-0). This study was financed in part by the Coordenação de Aperfeiçoamento de Pessoal de Nível Superior – Brasil (CAPES) – Finance Code 001.

References

1 C. P. Baldé, V. Forti, V. Gray, R. Kuehr and P. Stegmann, *The Global E-waste Monitor – 2017, United Nations University (UNU)*, International Telecommunication Union (ITU) &

International Solid Waste Association (ISWA), Bonn, Geneva, Vienna, 2017.
2 S. Zhang, Y. Ding, B. Liu and C.-C. Chang, *Waste Manag.*, 2017, **65**, 113–127.
3 D. F. Andrade, J. P. Romanelli and E. R. Pereira-Filho, *Environ. Sci. Pollut. Res.*, 2019, **26**, 17135–17151.
4 D. F. Andrade, F. M. Fortunato and E. R. Pereira-Filho, *Anal. Chim. Acta*, 2019, **1061**, 42–49.
5 J. P. Castro, D. V. Babos and E. R. Pereira-Filho, *Talanta*, 2020, **208**, 120443.
6 R. C. Machado, D. F. Andrade, D. V. Babos, J. P. Castro, V. C. Costa, M. A. Sperança, J. A. Garcia, R. R. Gamela and E. R. Pereira-Filho, *J. Anal. At. Spectrom.*, 2020, **35**, 54–77.
7 J. P. Castro and E. R. Pereira-Filho, *Talanta*, 2018, **189**, 205–210.
8 V. C. Costa, J. P. Castro, D. F. Andrade, D. V. Babos, J. A. Garcia, M. A. Sperança, T. A. Catelani and E. R. Pereira-Filho, *TrAC, Trends Anal. Chem.*, 2018, **108**, 65–73.
9 D. W. Hahn and N. Omenetto, *Appl. Spectrosc.*, 2012, **66**, 347–419.
10 V. C. Costa, A. S. Augusto, J. P. Castro, R. C. Machado, D. F. Andrade, D. V. Babos, M. A. Sperança, R. R. Gamela and E. R. Pereira-Filho, *Quim. Nova*, 2019, **42**, 527–545.
11 C. Pasquini, J. Cortez, L. M. C. Silva and F. B. Gonzaga, *J. Braz. Chem. Soc.*, 2007, **18**, 463–512.
12 S. Legnaioli, G. Lorenzetti, L. Pardini, V. Palleschi, D. M. D. Pace, F. A. Garcia, R. Grassi, F. Sorrentino, G. Carelli, M. Francesconi, F. Francesconi and R. Borgogni, *Spectrochim. Acta, Part B*, 2012, **71–72**, 123–126.
13 J. Guezenoc, A. Gallet-Budynek and B. Bousquet, *Spectrochim. Acta, Part B*, 2019, **160**, 105688.
14 J. El Haddad, L. Canioni and B. Bousquet, *Spectrochim. Acta, Part B*, 2014, **101**, 171–182.
15 R. Bro, *Chemom. Intell. Lab. Syst.*, 1997, **38**, 149–171.
16 R. Bro, *Anal. Chem.*, 2006, **36**, 279–293.
17 R. Bro, *Chemom. Intell. Lab. Syst.*, 1999, **46**, 133–147.
18 C. M. Andersen and R. Bro, *J. Chemom.*, 2003, **17**, 200–215.
19 L. Lenhardt, R. Bro, I. Zekovic, T. Dramicanin and M. D. Dramicanin, *Food Chem.*, 2015, **175**, 284–291.
20 J. C. G. E. da Silva, J. M. M. Leitão, F. S. Costa and J. L. A. Ribeiro, *Anal. Chim. Acta*, 2002, **453**, 105–115.
21 R. M. Callejón, J. M. Amigo, E. Pairo, S. Garmón, J. A. Ocaña and M. L. Morales, *Talanta*, 2012, **88**, 456–462.
22 H. Idborg, P.-O. Edlund and S. P. Jacobsson, *Rapid Commun. Mass Spectrom.*, 2004, **18**, 944–954.
23 D. Bylund, R. Danielsson, G. Malmquist and K. E. Markides, *J. Chromatogr. A*, 2002, **961**, 237–244.
24 L. Rubio, L. Valverde-Som, L. A. Sarabia and M. C. Ortiz, *J. Chromatogr. A*, 2019, **1589**, 18–29.
25 F. A. L. Ribeiro, F. F. Rosário, M. C. M. Bezerra, A. L. M. Bastos, V. L. A. Melo and R. J. Poppi, *Chemom. Intell. Lab. Syst.*, 2012, **115**, 18–24.
26 C. A. Stedmon and R. Bro, *Limnol. Oceanogr.: Methods*, 2008, **6**, 572–579.
27 M. B. B. Guerra, P. F. Rosa, C. E. G. R. Schaefer, R. F. M. Michel, I. C. Almeida and E. R. Pereira-Filho, *J. Braz. Chem. Soc.*, 2012, **23**, 1388–1394.
28 L. Rubio, S. Sanllorente, L. A. Sarabia and M. C. Ortiz, *Food Chem.*, 2019, **290**, 178–186.
29 M. Mørup, L. K. Hansen, C. S. Herrmann, J. Parnas and S. M. Arnfred, *NeuroImage*, 2006, **29**, 938–947.
30 R. A. Harshman and M. E. Lundy, *Comput. Stat. Data Anal.*, 1994, **18**, 39–72.
31 R. Bro, Doctoral dissertation, University of Amsterdam, 1998.
32 B. M. Wise, N. B. Gallagher, R. Bro, J. M. Shaver, W. Windig and R. S. Koch, *PLSToolbox 8.7.1*, Eigenvector Research Inc., Wenatchee, WA, USA, 2019.
33 D. Ballabio, F. Grisoni and R. Todeschini, *Chemom. Intell. Lab. Syst.*, 2018, **174**, 33–44.
34 R. Bro and H. A. L. Kiers, *J. Chemom.*, 2003, **17**, 274–286.
35 C. A. Stedmon, S. Markager and R. Bro, *Mar. Chem.*, 2003, **82**, 239–254.
36 D. F. Andrade, R. C. Machado, M. A. Bacchi and E. R. Pereira-Filho, *J. Anal. At. Spectrom.*, 2019, **34**, 2394–2401.
37 D. F. Andrade, R. C. Machado and E. R. Pereira-Filho, *J. Anal. At. Spectrom.*, 2019, **34**, 2402–2410.

Chapter 5. Conclusion

5. Conclusion

In this thesis, it was possible to develop a reference method using ICP OES for the high-performance magnets containing all the steps for sample preparation until the ICP OES analysis. A simple method was used: diluted acid (HNO_3) and digestor block minimizing the environmental impact from strong acids concentration. For the PCB samples, the preparation was minimized because none gridding step was made, so the sample was digested with aqua regia using microwave system followed by ICP OES determination. The differential was the exploratory analysis with different plots: score and loadings; correlation plot and individual distribution of the elements plot. With this approach, it was possible to understand and visualize the data, contributing with urban mining.

On the other hand, the best way to prepare a sample is not to prepare it, but to analyze it directly. Therefore, LIBS technique was used to characterize the high-performance magnets to determine rare earth elements (Dy, Gd, Pr, Sm, Tb and Nd) and the base elements (B and Fe). Five calibration strategies were tested: MLR and PLS as multivariate strategies and, MEC, OP GSA and TP CT (proposed in this study) as univariate strategies. For the multivariate calibration, the models are calculated in the presence of concomitants but do not correct matrix effect and, the calibration/validation dataset must have the same linear range. For univariate calibration, MEC and OP GSA are efficient matrix-matching methods but the choice of blank and standard can be a difficult task, besides care with the homogenization of the mixtures. In addition, with MEC is possible the removal of emission lines that present spectral interference. The TP CT seems to be more robust with low RSD values, the sample preparation and data treatment are simpler than the other, but the choice of standard is critical.

The three univariate calibration strategies (MEC, OP GSA and TP CT) were also applied for the Nd determination using WD XRF. As mentioned before, each strategy can be useful for a given situation. In general, all the models presented good results, where the TP CT seems to be more robust. In addition, the advantage to determine Nd with WD XRF is the use of only one crystal including five electronic transition where the analysis is faster.

And finally, the chapter 4 was the first paper about LIBS and PARAFAC in the literature. With this combination, it was possible handling spectral interference extracting them from the initial data or use the scores of the interest component

for additional calculations (calibration or classification). After the removal of interference, partial least square discriminant analysis (PLS DA) was performed for noble elements and the figures of merit were better than the models with the raw data. The scores are also useful to build images where it was possible visualize the distribution of the elements on the PCB. In addition, the multi-way analysis is an attractive field to visualize the variations in different modes, as example, samples, emission lines and depth. Also, in this case, with the PARAFAC two different situations with Cu was observed: two emission lines for Cu were investigated and the components given by PARAFAC showed the interference and interest emission line at the same position in the first emission line, but the PARAFAC managed to differentiate both through the second emission line (where the interferent was not present at the same position). In a normal approach, this would not be possible.

Figure 5 shows a conclusion overview by a chart. With all these approaches, it was possible to propose quick and simple methods to facilitate and optimize the recycling process.

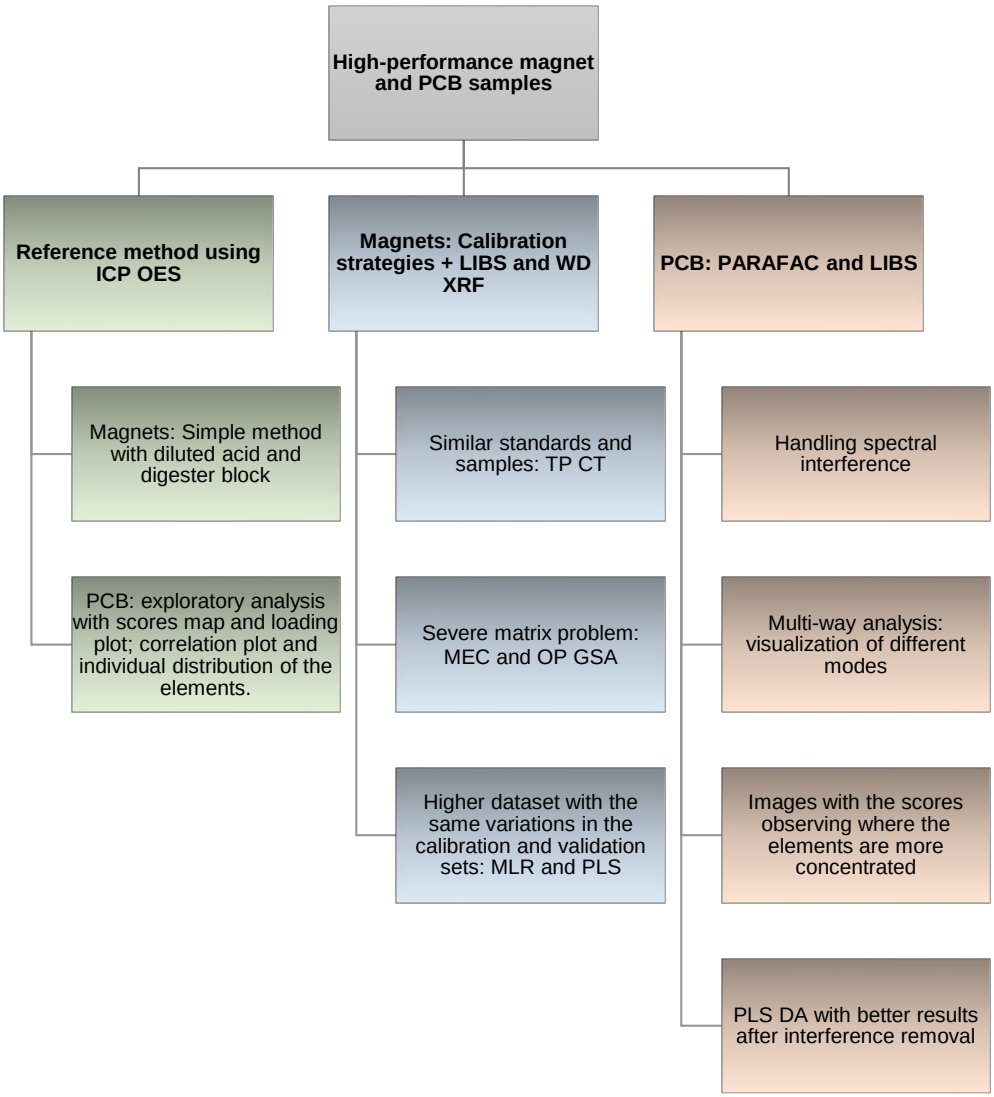

Figure 5. Conclusion overview.

6. References

[1] V. Forti, C.P. Baldé, R. Kuehr, G. Bel, The Global E-waste Monitor 2020: Quantities, Flows, and the Circular Economy Potential, 2020.

[2] D.F. Andrade, J.P. Romanelli, E.R. Pereira-Filho, Past and emerging topics related to electronic waste management: top countries, trends, and perspectives, Environ. Sci. Pollut. Res. 26 (2019) 17135–17151. https://doi.org/10.1007/s11356-019-05089-y.

[3] V.C. Costa, J.P. Castro, D.F. Andrade, D. Victor Babos, J.A. Garcia, M.A. Sperança, T.A. Catelani, E.R. Pereira-Filho, Laser-induced breakdown spectroscopy (LIBS) applications in the chemical analysis of waste electrical and electronic equipment (WEEE), TrAC - Trends Anal. Chem. 108 (2018) 65–73. https://doi.org/10.1016/j.trac.2018.08.003.

[4] K. Lundgren, The global impact of e-waste: Addressing the challenge, 2012.

[5] B. Hale, L. McAllister, From Treasure to Trash: The Lingering Value of Technological Artifacts, Sci. Eng. Ethics. 26 (2020) 619–640. https://doi.org/10.1007/s11948-019-00107-1.

[6] LEI Nº 12.305, Política Nacional de Resíduos Sólidos, (2010) 1–18.

[7] R.G. Souza, E-waste situation and current practices in Brazil, INC, 2019. https://doi.org/10.1016/B978-0-12-817030-4.00009-7.

[8] R.A. Patil, S. Ramakrishna, A comprehensive analysis of e-waste legislation worldwide, Environ. Sci. Pollut. Res. 27 (2020) 14412–14431. https://doi.org/10.1007/s11356-020-07992-1.

[9] R.I. Moletsane, C. Venter, Electronic Waste and its Negative Impact on Human Health and the Environment, 2018 Int. Conf. Adv. Big Data, Comput. Data Commun. Syst. IcABCD 2018. (2018). https://doi.org/10.1109/ICABCD.2018.8465473.

[10] Tecmundo, Como funciona um disco rígido?, (2010). https://www.tecmundo.com.br/aumentar-desempenho/3469-como-funciona-um-disco-rigido-.htm.

[11] N.E. Menad, A. Seron, N. Maat, Process Recovery of Nd-Fe-B Permanent Magnets from Hard Disc Drives, J. Geogr. Nat. Disasters. s6 (2017). https://doi.org/10.4172/2167-0587.s6-008.

[12] S. Zhang, Y. Ding, B. Liu, C. chi Chang, Supply and demand of some

critical metals and present status of their recycling in WEEE, Waste Manag. 65 (2017) 113–127. https://doi.org/10.1016/j.wasman.2017.04.003.

[13] European Comission: Enterprise and Industry, Critical raw materials for the EU, Report of the Ad-hoc Working Group on defining critical raw materials, Eucom. (2010) 1–84.

[14] N. Mackenzie, Neodímio, o valioso mineral raro escondido dentro de computadores, (2020). https://www.bbc.com/portuguese/geral-53083835.

[15] L.H. Yamane, V.T. de Moraes, D.C.R. Espinosa, J.A.S. Tenório, Recycling of WEEE: Characterization of spent printed circuit boards from mobile phones and computers, Waste Manag. 31 (2011) 2553–2558. https://doi.org/10.1016/j.wasman.2011.07.006.

[16] R. Cayumil, M. Ikram-Ul-Haq, R. Khanna, R. Saini, P.S. Mukherjee, B.K. Mishra, V. Sahajwalla, High temperature investigations on optimising the recovery of copper from waste printed circuit boards, Waste Manag. 73 (2018) 556–565. https://doi.org/10.1016/j.wasman.2017.01.001.

[17] R. Sanapala, Characterization of FR-4 Printed Circuit Board Laminates Before and After Exposure to Lead-free Soldering Conditions, (2018). Thesis submitted to the Faculty of the Graduate School of the University of Maryland, College Park.

[18] A. Varenne, Cooperation increases between analytical sciences and recycling, TrAC - Trends Anal. Chem. 48 (2013) 22–29. https://doi.org/10.1016/j.trac.2013.04.007.

[19] V.C. Costa, F.W.B. Aquino, C.M. Paranhos, E.R. Pereira-Filho, Identification and classification of polymer e-waste using laser-induced breakdown spectroscopy (LIBS) and chemometric tools, Polym. Test. 59 (2017) 390–395. https://doi.org/10.1016/j.polymertesting.2017.02.017.

[20] B. Sprecher, Y. Xiao, A. Walton, J. Speight, R. Harris, R. Kleijn, G. Visser, G.J. Kramer, Life cycle inventory of the production of rare earths and the subsequent production of NdFeB rare earth permanent magnets, Environ. Sci. Technol. 48 (2014) 3951–3958. https://doi.org/10.1021/es404596q.

[21] A. Kumari, M.K. Jha, D.D. Pathak, An innovative environmental process for the treatment of scrap Nd-Fe-B magnets, J. Environ. Manage. 273 (2020) 111063. https://doi.org/10.1016/j.jenvman.2020.111063.

[22] A. Marra, A. Cesaro, V. Belgiorno, Separation efficiency of valuable and

critical metals in WEEE mechanical treatments, J. Clean. Prod. 186 (2018) 490–498. https://doi.org/10.1016/j.jclepro.2018.03.112.

[23] D.D. München, A.M. Bernardes, H.M. Veit, Evaluation of Neodymium and Praseodymium Leaching Efficiency from Post-consumer NdFeB Magnets, J. Sustain. Metall. 4 (2018) 288–294. https://doi.org/10.1007/s40831-018-0180-6.

[24] M. Matsumiya, K. Ishioka, T. Yamada, M. Ishii, S. Kawakami, Recovery of rare earth metals from voice coil motors using bis(trifluoromethylsulfonyl)amide melts by wet separation and electrodeposition, Int. J. Miner. Process. 126 (2014) 62–69. https://doi.org/10.1016/j.minpro.2013.11.010.

[25] M. Ueberschaar, V.S. Rotter, Enabling the recycling of rare earth elements through product design and trend analyses of hard disk drives, J. Mater. Cycles Waste Manag. 17 (2015) 266–281. https://doi.org/10.1007/s10163-014-0347-6.

[26] T. Vander Hoogerstraete, B. Blanpain, T. Van Gerven, K. Binnemans, From NdFeB magnets towards the rare-earth oxides: A recycling process consuming only oxalic acid, RSC Adv. 4 (2014) 64099–64111. https://doi.org/10.1039/c4ra13787f.

[27] D. Dupont, K. Binnemans, Recycling of rare earths from NdFeB magnets using a combined leaching/extraction system based on the acidity and thermomorphism of the ionic liquid [Hbet][Tf2N], Green Chem. 17 (2015) 2150–2163. https://doi.org/10.1039/c5gc00155b.

[28] D.D. München, H.M. Veit, Neodymium as the main feature of permanent magnets from hard disk drives (HDDs), Waste Manag. 61 (2017) 372–376. https://doi.org/10.1016/j.wasman.2017.01.032.

[29] G. Reisdörfer, D. Bertuol, E.H. Tanabe, Recovery of neodymium from the magnets of hard disk drives using organic acids, Miner. Eng. 143 (2019) 105938. https://doi.org/10.1016/j.mineng.2019.105938.

[30] A. Beylot, N.E. Ménad, A. Seron, M. Delain, A. Bizouard, Y. Ménard, J. Villeneuve, Economic assessment and carbon footprint of recycling rare earths from magnets: Evaluation at lab scale paving the way toward industrialization, J. Ind. Ecol. 24 (2020) 128–137. https://doi.org/10.1111/jiec.12943.

[31] M. Gergoric, A. Barrier, T. Retegan, Recovery of Rare-Earth Elements from Neodymium Magnet Waste Using Glycolic, Maleic, and Ascorbic Acids Followed by Solvent Extraction, J. Sustain. Metall. 5 (2019) 85–96. https://doi.org/10.1007/s40831-018-0200-6.

[32] K. Habib, K. Parajuly, H. Wenzel, Tracking the Flow of Resources in Electronic Waste - The Case of End-of-Life Computer Hard Disk Drives, Environ. Sci. Technol. 49 (2015) 12441–12449. https://doi.org/10.1021/acs.est.5b02264.

[33] A. Walton, H. Yi, N.A. Rowson, J.D. Speight, V.S.J. Mann, R.S. Sheridan, A. Bradshaw, I.R. Harris, A.J. Williams, The use of hydrogen to separate and recycle neodymium-iron-boron-type magnets from electronic waste, J. Clean. Prod. 104 (2015) 236–241. https://doi.org/10.1016/j.jclepro.2015.05.033.

[34] N. Maât, V. Nachbaur, R. Lardé, J. Juraszek, J.M. Le Breton, An Innovative Process Using Only Water and Sodium Chloride for Recovering Rare Earth Elements from Nd-Fe-B Permanent Magnets Found in the Waste of Electrical and Electronic Equipment, ACS Sustain. Chem. Eng. 4 (2016) 6455–6462. https://doi.org/10.1021/acssuschemeng.6b01226.

[35] D.F. Andrade, R.C. Machado, M.A. Bacchi, E.R. Pereira-Filho, Proposition of electronic waste as a reference material-part 1: Sample preparation, characterization and chemometric evaluation, J. Anal. At. Spectrom. 34 (2019) 2394–2401. https://doi.org/10.1039/c9ja00283a.

[36] L. Flandinet, F. Tedjar, V. Ghetta, J. Fouletier, Metals recovering from waste printed circuit boards (WPCBs) using molten salts, J. Hazard. Mater. 213–214 (2012) 485–490. https://doi.org/10.1016/j.jhazmat.2012.02.037.

[37] D.F. Andrade, R.C. Machado, E.R. Pereira-Filho, Proposition of electronic waste as a reference material-part 2: Homogeneity, stability, characterization, and uncertainties, J. Anal. At. Spectrom. 34 (2019) 2402–2410. https://doi.org/10.1039/c9ja00284g.

[38] I. Birloaga, F. Vegliò, Study of multi-step hydrometallurgical methods to extract the valuable content of gold, silver and copper from waste printed circuit boards, J. Environ. Chem. Eng. 4 (2016) 20–29. https://doi.org/10.1016/j.jece.2015.11.021.

[39] A. Jandric, C.D. Tran, P. Beigl, Z. Micuda, S. Salhofer, Exploration of the

material distribution of complex components in waste electrical and electronic equipment, Glob. Nest J. 20 (2018) 725–736. https://doi.org/10.30955/GNJ.002672.

[40] X. Hou, R.S.. Amais, B.T.. Jones, G.L. Donati, Inductively coupled plasma optical emission spectrometry, Anal. Instrum. Handbook, Third Ed. (2004) 57–74. https://doi.org/10.1002/9780470027318.a5110.pub3.

[41] R.C. MacHado, D.F. Andrade, D. V. Babos, J.P. Castro, V.C. Costa, M.A. Sperancą, J.A. Garcia, R.R. Gamela, E.R. Pereira-Filho, Solid sampling: Advantages and challenges for chemical element determination- A critical review, J. Anal. At. Spectrom. 35 (2020) 54–77. https://doi.org/10.1039/c9ja00306a.

[42] C.S. Nomura, C.S. Da Silva, P.V. Oliveira, Análise direta de sólidos por espectrometria de absorção atômica com atomização em forno de grafite: Uma revisão, Quim. Nova. 31 (2008) 104–113. https://doi.org/10.1590/S0100-40422008000100022.

[43] S.C. Jantzi, V. Motto-Ros, F. Trichard, Y. Markushin, N. Melikechi, A. De Giacomo, Sample treatment and preparation for laser-induced breakdown spectroscopy, Spectrochim. Acta - Part B At. Spectrosc. 115 (2016) 52–63. https://doi.org/10.1016/j.sab.2015.11.002.

[44] F.R.P. KRUG, F. J. & ROCHA, Métodos de preparo de amostras para análise elementar, EditSBQ-, São Paulo, 2016.

[45] V.C. Costa, D. V. Babos, J.P. Castro, D.F. Andrade, R.R. Gamela, R.C. MacHado, M.A. Speranca, A.S. Araujo, J.A. Garcia, E.R. Pereira-Filho, Calibration strategies applied to laser-induced breakdown spectroscopy: A critical review of advances and challenges, J. Braz. Chem. Soc. 31 (2020) 2439–2451. https://doi.org/10.21577/0103-5053.20200175.

[46] A. Virgilio, D.A. Gonçalves, T. McSweeney, J.A. Gomes Neto, J.A. Nóbrega, G.L. Donati, Multi-energy calibration applied to atomic spectrometry, Anal. Chim. Acta. 982 (2017) 31–36. https://doi.org/10.1016/j.aca.2017.06.040.

[47] D.V. Babos, A. Virgilio, V.C. Costa, G.L. Donati, E.R. Pereira-Filho, Multi-energy calibration (MEC) applied to laser-induced breakdown spectroscopy (LIBS), J. Anal. At. Spectrom. 33 (2018) 1753–1762. https://doi.org/10.1039/c8ja00109j.

[48] A.A.C. Carvalho, L.A. Cozer, M.S. Luz, L.C. Nunes, F.R.P. Rocha, C.S. Nomura, Multi-energy calibration and sample fusion as alternatives for quantitative analysis of high silicon content samples by laser-induced breakdown spectrometry, J. Anal. At. Spectrom. 34 (2019) 1701–1707. https://doi.org/10.1039/c9ja00149b.

[49] D.F. Andrade, F.M. Fortunato, E.R. Pereira-Filho, Calibration strategies for determination of the In content in discarded liquid crystal displays (LCD) from mobile phones using laser-induced breakdown spectroscopy (LIBS), Anal. Chim. Acta. 1061 (2019) 42–49. https://doi.org/10.1016/j.aca.2019.02.038.

[50] A.S. Augusto, J.P. Castro, M.A. Sperança, E.R. Pereira-Filho, Combination of multi-energy calibration (MEC) and laser-induced breakdown spectroscopy (LIBS) for dietary supplements analysis and determination of Ca, Mg and K, J. Braz. Chem. Soc. 30 (2019) 804–812. https://doi.org/10.21577/0103-5053.20180211.

[51] Felipe M. Fortunato, Tiago A. Catelani, Mario S. Pomares-Alfonso, Edenir R. Pereira-Filho, Application of Multi-energy Calibration for Determination of Chromium and Nickel in Nickeliferous Ores by Laser-induced Breakdown Spectroscopy., Anal. Sci. 35 (2019) 165–168. https://www.jstage.jst.go.jp/article/analsci/35/2/35_18P286/_pdf/-char/en.

[52] D.V. Babos, A.I. Barros, J.A. Nóbrega, E.R. Pereira-Filho, Calibration strategies to overcome matrix effects in laser-induced breakdown spectroscopy: Direct calcium and phosphorus determination in solid mineral supplements, Spectrochim. Acta - Part B At. Spectrosc. 155 (2019) 90–98. https://doi.org/10.1016/j.sab.2019.03.010.

[53] L.C. Nunes, F.R.P. Rocha, F.J. Krug, Slope ratio calibration for analysis of plant leaves by laser-induced breakdown spectroscopy, J. Anal. At. Spectrom. 34 (2019) 2314–2324. https://doi.org/10.1039/c9ja00270g.

[54] R.R. Gamela, V.C. Costa, D.V. Babos, A.S. Araújo, E.R. Pereira-Filho, Direct Determination of Ca, K, and Mg in Cocoa Beans by Laser-Induced Breakdown Spectroscopy (LIBS): Evaluation of Three Univariate Calibration Strategies for Matrix Matching, Food Anal. Methods. 13 (2020) 1017–1026. https://doi.org/10.1007/s12161-020-01722-6.

[55] D.V. Babos, A. Cruz-Conesa, E.R. Pereira-Filho, J.M. Anzano, Direct

determination of Al and Pb in waste printed circuit boards (PCB) by laser-induced breakdown spectroscopy (LIBS): Evaluation of calibration strategies and economic - environmental questions, J. Hazard. Mater. 399 (2020) 122831. https://doi.org/10.1016/j.jhazmat.2020.122831.

[56] V.C. Costa, M.L. de Mello, D.V. Babos, J.P. Castro, E.R. Pereira-Filho, Calibration strategies for determination of Pb content in recycled polypropylene from car batteries using laser-induced breakdown spectroscopy (LIBS), Microchem. J. 159 (2020) 105558. https://doi.org/10.1016/j.microc.2020.105558.

[57] R. Bro, Multivariate calibration: What is in chemometrics for the analytical chemist?, Anal. Chim. Acta. 500 (2003) 185–194. https://doi.org/10.1016/S0003-2670(03)00681-0.

[58] T. Zhang, H. Tang, H. Li, Chemometrics in laser-induced breakdown spectroscopy, J. Chemom. 32 (2018) 1–18. https://doi.org/10.1002/cem.2983.

[59] M.M.C. Ferreira, Quimiometria. Conceitos, Métodos e Aplicações, Editora Unicamp, Campinas, 2015.

[60] M.A. Sperança, D.F. Andrade, J.P. Castro, E.R. Pereira-Filho, Univariate and multivariate calibration strategies in combination with laser-induced breakdown spectroscopy (LIBS) to determine Ti on sunscreen: A different sample preparation procedure, Opt. Laser Technol. 109 (2019) 648–653. https://doi.org/10.1016/j.optlastec.2018.08.056.

[61] J. Wang, M. Shi, P. Zheng, S. Xue, Quantitative Analysis of Lead in Tea Samples by Laser-Induced Breakdown Spectroscopy, J. Appl. Spectrosc. 84 (2017) 188–193. https://doi.org/10.1007/s10812-017-0448-9.

[62] K.K. Ayyalasomayajula, F. Yu-Yueh, J.P. Singh, D.L. McIntyre, J. Jain, Application of laser-induced breakdown spectroscopy for total carbon quantification in soil samples, Appl. Opt. 51 (2012) 149–154. https://doi.org/10.1364/AO.51.00B149.

[63] N. Kumar, A. Bansal, G.S. Sarma, R.K. Rawal, Chemometrics tools used in analytical chemistry: An overview, Talanta. 123 (2014) 186–199. https://doi.org/10.1016/j.talanta.2014.02.003.

[64] V.C. Costa, F.W.B. Aquino, C.M. Paranhos, E.R. Pereira-Filho, Use of laser-induced breakdown spectroscopy for the determination of

polycarbonate (PC) and acrylonitrile-butadiene-styrene (ABS) concentrations in PC/ABS plastics from e-waste, Waste Manag. 70 (2017) 212–221. https://doi.org/10.1016/j.wasman.2017.09.027.

[65] A. Erler, D. Riebe, T. Beitz, H.-G. Lohmannsroben, R. Gebbers, Soil Nutrient Detection for Precision Agriculture Using Handheld Laser-Induced Breakdown Spectroscopy (LIBS) and Multivariate Regression Methods (PLSR, Lasso and GPR), Sensors (Switzerland). 20 (2020) 418. https://doi.org/https://doi.org/10.3390/s20020418.

[66] Y. Lu, H. Guo, T. Shen, W. Wang, Y. He, F. Liu, Quantitative analysis of cadmium and zinc in algae using laser-induced breakdown spectroscopy, Anal. Methods. 11 (2019) 6124–6135. https://doi.org/10.1039/c9ay01681c.

[67] D.V. Babos, V.C. Costa, E.R. Pereira-Filho, Wavelength dispersive X-ray fluorescence (WD-XRF) applied to speciation of sulphur in mineral supplement for cattle: Evaluation of the chemical and matrix effects, Microchem. J. 147 (2019) 628–634. https://doi.org/10.1016/j.microc.2019.03.077.

[68] P. Kikongi, C. Fauteux-Lefebvre, J. Salvas, R. Gosselin, Detecting trace levels of heavy metals in pharmaceutical raw materials with wavelength-dispersive X-ray fluorescence spectroscopy and curve-fitting regression, Spectrochim. Acta - Part B At. Spectrosc. 147 (2018) 59–70. https://doi.org/10.1016/j.sab.2018.05.011.

[69] J. Malherbe, F. Claverie, Toward chromium speciation in solids using wavelength dispersive X-ray fluorescence spectrometry Cr Kβ lines, Anal. Chim. Acta. 773 (2013) 37–44. https://doi.org/10.1016/j.aca.2013.02.035.

[70] V.C. Costa, A.S. Augusto, J.P. Castro, R.C. Machado, D.F. Andrade, D. V. Babos, M.A. Sperança, R.R. Gamela, E.R. Pereira-Filho, Laser Induced-Breakdown Spectroscopy (Libs): Histórico, Fundamentos, Aplicações E Potencialidades, Quim. Nova. 42 (2019) 527–545. http://www.scielo.br/scielo.php?script=sci_arttext&pid=S0100-40422019004500527&lng=en&nrm=iso.

[71] R. Noll, Laser-induced breakdown spectroscopy. Fundamentals and Applications, Springer, 2012.

[72] D. Fernandes Andrade, E.R. Pereira-Filho, D. Amarasiriwardena, Current trends in laser-induced breakdown spectroscopy: a tutorial review, Appl.

Spectrosc. Rev. 0 (2020) 1–17. https://doi.org/10.1080/05704928.2020.1739063.

[73] D. Syvilay, J. Guezenoc, B. Bousquet, Guideline for increasing the analysis quality in laser-induced breakdown spectroscopy, Spectrochim. Acta - Part B At. Spectrosc. 161 (2019) 105696. https://doi.org/10.1016/j.sab.2019.105696.

[74] J. Guezenoc, A. Gallet-Budynek, B. Bousquet, Critical review and advices on spectral-based normalization methods for LIBS quantitative analysis, Spectrochim. Acta - Part B At. Spectrosc. 160 (2019) 105688. https://doi.org/10.1016/j.sab.2019.105688.

[75] J.P. Castro, E.R. Pereira-Filho, Twelve different types of data normalization for the proposition of classification, univariate and multivariate regression models for the direct analyses of alloys by laser-induced breakdown spectroscopy (LIBS), J. Anal. At. Spectrom. 31 (2016) 2005–2014. https://doi.org/10.1039/c6ja00224b.

[76] P.R. Villas-Boas, M.A. Franco, L. Martin-Neto, H.T. Gollany, D.M.B.P. Milori, Applications of laser-induced breakdown spectroscopy for soil characterization, part II: Review of elemental analysis and soil classification, Eur. J. Soil Sci. 71 (2020) 805–818. https://doi.org/10.1111/ejss.12889.

[77] X. Yu, Y. Li, X. Gu, J. Bao, H. Yang, L. Sun, Laser-induced breakdown spectroscopy application in environmental monitoring of water quality: a review, Environ. Monit. Assess. 186 (2014) 8969–8980. https://doi.org/10.1007/s10661-014-4058-1.

[78] R.R. Gamela, E.R. Pereira-Filho, F.M.V. Pereira, Minimal-Invasive Analytical Method and Data Fusion: an Alternative for Determination of Cu, K, Sr, and Zn in Cocoa Beans, Food Anal. Methods. (2020). https://doi.org/10.1007/s12161-020-01904-2.

[79] N. Ahmed, U. Liaqat, M. Rafique, M.A. Baig, W. Tawfik, Detection of toxicity in some oral antidiabetic drugs using LIBS and LA-TOF-MS, Microchem. J. 155 (2020) 104679. https://doi.org/10.1016/j.microc.2020.104679.

[80] M. Martinez, M. Baudelet, Calibration strategies for elemental analysis of biological samples by LA-ICP-MS and LIBS – A review, Anal. Bioanal. Chem. 412 (2020) 27–36. https://doi.org/10.1007/s00216-019-02195-1.

[81] F. Cicconi, V. Lazic, A. Palucci, A.C.A. Assis, F.S. Romolo, Forensic analysis of commercial inks by laser-induced breakdown spectroscopy (LIBS), Sensors (Switzerland). 20 (2020) 1–20. https://doi.org/10.3390/s20133744.

[82] Z.Q. Hao, C.M. Li, M. Shen, X.Y. Yang, K.H. Li, L.B. Guo, X.Y. Li, Y.F. Lu, X.Y. Zeng, Acidity measurement of iron ore powders using laser-induced breakdown spectroscopy with partial least squares regression, Opt. Express. 23 (2015) 7795. https://doi.org/10.1364/oe.23.007795.

[83] J.P. Willis, A.R. Duncan, Understanding XRF Spectrometry. Basic concepts and instrumentation. Volume 1. Printed in the Netherlands (2008).

[84] J. Willis, C. Feather, K. Turner, Guidelines for XRF Analysis Setting up programmes for WD XRF and EDXRF. Published by James Willis Consultants cc, Cape Town, South Africa. First Edition (2014).

[85] G.G. Arantes De Carvalho, M.B. Bueno Guerra, A. Adame, C.S. Nomura, P.V. Oliveira, H.W. Pereira De Carvalho, D. Santos, L.C. Nunes, F.J. Krug, Recent advances in LIBS and XRF for the analysis of plants, J. Anal. At. Spectrom. 33 (2018) 919–944. https://doi.org/10.1039/c7ja00293a.

[86] T. Ohmori, S. Kato, M. Doi, T. Shoji, K. Tsuji, Wavelength dispersive X-ray fluorescence imaging using a high-sensitivity imaging sensor, Spectrochim. Acta - Part B At. Spectrosc. 83–84 (2013) 56–60. https://doi.org/10.1016/j.sab.2013.02.002.

[87] A. Younis, Z. Ahmadi, M.G. Adams, A. Iqbal, A simple method for quantitative analysis of elements by WD-XRF using variable dilution factors in fusion bead technique for geologic specimens, X-Ray Spectrom. 46 (2017) 69–76. https://doi.org/10.1002/xrs.2729.

[88] H.K. Bajwa, O. Santosh, A. Koul, M.S. Bisht, C. Nirmala, Quantitative determination of macroelement and microelement content of fresh and processed bamboo shoots by wavelength dispersive X-ray fluorescence spectrometry, X-Ray Spectrom. 48 (2019) 637–643. https://doi.org/10.1002/xrs.3048.

[89] S. Uhlig, R. Möckel, A. Pleßow, Quantitative analysis of sulphides and sulphates by WD-XRF: Capability and constraints, X-Ray Spectrom. 45 (2016) 133–137. https://doi.org/10.1002/xrs.2679.

[90] M.F. Gazulla, M. Orduña, S. Vicente, M. Rodrigo, Development of a WD-XRF analysis method of minor and trace elements in liquid petroleum products, Fuel. 108 (2013) 247–253. https://doi.org/10.1016/j.fuel.2013.02.049.

[91] R. Bro, PARAFAC. Tutorial & applications., Chemom. Intell. Lab. Syst. 38 (1997) 149–171.

[92] Rasmus Bro, Multi-way Analysis in the Food Industry - Models, Algorithms, and Applications, Thesis Work (1998).

[93] R. Bro, H.A.L. Kiers, A new efficient method for determining the number of components in PARAFAC models, J. Chemom. 17 (2003) 274–286. https://doi.org/10.1002/cem.801.

[94] M.G. Trevisan, R.J. Poppi, Determination of doxorubicin in human plasma by excitation-emission matrix fluorescence and multi-way analysis, Anal. Chim. Acta. 493 (2003) 69–81. https://doi.org/10.1016/S0003-2670(03)00864-X.